

Table of contents

Abstract.....	5
1 Introduction.....	7
2 Background.....	11
2.1 Active tectonics.....	13
2.1.1 Regional tectonics in the Aegean-Anatolian area.....	13
2.1.2 Local tectonics around İzmir.....	20
2.2 The seismicity of İzmir and its surroundings.....	25
2.3 Seismic hazard analysis.....	30
2.3.1 Previous studies in the area around İzmir.....	30
2.3.2 Methods to determine seismic hazard estimations.....	36
3 Methodology.....	41
3.1 Waveform modelling.....	41
3.1.1 Basic model of a seismogram.....	41
3.2 Ground motion simulation.....	49
3.2.1 Low-frequency ground motion.....	49
3.2.2 High-frequency ground motion.....	51
3.2.3 Frequency-dependent radiation pattern.....	54
3.3 Parameters used in ground motion simulations.....	56
4 Input parameters and earthquake scenarios.....	59
4.1 Regional parameters.....	59
4.1.1 Velocity model.....	60
4.1.2 Attenuation relations.....	60
4.2 Fault rupture parameters.....	62
4.2.1 Rupture velocity.....	62
4.2.2 Rise time.....	64
4.2.3 Stress drop.....	65
4.3 Finite fault models.....	68
4.3.1 Fault plane geometry.....	69
4.3.2 Rupture initiation point.....	73
4.3.3 Magnitude.....	74

4.4 Fault rupture scenarios.....	78
4.4.1 İzmir fault.....	79
4.4.2 Gülbahçe fault	83
4.4.3 Tuzla fault	86
4.4.4 Seferihisar fault	88
4.4.5 Manisa fault.....	89
4.5 Databases	94
4.5.1 Fault parameter database.....	94
4.5.2 Point calculations	95
4.5.3 Earthquake catalogs.....	95
5 Ground motion simulation results.....	97
5.1 İzmir Fault	97
5.1.1 1A WIF, Western İzmir Fault segment	98
5.1.2 1B EIF, Eastern İzmir Fault segment.....	100
5.1.3 1C IF, İzmir Fault.....	102
5.2 Gülbahçe Fault	104
5.3 Tuzla Fault.....	106
5.4 Seferihisar Fault	108
5.5.1 5A WMF, Western Manisa Fault segment.....	110
5.5.2 5B IMF, Intermediate Manisa Fault segment.....	112
5.5.3 5C EMF, Eastern Manisa Fault segment.....	114
6 Discussion.....	117
6.1 Discussion of the obtained results.....	117
6.1.1 Comparison of the results.....	117
6.1.2 Attenuation of the seismic waves.....	120
6.1.3 Response spectra	126
6.2 Local site conditions and secondary effects of earthquakes.....	128
6.2.1 Amplification of seismic waves	128
6.2.2 Other secondary effects.....	133
6.3 Weaknesses in the methodology.....	133
6.3.1 Uncertainties in the input	134
6.3.2 Computational deficiencies/limitations of the code	136
7 Conclusion	138
8 Future perspectives	141
8.1 Future work in the area around İzmir.....	141

8.2 Improvement of the methodology	142
9 Acknowledgements	145
10 References	146

Appendixes

A Description of the Enclosed CD	i
B List of Symbols	iii
C Grid Point Calculations	v
D Catalogue of Normal Faulting Earthquakes	xi
E GMS: Program Package	xiii
F GMS: Input Parameters	xxiii
G Attenuation Figures	lxi
H Velocity Response Spectra	lxxi

Abstract

The collision between the Arabian and African plates with Eurasia forces the Anatolian micro-plate to move westward. In the Aegean Sea, the Anatolian micro-plate rotates counter-clockwise and extends due to the subduction along the Hellenic Arc. This deformation results in reactivation of faults on the west coast of Turkey, which results in destructive earthquakes. İzmir, the third largest city in Turkey, has been destroyed by (large) earthquakes several times in recent history, latest in 1778. In this study a deterministic seismic hazard analysis is conducted based on ground motion simulations for nine different earthquake rupture scenarios for recognized faults in the area surrounding İzmir. The method adopted is a hybrid broad-band ground motion simulation technique, which has been previously validated. The earthquake scenarios are based on existing knowledge for source parameters, local as well as regional. Among the various faults surrounding İzmir, the largest peak ground motions are associated with two faults, the İzmir fault which lies underneath the city and the Tuzla fault. The results indicate that a rupture on the 42 kilometer long İzmir fault, can produce ground acceleration as high as 0.3 g on bedrock level in the center of İzmir. Considering the site effect potential in the area, this value needs to be treated as the lower threshold. The simulation results indicate that the historic events that have caused severe destruction in İzmir are most likely to have occurred on either the İzmir or Tuzla faults. Furthermore the attenuation of the simulated ground motions agrees well with empirical relations in the case of peak ground accelerations. The study has also demonstrated several weaknesses in the used methodology, which must be corrected for future studies.

1 Introduction

The Aegean-Anatolian region is one of the most seismically and tectonically active areas within Europe and is characterized by significant seismic hazard. Extensive information exists on active faults based on high-resolution GPS datasets covering the Aegean and Anatolian regions as well as from regional and local geological studies. The GPS data show that the Anatolian micro-plate moves westwards with most deformation occurring along the well known and well studied North Anatolian Fault Zone. Various interpretations of the GPS data exist; dividing the region into a number of micro-plates separated by relatively narrow zones that accommodate most of the tectonic deformation with a well resolved, relatively narrow zone of active deformation in Central Western Anatolia (the Menderes-İzmir region) (Ayhan et al., 2002; Clarke et al., 1998; Cocard et al., 1999; Kotzev et al., 2001; McClusky et al., 2000; Meade et al., 2002). This study contains a short description of the models and no model has been given special prominence.

The active deformation in western Anatolia results in reactivation of various fault systems in the region, as destructive earthquakes have demonstrated in geological and historical times. During recent history there have been three catastrophic earthquakes in İzmir, Turkey. These earthquakes were separated by approximately 50 years; the latest occurring in 1778 (Ambraseys and Finkel, 1995; Papazachos and Papazachou, 1997; Papazachos et al., 1997).

Previously several probabilistic seismic hazard analyses for western Turkey have been conducted (Erdik et al., 2000; Giardini et al., 1999; Giardini et al., 2003). However, the regional scale studies covering the whole Mediterranean area do not provide a detailed picture of the study area around İzmir. The hazard from the single active faults surrounding İzmir is therefore not taken into account. One local probabilistic seismic hazard analysis exists, indicating that there is a 10% probability of exceeding the ground motion level of 0.4 g in İzmir within the next 50 years. However, the results from this analysis do not take the map of active faults in İzmir and its surroundings, which has now become available into account.

The study conducted in this thesis is a hazard analysis for the city of İzmir. The area around İzmir has been populated since 3000 BC, and historic cities in the region (Bergama and Efesus) have been destroyed due to several violent earthquakes. The modern city of İzmir is the third largest city in Turkey - with more than 3 million inhabitants - and is a densely populated area. There are many and large industries in the area and the largest harbor in western Turkey is located in İzmir Bay. The area is an important economic center and a new seismic hazard analysis like the one conducted in this thesis is needed in order to lower the risk in the area.

This important population center is not only located in an area with several active faults and a lot of seismic activity in a large magnitude range, but also located on top of the deltas of several rivers, causing a thick layer of unconsolidated sediments. This will during an earthquake amplify the ground shaking from the seismic waves significantly causing even more damage to the area. However, site effects are not treated explicitly in this study.

Numerical ground motion simulation methods using earthquake scenarios are now currently being applied for estimating the seismic hazard in regions where the hazard is controlled by a nearby large fault (Pulido and Kubo, 2004; Pulido et al., 2004; Sørensen et al., 2007). İzmir is exposed to significant hazard due to its proximity to several active faults. This study aims to quantify the ground motion distributions as a result of earthquake rupture along the well-defined faults near İzmir. In this study seismic hazard in the area is assessed deterministically based on nine different earthquake scenarios on active faults located around the city of İzmir. For each earthquake scenario maps showing ground shaking, in peak ground acceleration and velocity are prepared.

The methodology used in this thesis is based on a hybrid broad-band ground motion simulation technique already applied in Tottori, Japan and Istanbul, Turkey with success (Pulido and Kubo, 2004; Pulido et al., 2004; Sørensen et al., 2007). The source complexity is represented using multi-asperity models with various parameters defining the physical properties of the slip during the scenario earthquake rupture. Input models are based on the characteristics of both the source (fault dimensions, geometry, mechanism, size and location of asperities and their parameters) and the path (seismic velocities and attenuation in the crust). Background knowledge of the fault

characteristics of İzmir is limited, and therefore several earthquake rupture scenarios are investigated. Comparison of the results from the ground motion simulation gives new insights in which fault ruptures that control the hazard in İzmir.

2 Background

İzmir is located in the diffuse transition zone between the Aegean and the Anatolian micro plates, which is an area where several fault systems on various scales interact in a complex tectonic setting. The north-northeast oriented motion of the African plate together with the north-northwest oriented motion of the Arabian plate results in a collision with the Eurasian plate where the main deformation is accommodated along the two major strike-slip faults systems: the North Anatolian (right-lateral) and the East Anatolian (left lateral) faults. As a consequence of this the Anatolian block moves westwards and rotates counter-clockwise. In the south the collision is localized along the Hellenic Arc, where the African plate is subducted underneath the Aegean micro-plate. This results in a north-south oriented extension of the overriding Aegean micro-plate. The north-south oriented extension in the Aegean are results in several large east-west oriented normal fault systems in the eastern Greece and the western Turkey.

Seismic hazard analysis for İzmir and its surroundings is important due to a number of active faults and a high seismic activity. During the last approximately 2500 years there has been a large number of $M > 6$ earthquakes in the area around İzmir, which have resulted in several destructions of the ancient city Smyrne (located where the modern city İzmir is today).

In the following the regional tectonics of the Aegean region as well as the local tectonics around İzmir are described. Seismicity and the previous seismic hazard studies are dealt with in two separate sections. Finally different methods to obtain seismic hazard estimates and ground motion simulations used in previous studies are described in section 2.3.2.

In this chapter references are made to the enclosed CD, which is described in appendix A.

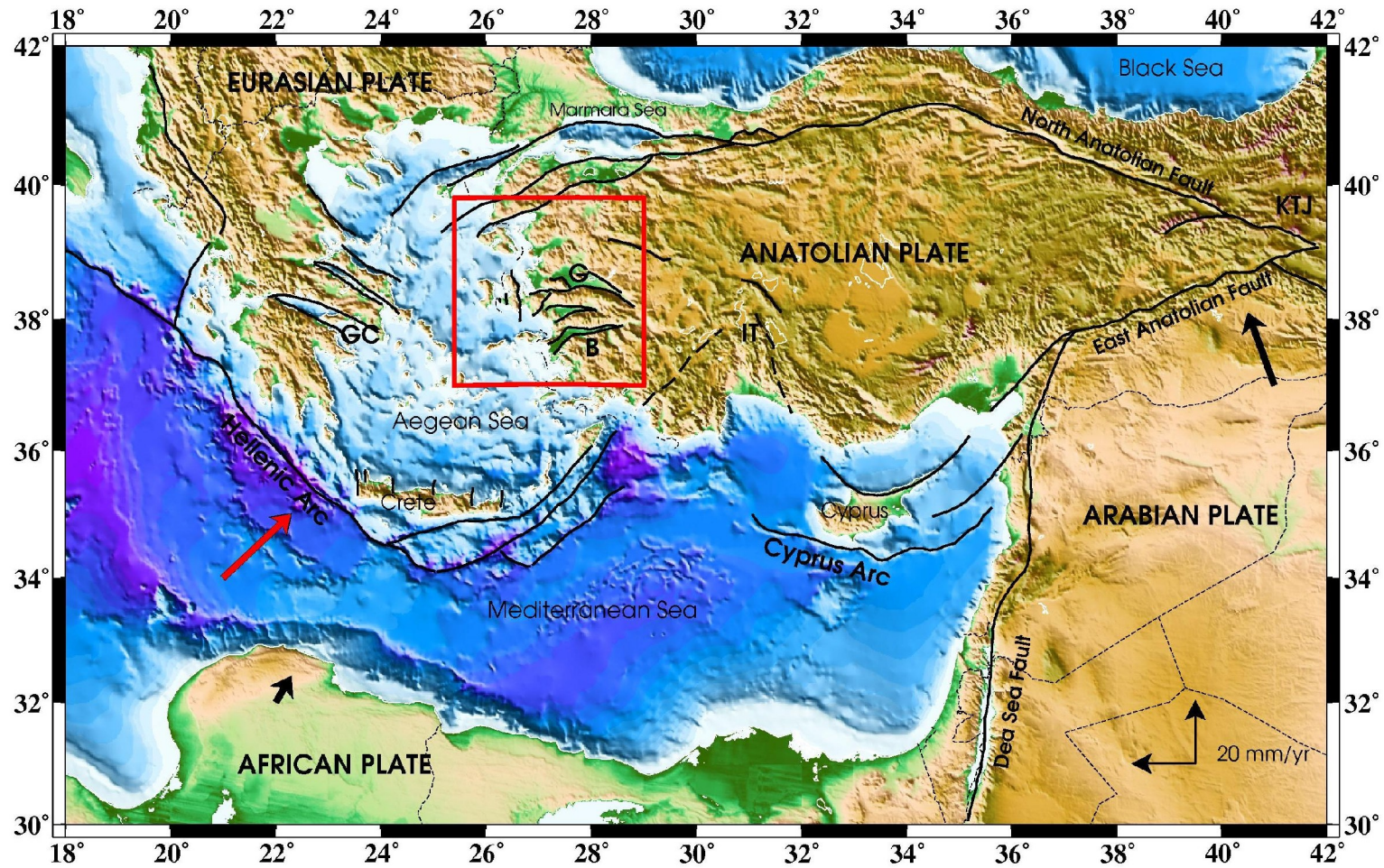


Figure 2.1: Tectonic map of the Aegean-Anatolian region. The solid black lines are plate boundaries, modified from Bird (2003), ten Veen (2004) and McClusky (2000). The heavy black arrows give the plate motions of the African and Arabian plates relative to a stable Eurasia, the red arrow gives the plate motion of the African plate relative to a stable Anatolian plate. All plate motions are taken from the NUVEL 1A model. (The plate motion of the African plate with respect to stable Eurasia is taken in the geographical point 20°E 0°N.) Locations of the main structures are given as follows; GC, Gulf of Corinth; G, Gediz Graben; B, Büyük Menderes Graben; KTJ, Karlova Triple Junction; IT, Isparta Triangle. The study area for the work conducted in this thesis is marked by a red square.

2.1 Active tectonics

The description of the active tectonics influencing the area around İzmir has been divided into two parts: a section concerning the regional tectonics and a section concerning the local tectonics near İzmir. The first is a description of the larger fault systems and trends for crustal deformation across the Aegean Sea. Later, the smaller structures located in the study area are described.

2.1.1 Regional tectonics in the Aegean-Anatolian area

The large-scale deformation of the tectonics in the Aegean-Anatolian region is dominated by the collision of the African and Arabian plates with Eurasia, the continental collision between northwestern Greece and Albania with the Apulia-Adriatic platform and the Hellenic subduction zone in the south (Taymaz et al., 1991). The rates of the collisions between the African and Arabian plates with respect to stable Eurasia are of 10 mm/y towards northeast and 18-25 mm/y towards northwest respectively (McClusky et al., 2000). These collisions result in large zones of deformation from the Zagros Thrust Belt in the east to the Hellenic Subduction Zone in the west (figure 2.1).

The collision of the Arabian plate with the Eurasian plate causes a westward migration of the Anatolian block, defined from the Karliova triple junction in the east to the Aegean Sea in the west. The westward motion of the Anatolian plate is accommodated by the North and East Anatolian Fault zones (NAF and EAF), which are two large right and left lateral strike-slip faults, respectively.

In the west the African plate is subducted underneath the Aegean Sea along the Hellenic Arc. This subduction is found to occur faster than the northward motion of the African plate due to roll-back. This means that the subduction of the African plate proceeds faster due to the weight of the plate itself than due to the under-thrusting by the overriding plate (Taymaz et al., 1991). Roll-back is seen in subduction zones where a very old, and therefore very dense, oceanic plate is subducted. The age of the oceanic part of the African plate is assumed to be somewhere between 80 and 100 My

(Fairhead and Wilson, 2005). In cases where roll-back occur the overriding plate is under extension, this is explained by a migration of the trench: in the case of the Hellenic Arc towards south. The overriding and subducting plates are strongly coupled and the overriding plate will therefore be dragged, as the trench retreats, and thereby stretched perpendicular to the trench.

The two large strike-slip faults NAF and EAF are clearly visible due to their well defined narrow deformation zone. However, this is not the case for the plate boundary south of the Aegean-Anatolian area. The location of the Hellenic Arc southwest of Greece as well as from the Ionian Islands to the south of Crete is clearly exposed in the bathymetry, but in the eastern part of the plate boundary between the African and Anatolian plate the picture becomes more diffuse. From the eastern end of Crete the plate boundary turns towards northeast, which results in strike-slip faults oriented northeast-southwest (Nyst and Thatcher, 2004; Papazachos et al., 1991; Taymaz et al., 1991). How far north these strike-slip faults continue, and at which point the arc bends back into a direction northwest-southeast, is more uncertain. In figure 2.1, the continuation of these strike-slip faults from the Cretan side and the thrust fault from the Cyprian side are shown as dashed lines. These form the Isparta Triangle (IT), with diffuse plate deformation due to the subducting African plate.

The westward migration of the Anatolian block is accommodated mainly along the North Anatolian Fault zone, and this movement is continued into the North Aegean Sea. The North Anatolian fault becomes more complex when entering the Marmara Sea in northwestern Turkey. In the North Aegean Sea the most prominent strike-slip fault system is the North Aegean Trough. In the west this system has a northeast orientation, while the eastern part of the system is oriented more east-northeast (Nyst and Thatcher, 2004; Taymaz et al., 1991).

The focal mechanisms of the earthquakes in the Northern Aegean Sea are mainly strike-slip (green), which is a result of the westward migration of the Anatolian plate. Along the Hellenic Arc and northwards along the continental collision zone between northwestern Greece and Albania with the Apulia-Adriatic platform there are thrust faulting earthquakes (blue). Normal faulting events (red) indicating extension of the

landmasses occur on either side of the Aegean Sea. Active faults and earthquake fault plane solutions for the area around the Aegean Sea are shown in detail in figure 2.2. The extension observed on both sides of the Aegean Sea is due to the subduction of the African plate along the Hellenic Arc and the associated extension of the overriding plate, as previously described. The extension of the Aegean region is accommodated by large (approximately) east-west trending normal fault systems like the Gulf of Corinth in the West Aegean and Gediz Graben and Büyük Menderes Graben in the east. In Greece the opening of these graben structures is towards east, while they are found to be towards west on the west coast of Turkey. Also, the orientation of the faults is more west-northwest in the mainland of Greece and more east-northeast in western Turkey. These observations fit well with the opposite block rotations suggested on each side of the Aegean Sea: counter-clock wise in western Anatolia and clock wise in Greece (Westaway, 1990a, 1990b).

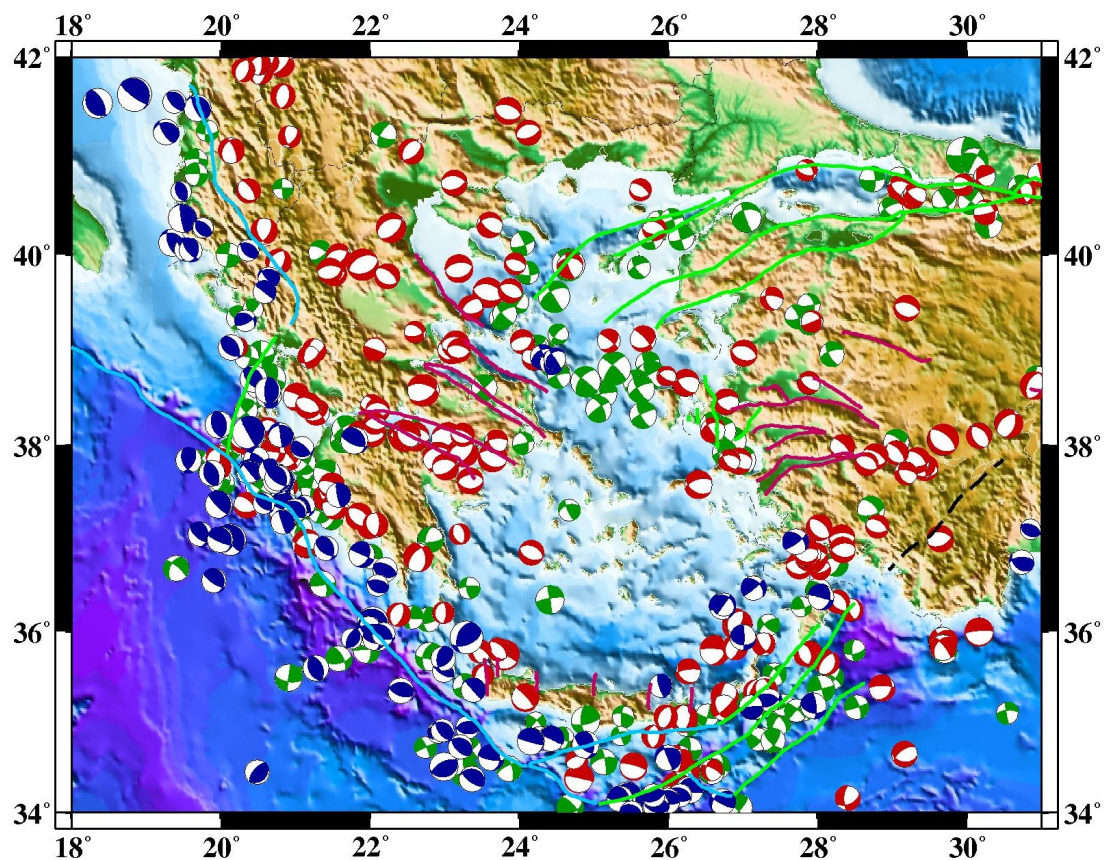


Figure 2.2: Active faults and earthquake focal mechanisms in the Aegean region. Red symbols are used for normal faulting events and faults, green for strike-slip and blue for thrust faulting events and faults. The fault plane solutions are compiled from the INGV, USGS and Harvard moment tensor solution databases. The compiled database is described in chapter 4.5 and appended on the CD with this thesis.

The area surrounding the Aegean Sea is an area of high seismic activity as it is seen in figure 2.2. Several studies on the tectonics of the area have been conducted in various times and with very different datasets. These include historical and instrumental seismic data combined with the focal mechanisms and geology in the area (Jackson et al., 1982; Papazachos et al., 1991; Taymaz et al., 1991). The consensus among these studies is a westward migration of the Anatolian block due to the collision of the African and Arabian plates with the Eurasian plate to the north. It was furthermore suggested that when the central Anatolian block moves westwards it ends in a counter-clockwise rotation at the westernmost part of Turkey and parts of the eastern Aegean area rotates counter-clockwise to have a more southward direction with respect to a fixed Eurasian plate.

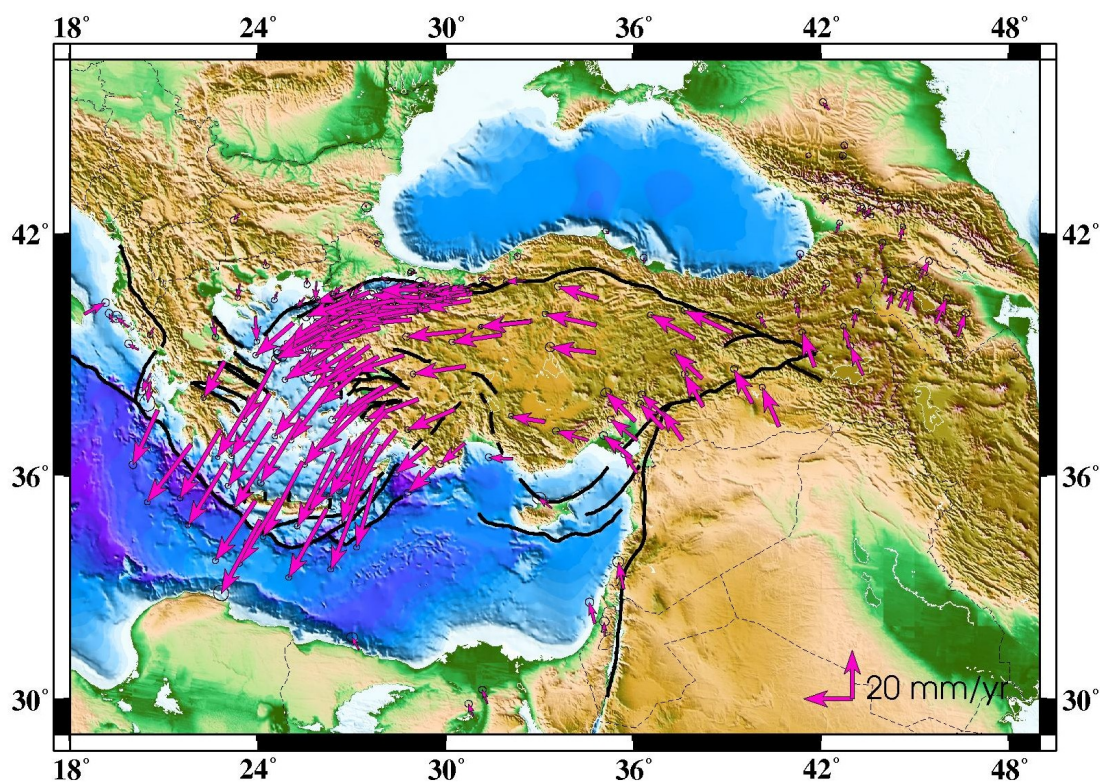


Figure 2.3: GPS horizontal velocities and 95% confidence ellipses in a Eurasia-fixed reference frame from 1988-1997, data plotted is from McClusky et al. (2000). The plate boundaries and faults from figure 2.1 are also shown.

Later studies of the tectonics of the Aegean-Anatolian region have been conducted with data from GPS (Ayhan et al., 2002; Clarke et al., 1998; Cocard et al., 1999; Kotzev et al., 2001; McClusky et al., 2000; Meade et al., 2002). These studies confirmed the earlier models of the area with an Anatolian block escaping towards west and a change in the velocity field in western Turkey and the Aegean Sea. The

interpretation of the data has however resulted in several models for the tectonics of the Aegean-Anatolian area, as will later be discussed.

From the GPS study by McClusky et al. (2000), covering the whole Anatolian block, it is evident that the plate motions are increasing from the eastern to the western Anatolian and Aegean region, see figure 2.3.

The GPS velocity vectors have stable westerly orientation in the eastern and central Turkey, whereas a counter-clockwise rotation of west Anatolia is observed in the Aegean area. This velocity change is also found from various other GPS studies in the region, (Ayhan et al., 2002; Clarke et al., 1998; Cocard et al., 1999; Kotzev et al., 2001; McClusky et al., 2000; Meade et al., 2002).

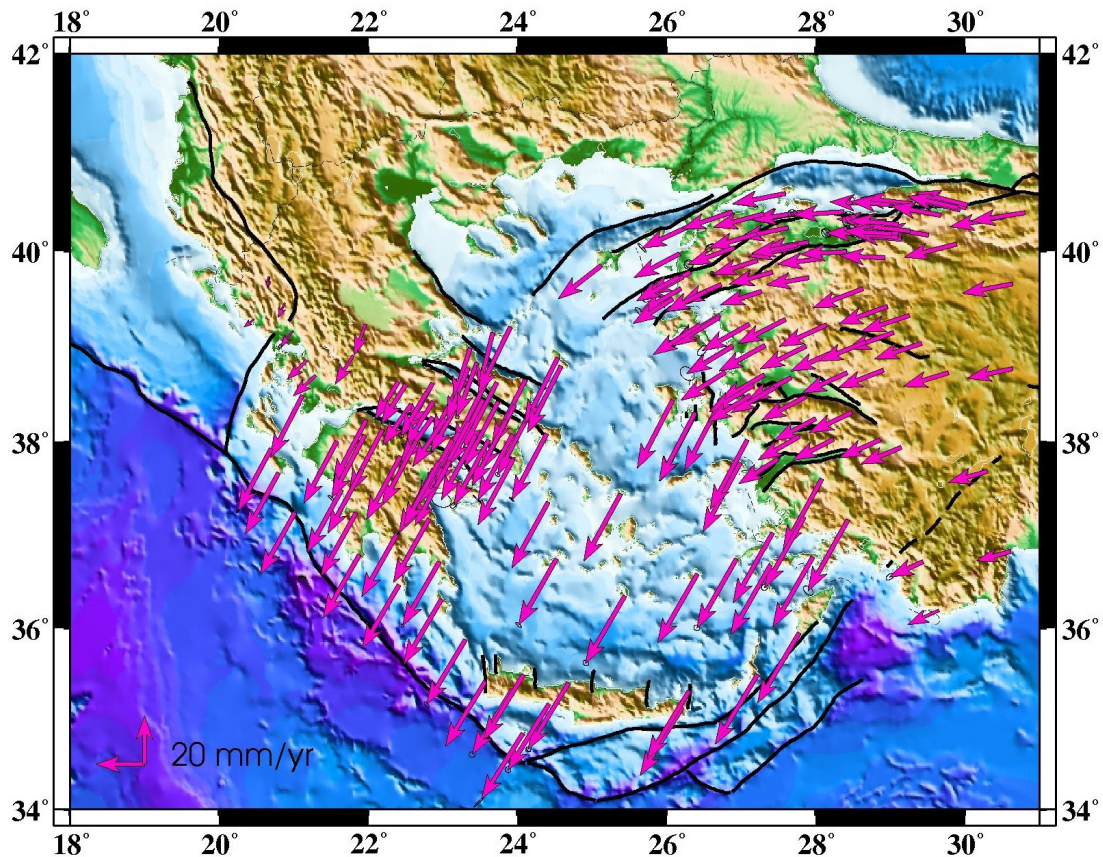


Figure 2.4: Observed GPS velocity field in relation to stable Eurasia (north of map area). The GPS velocity field is gathered from previous studies conducted in the area (Ayhan et al., 2002; Clarke et al., 1998; Cocard et al., 1999; Kotzev et al., 2001; McClusky et al., 2000; Meade et al., 2002), and compiled by Nyst and Thatcher (2004). The plate boundaries and faults from figure 2.1 are also shown.

In order to obtain a more detailed picture of the GPS velocity field in the Aegean Sea and its surroundings, Nyst and Thatcher (2004) compiled several previous GPS

surveys in order to assess the velocity field in the Aegean region. The measured velocity field is given in figure 2.4.

From both figure 2.3 and 2.4 it is evident that the western part of the Anatolian block is moving towards west, and that the western Turkey is experiencing a counter-clockwise block rotation. These rotation directions are also confirmed by other studies not related to GPS measurements (Westaway, 1990a, 1990b). A comparison between the plate velocity vector for the African Plate with respect to a stable Anatolian block, shown as a red arrow in figure 2.1, with the velocity field obtained by both McClusky et al. (2000) and the combined velocity field gathered by Nyst and Thatcher (2004) shows a good agreement in the orientation and the magnitude of the plate velocities.

The different studies of the Aegean-Anatolian area have suggested several kinematic models of the Aegean tectonics (Armijo et al., 1996; Goldsworhty et al., 2002; Le Pichon et al., 1995; McClusky et al., 2000; McKenzie, 1972; McKenzie, 1978; McKenzie and Jackson, 1983; Nyst and Thatcher, 2004; Taymaz et al., 1991). The various models are summarized in figure 2.5 in order to show the complexity of the tectonics of the area.

Among these different studies there is a general agreement on a clockwise and counter-clockwise rotation of Greece and western Anatolia respectively. The interpretation that the westward migration of the Anatolian block continues along strike-slip faults in the North Aegean Sea is also found to be generally agreed, just like the extension in the north-south direction in the central Aegean Sea and in western Anatolia.

However, there are different interpretations of the deformation in the Aegean Sea. Two opposing theories exist; one with a simple common micro-plate for the western Anatolia and the Aegean Sea (Armijo et al., 1996; Goldsworhty et al., 2002; Le Pichon et al., 1995; McKenzie and Jackson, 1983) and another with two different micro-plates (McClusky et al., 2000; McKenzie, 1972; McKenzie, 1978; Nyst and Thatcher, 2004; Taymaz et al., 1991). In the latter case the boundary between the Anatolian and the Aegean micro-plate is located across the study area of this thesis.

The basis for this location is due to a change of direction in the velocity field in the westernmost part of Turkey (figure 2.4).

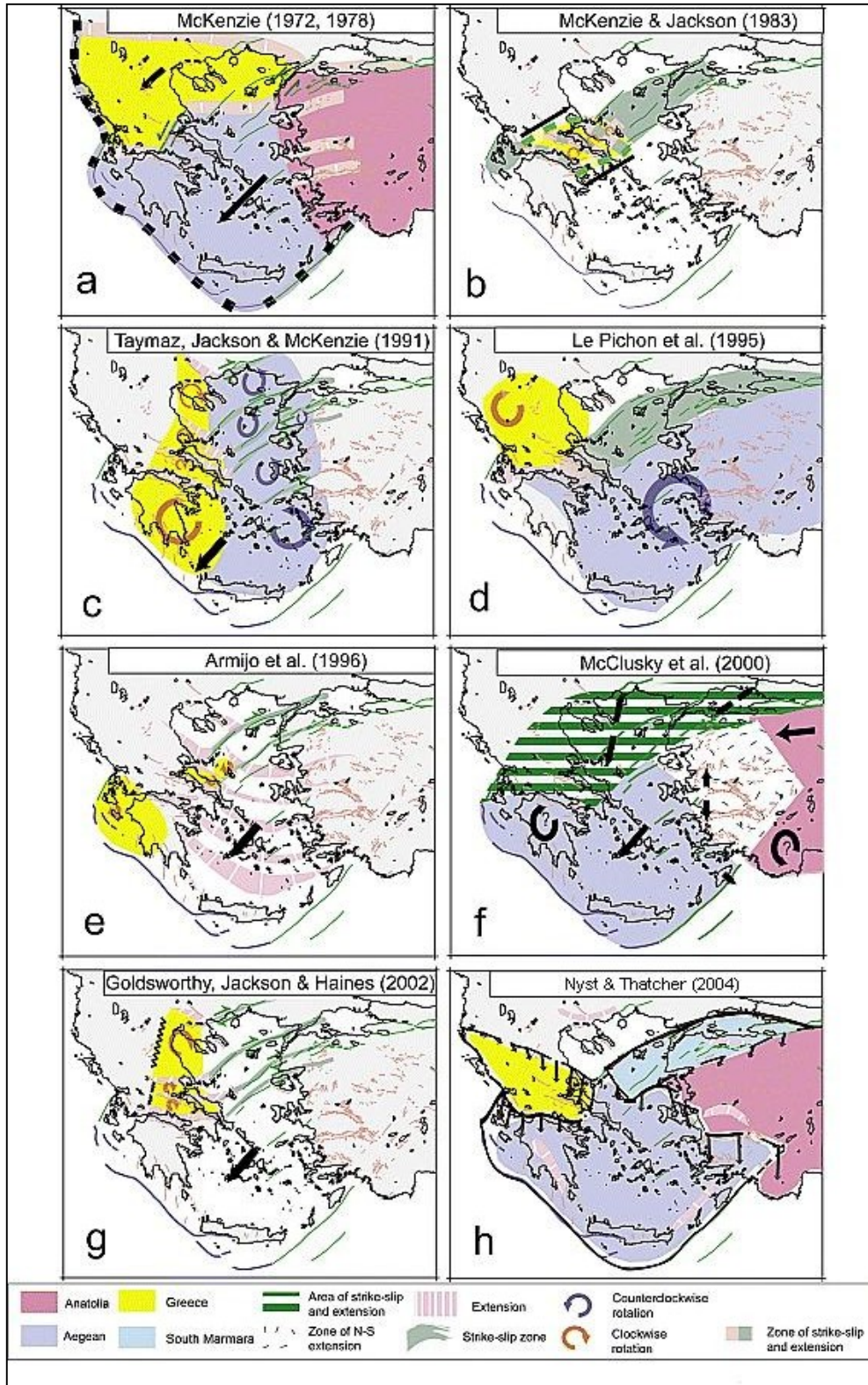


Figure 2.5: Kinematic models of Aegean tectonics (Nyst and Thatcher, 2004).

Generally there seems to be good agreement with the sense of motion of the known structures and the earthquake focal mechanisms (Nyst and Thatcher, 2004). Several studies have been conducted to map the stress axis in the region (e.g. Nyst and Thatcher (2004) and Papazachos et al (1991)). The stress axis in the İzmir area is described in the following section.

2.1.2 Local tectonics around İzmir

Due to the counter-clockwise rotation of western Anatolia discussed in the previous section faults with various orientation become reactivated in the area around the city of İzmir, which is the focus in this study. The Mineral Research and Exploration Institute, Ankara, Turkey (MTA) has located more than 40 active faults in the vicinity of the city, shown in figure 2.6 (Emre et al., 2005b).



Figure 2.6: Map of the study area around İzmir, showing active faults that are recognized by Emre et al. (2005). Locations mentioned in the text are also indicated on the map.

As earlier discussed the change of the GPS vectors in this area is evident (see figure 2.4). As it was also seen in figure 2.5 some authors (e.g. Nyst and Thatcher (2004), McClusky et al. (2000) and Taymaz et al. (1991)) have interpreted this change in the

direction of the vectors of the GPS velocity field as a more or less diffuse plate boundary, which in this case crosses the study area of this thesis.

Aktuğ and Kılıçoğlu (2006) have investigated the velocity field around İzmir more closely by a GPS survey based on previous data (from 1992 and newer) and a new denser network (2001-2004). The geographical coverage of this network had special emphasis on three large faults in the area: the İzmir fault, the Gülbahçe fault and the Tuzla fault (see figure 4.3). These three faults are among those for which ground motion simulations are conducted in this study, and they are referred to as scenario 1(A-C) IF, 2 GF and 3 TF, respectively. For details of each fault see section 4.4.1-3.

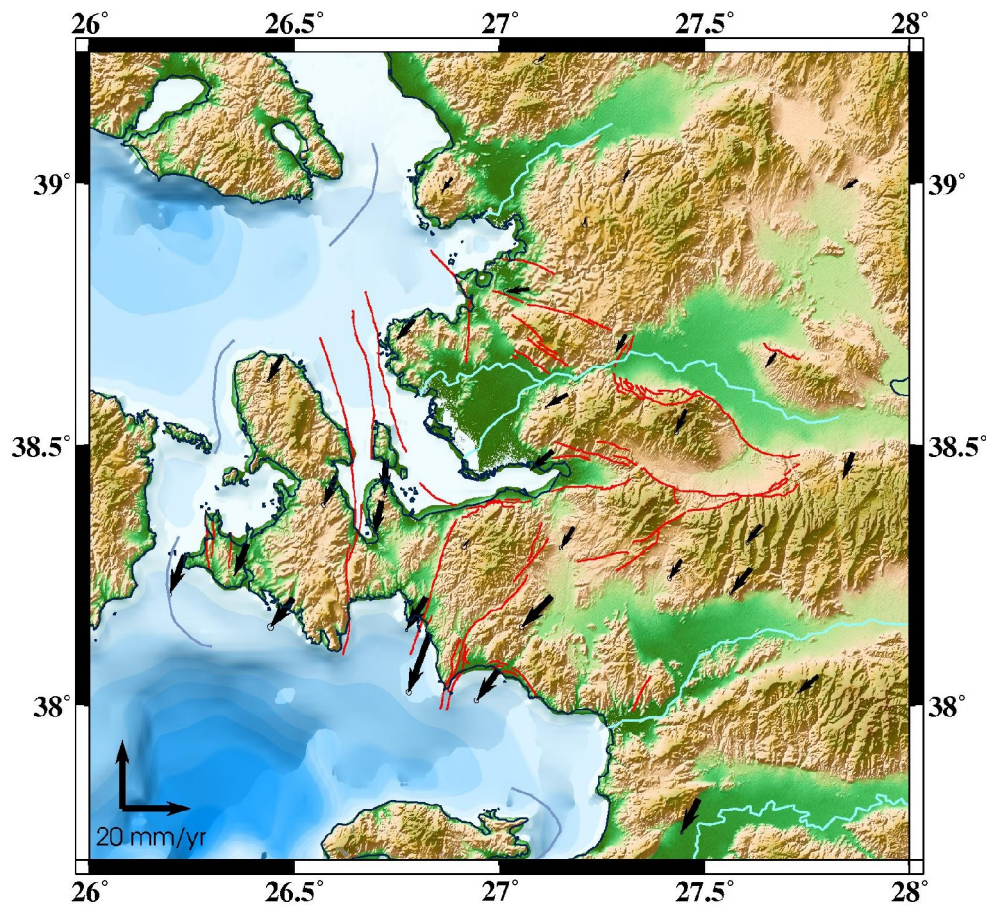


Figure 2.7: The GPS field in the vicinity of İzmir with a stable Anatolian block as a reference frame. Based on the recent study by Aktuğ and Kılıçoğlu (2006). Note the significant variation in the magnitude and orientation of the GPS-velocity vectors.

The detailed geographical coverage of the GPS network in the study by Aktuğ and Kılıçoğlu (2006) has the advantage of being able to map small-scale block rotations instead of looking at the entire western Anatolia as one single rigid block. Also the

network was set up in order to map the rate of opening and extension across the İzmir bay (Aktug and Kilicoglu, 2006).

The velocity field as found by Aktuğ and Kılıçoğlu (2006) is given in figure 2.7 with respect to the Anatolian fixed reference frame. From the figure it is evident that block rotations exist in the area around İzmir; especially the relative velocities on each side of the Seferihisar and Tuzla faults (scenario 3 TF and 4 SF described in section 4.4.3-4) are significant. The increase in velocities from the east to west, and north to the south is also evident, like the change in the velocity field across the İzmir bay, which confirms the opening of the bay.

The earlier deformation in the area is investigated in a few paleomagnetic studies of the area around İzmir (Isseven, 2001; Kissel, 1986; Kissel et al., 1987; Orbay et al., 2000; Tapirdamaz, 2005). However, there are significant uncertainties concerning the location of the samples gathered in the database by Tapirdamaz (2005) (shown as lines in figure 2.8), which contains the results from previous paleomagnetic studies in the study area.

As it is seen in figure 2.8 there are several points reported at sample sites located in the ocean, which is probably due to location errors. In figure 2.8 five circles are shown dividing the results into different studies. The red circles are from a study conducted by Kissel (1986), the blue is from Isseven (2001) and the green study, conducted at the Karaburun Peninsula, is from a study of Orbay (2000). The 95% confidence intervals for the average values found for each study are shown as small circles. The statistics on these data have been conducted by Harald Walderhaug (personal communication).

From figure 2.8 it is evident that different rotations occur in the blocks around İzmir, and especially the difference in strikes found in the study on the Karaburun Peninsula, which according to the paleomagnetic data is subject to a clockwise rotation, and in the İzmir-Bergama area, where a counter-clockwise rotation is observed, is of interest for the block rotations around İzmir. However, since several active faults are located between the areas of these two studies this does not give an indication of the possible

block rotations due to the deformation along the Gülbahçe, Seferihisar, İzmir and Tuzla faults from these studies, which is of main interest in this thesis.

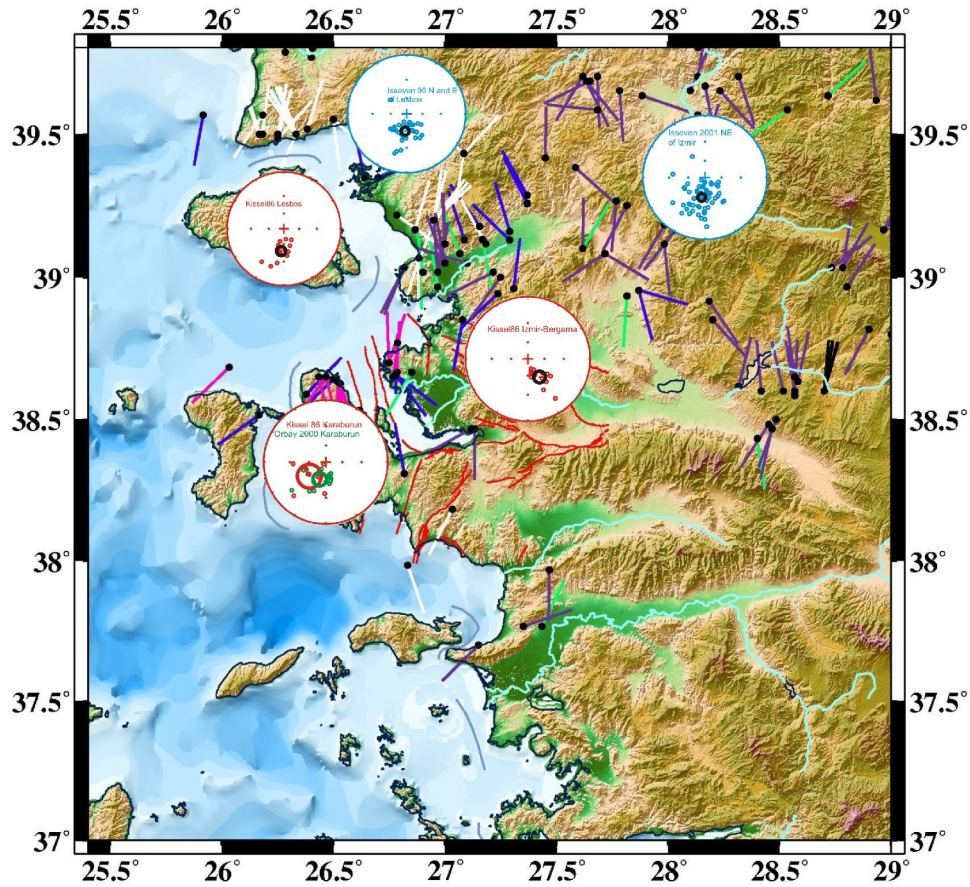


Figure 2.8: Paleomagnetic data from various studies in the vicinity of İzmir, (Isseven, 2001; Kissel, 1986; Kissel et al., 1987; Orbay et al., 2000; Tapirdamaz, 2005).

Different stress axes for the area based on previous studies are given in figure 2.9 (Kiratzi and Louvari, 2003; Nyst and Thatcher, 2004; Papazachos et al., 1991; Zhu et al., 2006). The general trend of the stress axes in the area is northeast-southwest with an azimuth of 14° to 27° N. In the study conducted by Papazachos et al. (1991), the red arrow, the stress axis was deduced by seismicity in the period from 1961 to 1986 where the maximum horizontal extension axis is determined based on the lower hemisphere projections of the T axes in the whole Aegean. In the study conducted by Kiratzi and Louvari (2003) the stress pattern of the Aegean area is found by analyzing T axes from an earthquake catalog covering the time period 1953 to 1999 (yellow arrow). The blue arrow in figure 2.9 is from the study conducted by Nyst and Thatcher (2004). The arrow shows the direction of the principal axis of extension in western Anatolia, which is in the order of 47 ± 8 nanostrain/year. The deformation rate and the direction of the stress axis were also determined previously from the GPS

survey of the Aegean area (also mentioned in chapter 2.1.1). The black arrow in figure 2.9 is from the study by Zhu et al. (2006), and the extensional direction of western Turkey is found by averaging all the fault plane solutions of 364 earthquakes in the area of İzmir in the period 2002 and 2003.

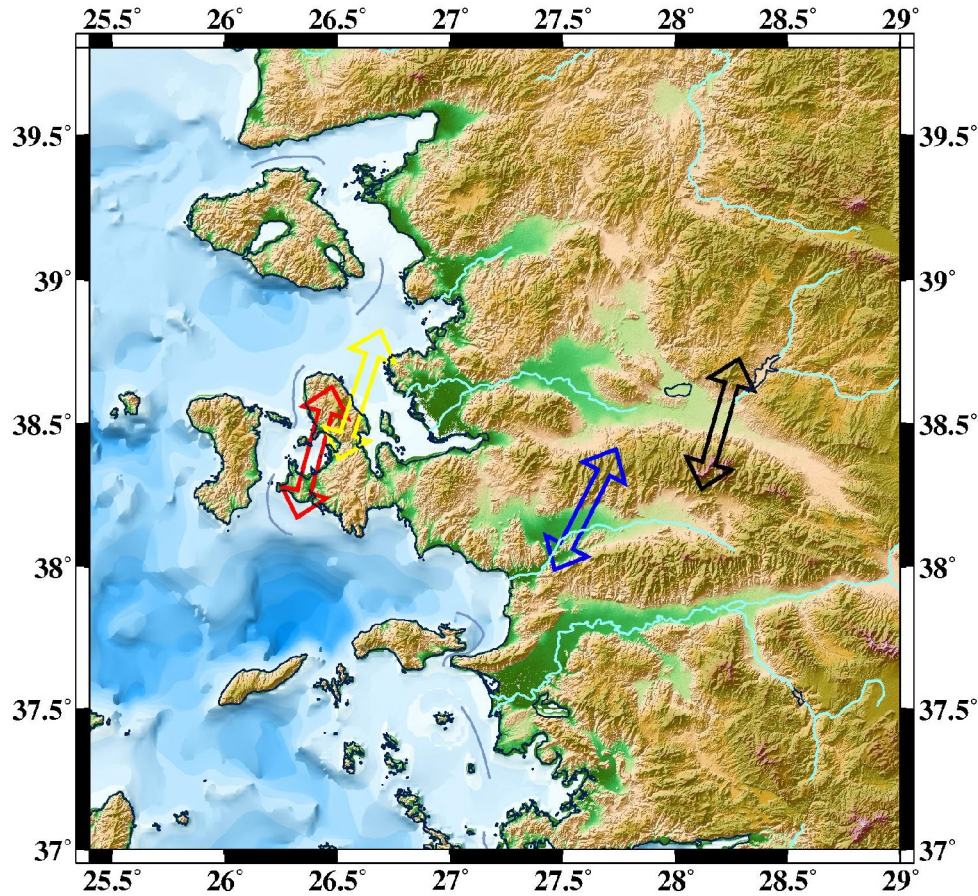


Figure 2.9: Stress axis for the İzmir area as found by different studies; the red arrow is from Papazachos et al. (1991), the yellow arrow is from Kiratzi and Louvari (2003), the blue arrow is from Nyst and Thatcher (2004) and the black arrow is from Zhu et al. (2006). The arrows are of equal size, and do not tell anything about the strain rate in the area.

The four extensional axes for western Turkey given in figure 2.9 have approximately the same direction, and the orientation of these axes are near perpendicular to the large east-west trending fault systems of the area (i.e. Gediz Graben, Büyük and Küçük Mendere Massif Grabens), which is in agreement with east-west oriented normal faults. Similarly the local GPS study conducted by Aktuğ and Kılıçoğlu (2006) confirms the strike-slip motion along the north-south trending strike-slip faults in the area around İzmir.

2.2 The seismicity of İzmir and its surroundings

Tectonic deformation in western Anatolia produces a high rate of seismic activity on both a regional scale (see figure 2.2) and on a local scale (see figure 2.12). During historical times İzmir (the ancient city of Smyrne) and its surroundings is known to have experienced several very destructive earthquakes.

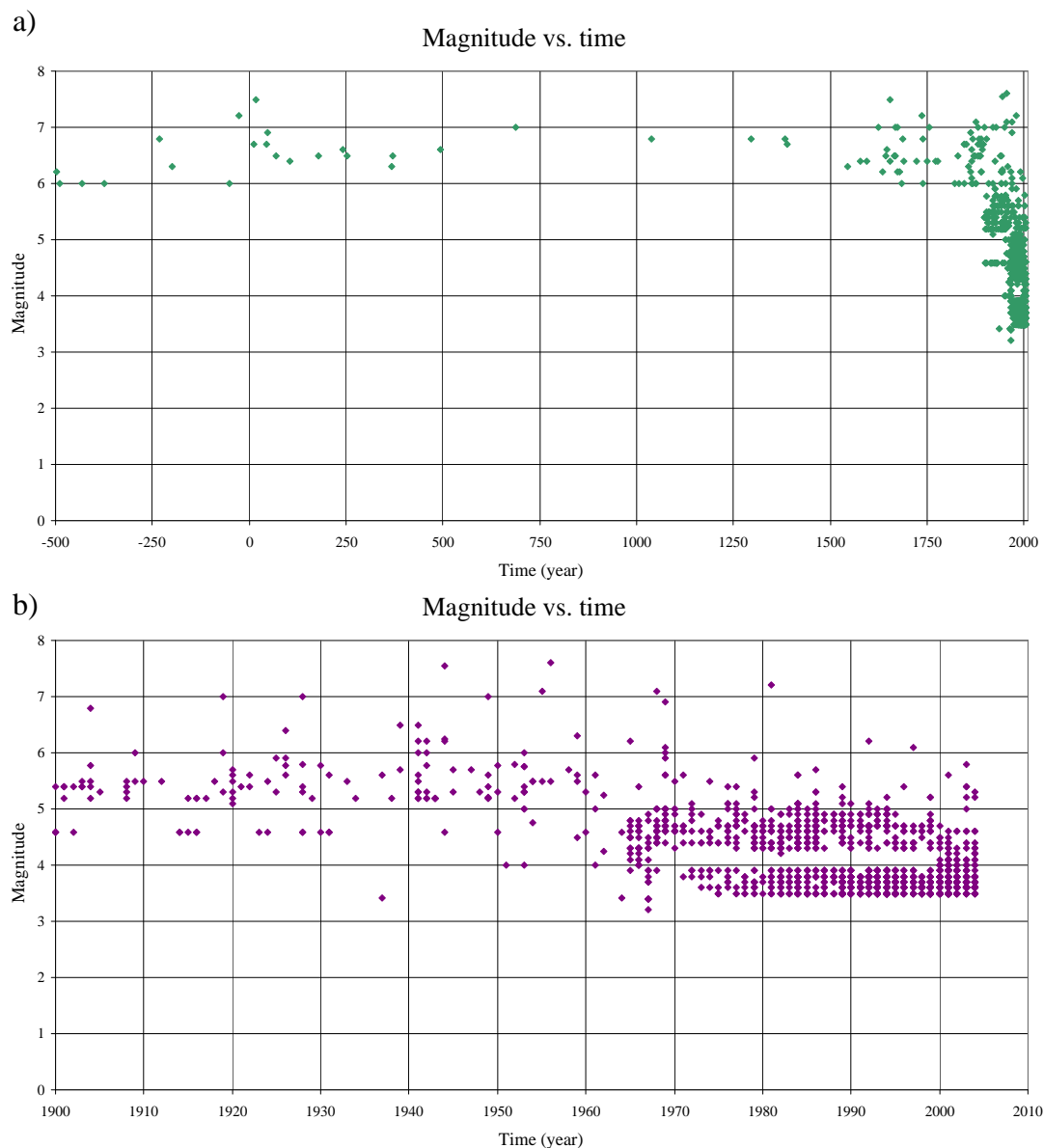


Figure 2.10: Catalog completeness, showing reported magnitudes of earthquakes with time; **a)** The entire time span of the catalog from 496 BC to 2004, **b)** the instrumental period from 1900 to 2004.

Within the framework of this thesis an earthquake catalog was compiled for the period 496 BC to 2004. The catalog is complete for moment magnitudes of more than 6 for the whole time span. Magnitude completeness goes down to 3.0 for the recent past of

the catalog (last 40 years). The earthquake catalog compilation is described in chapter 4.5.3 and the catalog is available on appended CD attached to this thesis, for which there is given an explanation to in appendix A.

In order to check the completeness of the compiled seismic catalog a plot showing the reported seismicity during time versus moment magnitude is given in figure 2.10. It is seen that for the whole time period from 496 to 2004 the catalog is complete for a moment magnitude larger than 6, while it is complete for moment magnitudes of 4.5 since 1900 and even down to 3.5 from 1960 as a consequence of the implementation of the WorldWide Standard Seismograph Network (WWSSN) and the comprehensive earthquake reports from the International Seismological Center (ISC). In figure 2.10a there seems to be a gap in seismicity from approximately year 500 to 1250. The reason for this is unknown.

From the macroseismic records compiled by Papazachos et al. (1997), Papazachos and Papazachou (1997) and Ambraseys and Finkel (1995) it is evident that the area surrounding İzmir has been subject to severe ground shaking and that the city has been destroyed several times. The most significant events in the historical catalog are shown in table 2.1 (see also the appended CD) and shown in figure 2.11. The seismic gap from 500 to 1250 mentioned in the above paragraph is also visible in the part of the historic catalog shown in table 2.1, where only one event is observed between the earthquake of 178 and the event in 1625 – a time period of approximately 1450 years. This is a very long period of seismic quiescence in the area when compared to the rest of the catalog. It might indicate lack of historical sources from this period of time.

Table 2.1: Part of the historical catalog, compiled from Papazachos et al. (1997), Papazachos and Papazachou (1997) and Ambraseys and Finkel (1995), covering the events occurred in Smyrne, and the events of which there are reports of severe ground shaking in the city of Smyrne. Earthquakes with epicenter reported in Smyrne have been written with bold.

Year	Latitude	Longitude	Mw	Intensity	Location name
47	37.84	27.16	6.9	VIII	Samos ¹
178	38.30	27.10	6.5	VIII	Smyrne
1039	38.40	27.30	6.8	VIII	Smyrne
1625	39.20	27.80	7.0	VII	Manisa
1654	38.50	27.10	6.4	VIII	Smyrne
1674	38.40	26.30	6.2	VII	Chios ¹
1680	38.40	27.20	6.2	VII	Smyrne
1688	38.38	27.17	6.8	X	Smyrne ²
1690	38.60	27.40	6.4	VII	Smyrne

1702	37.70	29.10	7.0	X	Denizli ¹
1723	38.40	27.00	6.4	VII	Smyrne
1739	38.40	26.90	6.8	IX	Foca
1772	38.80	26.70	6.4	VIII	Foca
1778	38.40	26.80	6.4	IX	Smyrne³
1845	38.60	27.50	6.7	IX	Manisa ¹
1845	39.10	26.30	6.7	X	Lesbos ¹
1865	39.40	26.20	6.2	IX	Lesbos ¹
1865	37.70	27.00	6.0	VII	Samos ¹
1867	39.25	26.21	6.8	X	Lesbos ¹
1868	37.60	26.90	6.0	VII	Samos ¹
1869	36.98	28.32	6.8	IX	SW. Turkey ¹
1873	37.80	27.10	6.5	VII	Samos ¹
1880	38.50	27.20	6.7	IX	W. Turkey ¹
1883	38.30	26.60	6.8	IX	Cesme ¹
1889	39.20	25.90	6.8	IX	Lesbos ¹
1904	37.66	26.93	6.8	VIII	Samos ¹
1919	39.20	27.40	7.0	IX	W. Turkey ¹
1928	38.20	27.50	6.5	IX	W. Turkey ¹
1942	39.40	28.10	6.2	VIII	W. Turkey ¹
1949	38.58	26.23	6.7	IX	Chios ¹
1992	38.19	27.05	6.2	VII	Doganbey ¹

¹ The earthquake was felt in Smyrne

² The city of Smyrne was lowered 60 cm during the rupture

³ Following there were observed several aftershocks and ground cracks were found in Urla.

The historic events from table 2.1 draw up a clear sign of activity on both the İzmir and the Tuzla faults as seen in figure 2.11. This indicates that these two faults are the most active ones in the area, and also the ones producing the largest intensities in İzmir.

The latest large earthquake with hypocenter near İzmir occurred in 1788 with a moment magnitude of 6.4 following two earlier events occurring with 35 and 65 years time difference respectively (1688 and 1723). This rather dense distribution of large earthquakes near the city can possibly be explained by coupling between the faults in the area and that the stress release in one fault results in stress transfers provoking the next rupture. However, during the last 220 years no large earthquake has taken place in the city, which indicates that there is built up a significant amount of stress in the faults surrounding the city. From the earthquake in 1688 (Mw=6.8) it was noted that the city center of Smyrne, located on the hanging wall block of the İzmir fault, was lowered by 60 cm.

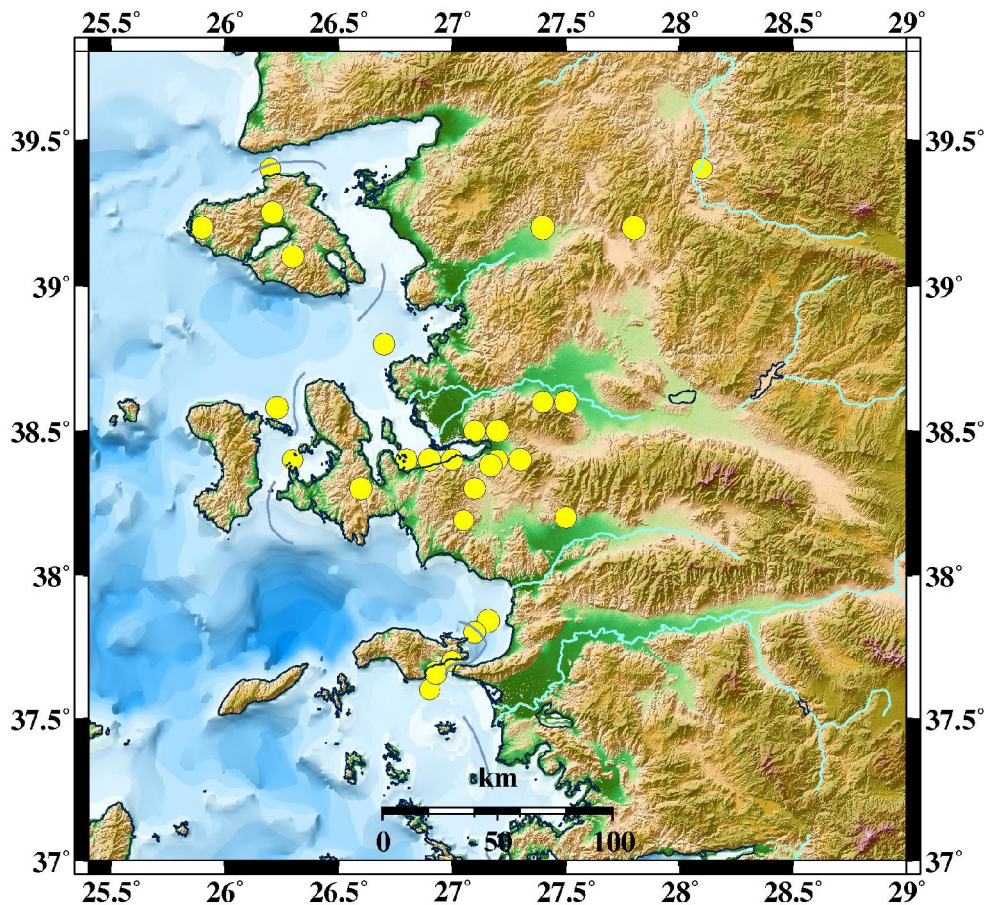


Figure 2.11: The earthquakes that have caused significant ground shaking in İzmir (Smyrne) during the period 47-1992. Events are extracted from the compiled historical catalog and are given in table 2.1.

The seismicity in the study area is shown in figure 2.12 (a-d) for events larger than $M_w = 3$, $M_w = 4$, $M_w = 5$ and $M_w = 6$, respectively. As it is seen in figure 2.12 (a-b) the seismicity of the area is widespread, however the large events ($M_w > 6$) shown in figure 2.12 (d) correlate well with the larger structures identified in the area.

From figure 2.12 (a and b) it is seen that micro-seismicity ($M_w < 4$) is lacking along the large structures of the study area as the Büyük, the Küçük and the Gediz Grabens. The micro seismicity is located in clusters northeast and northwest of İzmir as well as south of the city. This is probably associated with the regional deformation caused by the observed westward migration of Anatolia as described previously. In figure 2.12 (b), the structures that are modeled for ground motion simulations in this study are clearly visible by the earthquake activity, especially the İzmir, Tuzla and Gülbahçe faults. These are even more pronounced in the map showing seismicity for moment magnitudes larger than 5 (figure 2.12 (c)).

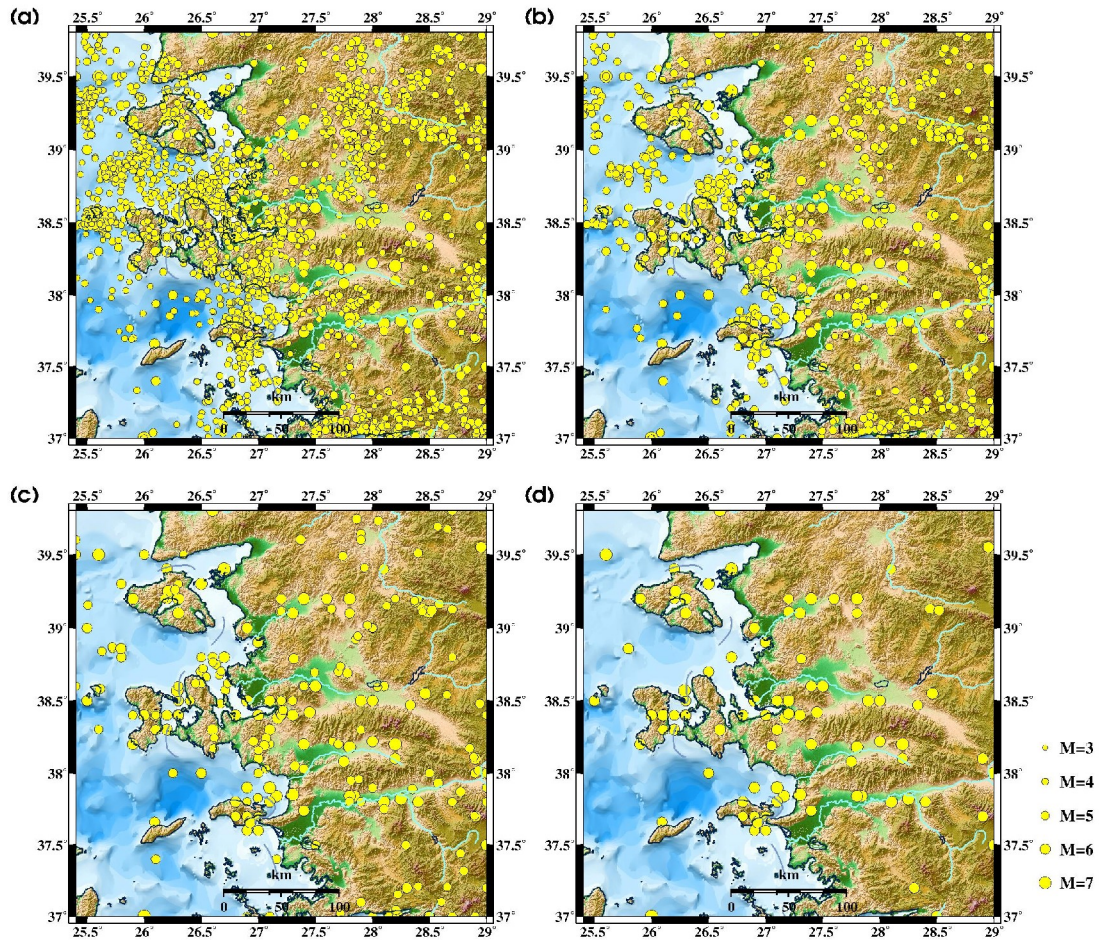


Figure 2.12: Seismicity in the study area around Izmir from 496 BC until 2004. (a) All events in the compiled catalog, $M > 3$. (b) $M > 4$. (c) $M > 5$. (d) $M > 6$, regarding this magnitude range the seismic catalog is complete for the whole time span, and it is noted that the larger events occur along the faults shown in figure 2.2 and 2.6. All magnitudes are in moment magnitude.

A specific earthquake sequence between Chios and the Karaburun Peninsula is observed in figure 2.12 (c and d). Since there is no known structures striking east-west at this location this seems rather unusual and might be a result of historical events that are located in grid points. However, only one of these events is shown on figure 2.11, which shows the historical events in the area. It ought to be mentioned that the catalog compiled to show the historical events (figure 2.9) originates from the studies made by Papazachos et al. (1997), Papazachos and Papazachou (1997) and Ambraseys and Finkel (1995) and based on observed intensities, while the catalog used in figure 2.12 contains much more data and therefore is assumed to be more complete. Consequently it is not clear whether these events are historical or of more recent time.

Recently, in autumn 2005 a high seismic activity was observed in the Gulf of Sığacık with approximately 50 events ($M_w > 3.2$) from the 17th to the 31st of October, and three

earthquakes of moment magnitude larger than 5.4 took place within three days (October 17th to 20th) (Benetatos et al., 2006). The focal mechanisms of the large events indicate a strike-slip motion on faults striking northeast southwest in the Gulf of Sığacık, however such structures have not yet been recognized by e.g. seismic reflection surveys.

2.3 Seismic hazard analysis

In this thesis a seismic hazard analysis is conducted by ground motion simulations based on different earthquake scenarios on the faults in the vicinity of İzmir. Due to the preceding high rate of seismicity in western Turkey various seismic hazard analyses have been conducted for the area. Especially three studies need to be mentioned; one by the Kandili observatory in Istanbul (KOERI) conducted as a part of the GSHAP project (Giardini et al., 1999), followed by a regional study for the Mediterranean area from the SESAME project (Giardini et al., 2003; Jimenez et al., 2003) and a study conducted by the Istanbul Technical University and Boğaziçi University for İzmir focusing on the area close to the city (Erdik et al., 2000). The main results of these studies are described in section 2.3.1.

The methodology adopted in this study differs significantly from the previous studies concerning this region, and follows an already accepted method developed by Pulido and Kubo (2004), which is described in chapter 3. A discussion on various methods used in conducting seismic hazard analysis is included (see section 2.3.2).

2.3.1 Previous studies in the area around İzmir

Several probabilistic seismic hazard studies were performed covering the area of İzmir in the past. In this section the results of three former studies of the area are given.

Global Seismic Hazard Assessment Program (GSHAP) 1992-1999

The GSHAP project (Giardini et al., 1999) was conducted aiming to produce a global probabilistic seismic hazard analysis. Within this project a number of regions were

identified. One of these was covering Turkey and the neighboring regions. The work was done by use of the most recent attenuation relations at the time for the region, a large compiled seismicity database and after studying the tectonics of the area in detail (Erdik et al., 1999). The result of this study is shown in figure 2.13, where the study area of this thesis is approximately marked by a red square.

Figure 2.13 shows the seismic hazard map for Turkey and its surroundings obtained during the GSHAP project. The return period used in the map is of 475 years, which equals a 10% probability of exceedance in ground motion within 50 years. In the area around İzmir expected peak ground acceleration values reach 0.3-0.5 g (Erdik et al., 1999). However, since the calculated ground motions are for the bedrock the ground motion is therefore expected to be different during an earthquake due to sediment layers.

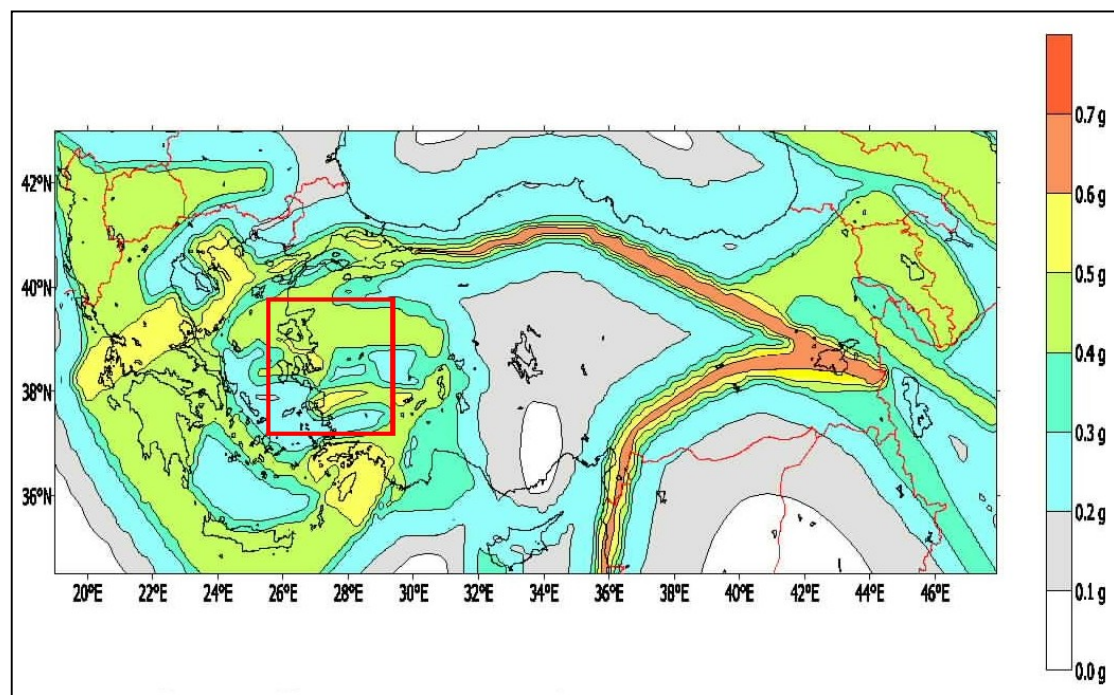


Figure 2.13: Probabilistic seismic hazard map from the GSHAP project (Giardini et al., 1999) for a return period of 475 years (10% exceedance within 50 years). The values for ground motions are given in g. From Erdik et al. (1999). The study area of this thesis is approximately marked by a red square, placed by the author.

The predicted estimates for ground shaking inside the study area are very coarse. Two main areas where the peak ground acceleration is expected to exceed 0.5 g with a 10% probability of exceedance within the next 50 years are observed. These areas coincide with the Büyük Menderes Graben south of İzmir and the area northwest of İzmir towards Foça (see figure 2.6 for location names). In the north of the study area a large

area (green) is observed, where the peak ground acceleration is predicted to be of 0.4 g. This area coincides with the area of micro-seismic activity showed in figure 2.12a. The results from the GSHAP project are of a regional scale, and therefore no details can be obtained that can be related to specific faults in the study area. Large structures like the North and East Anatolian faults, the Hellenic Arc and the Menderes Graben are clearly visible; however; the details on single faults identified by Emre et al. (2005) in the area surrounding İzmir are lost in the regional content.

SEismotectonic and Seismic hazard Assessment of the MEditerranean (SESAME) 2003

Following the GSHAP project, the SESAME project was launched, focusing only on the European-Mediterranean region. This project is also based on a probabilistic seismic hazard analysis and was initiated to take the weaknesses in the Mediterranean region in the GSHAP project (e.g. large number of independent areas) into account. In the SESAME project a more detailed and complete, integrated seismic source model is developed, which results in a more homogeneous hazard map for the region (Jimenez et al., 2003).

Figure 2.14 shows the probabilistic seismic hazard map with a recurrence period of 475 years from the SESAME project. From the figure it is evident that the areas surrounding the Aegean Sea are considered to be the most prone area for large ground shaking in Europe. The estimated values for peak ground acceleration in the study area of this thesis are found to be between 0.3-0.4 g on the bedrock - correlating well with the results of the GSHAP project.

Since the probabilistic seismic hazard map produced in the SESAME project covers an even larger region than the map produced in the GSHAP project, the resolution is not any better. There is even less detail in predicted ground acceleration inside the box covering the study area of this thesis (figure 2.14). A closer look into the northwestern part of the study area reveals that larger peak ground acceleration is expected on the Greek islands Lesbos and Chios and to some extent also on the Karaburun Peninsula than on the mainland of western Turkey. In the map from the SESAME project - as it

was the case for the hazard map produced in the GSHAP project - there is not enough detail to identify the single faults in the vicinity of İzmir.

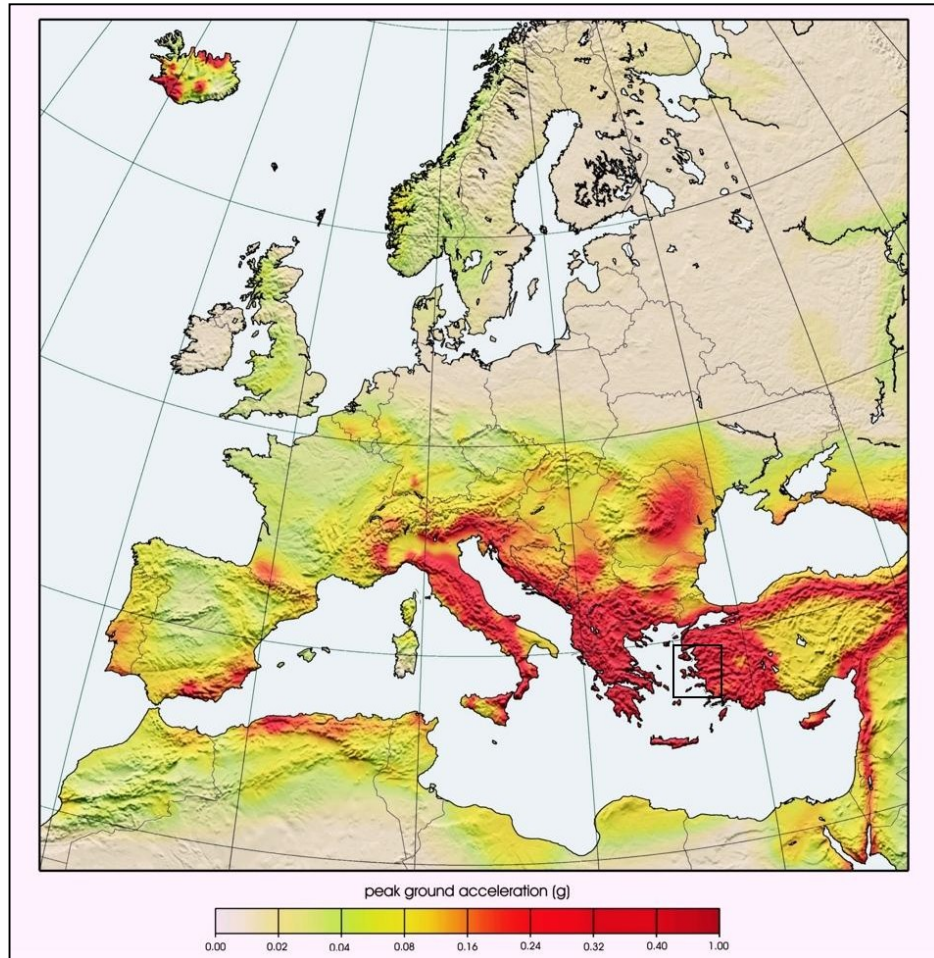


Figure 2.14: Probabilistic seismic hazard map from the SESAME project for a return period of 475 years (10% exceedance within 50 years). The values for ground motions are given in g. From Jimenez et al. (2003). The study area of this thesis is approximately marked by a black square, placed by the author.

İzmir Earthquake Master Plan

Due to the significant risk in the area of İzmir an earthquake master plan was prepared in 2000 in order to calculate socio-economic losses due to a future earthquake. This work is done on the basis of a probabilistic seismic hazard analysis for the local area around İzmir. The analysis has been conducted in cooperation between the Istanbul Technical University and the Boğaziçi University (Erdik et al., 2000).

The seismic hazard analysis was based on a study of the geology and tectonics as well as the earthquake occurrence in the area around İzmir. The results are given both as intensities and in values of g. In figure 2.15 a probabilistic seismic hazard map is shown for a recurrence period of 475 years, with the ground motions given as intensities in the range of 6.5-7.5 on the modified Mercalli Intensity Scale (MMI).

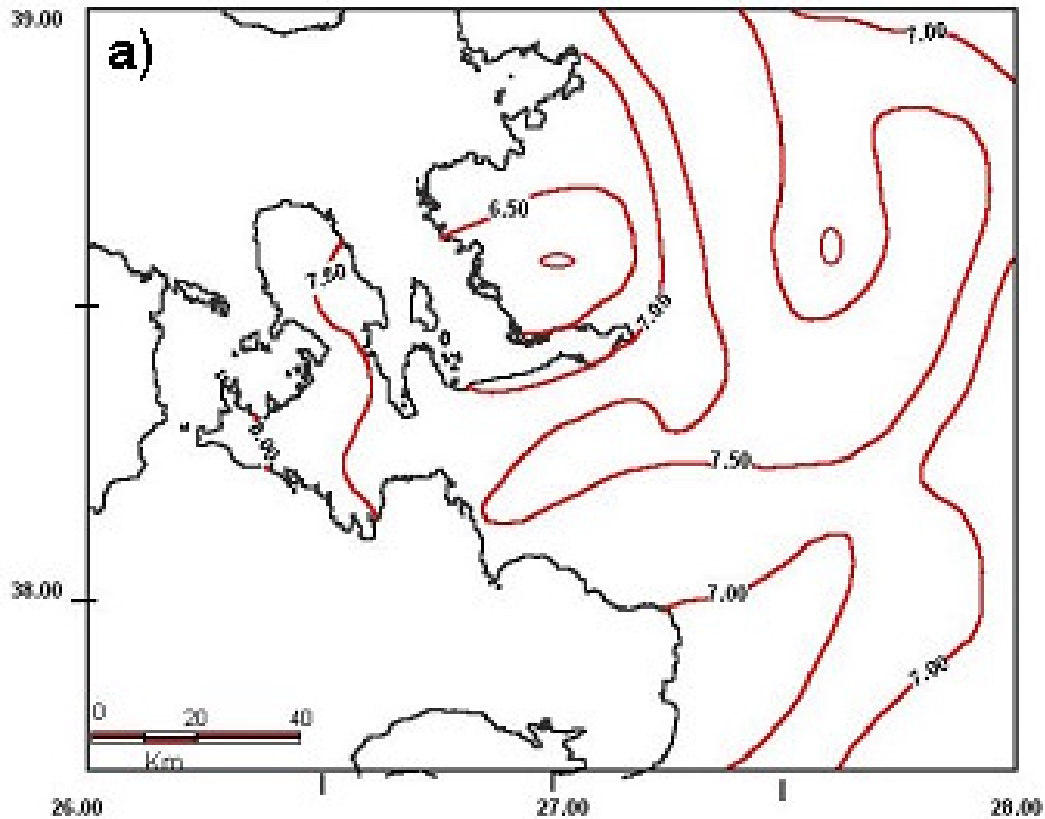


Figure 2.15: Probabilistic hazard map for the area around İzmir, with a recurrence period of 475 years (10% probability of exceedance during 50 years). The ground motion is given as intensities. From Erdik et al. (2000).

These values are comparable with previous records of historical earthquakes for the area (Papazachos et al., 1997). It is noted that intensities are also given in $\frac{1}{2}$, which is not in accordance with the definition of the Modified Mercalli Intensity scale.

The pattern of the intensity isolines is not meaningful when taking the location of the active faults (Emre et al., 2005b) into account. An increase of ground shaking towards Chios (west) and towards the mainland to Turkey (east) seems to be predicted with minimum values of ground shaking around the center of İzmir and in the area northwest of İzmir towards Foça. This is in contrast with the prediction given in the GSHAP and SESAME projects. The very detailed intensity isolines make the picture even more confusing, and do not give any reasonable insight.

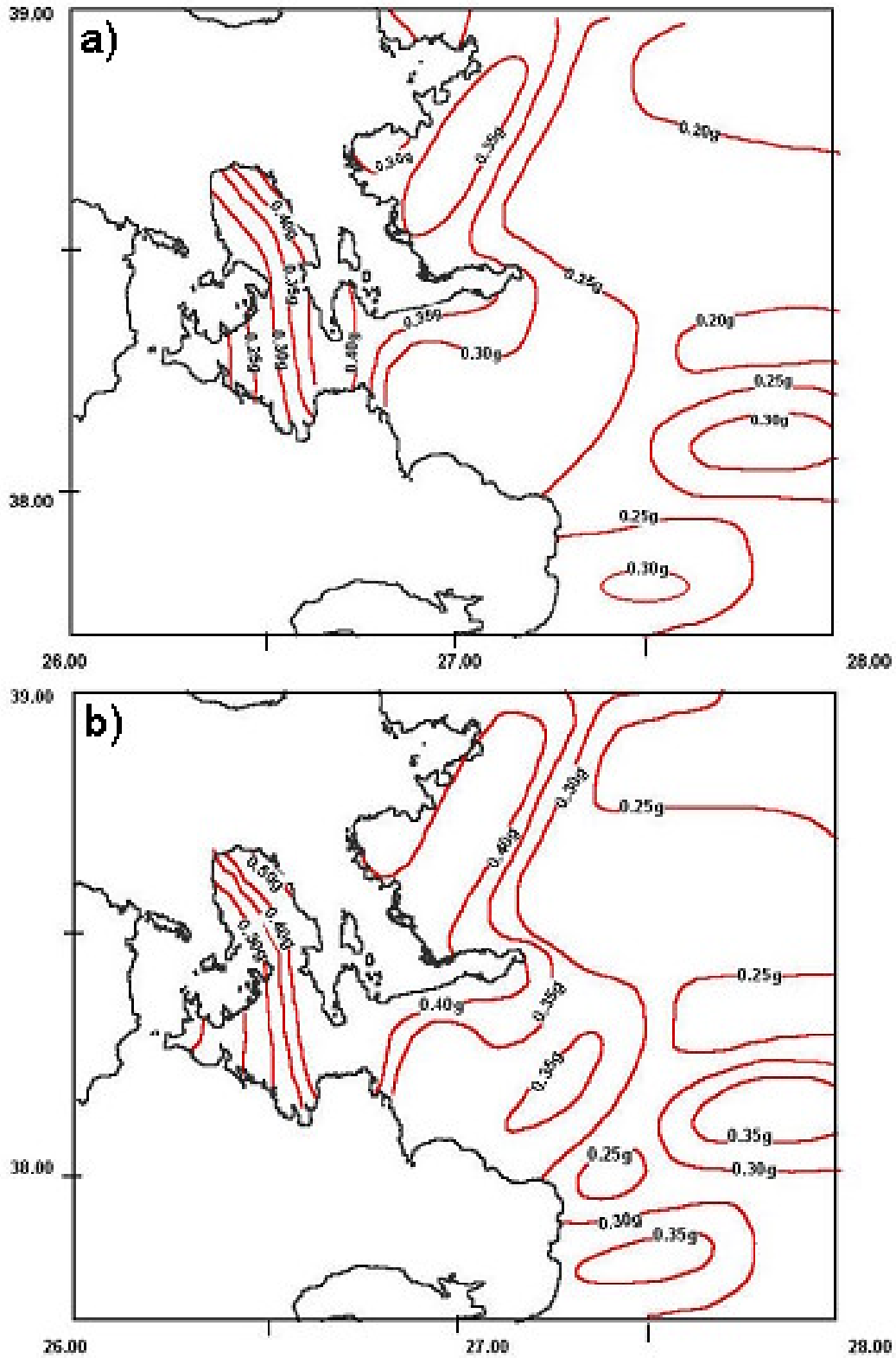


Figure 2. 16: Probabilistic seismic hazard map from the İzmir Earthquake Master Plan project for a return period of 475 years (10% exceedance within 50 years). The values for ground motions are given in g. (a) is calculated for hard rock and (b) is calculated for soft soil. From Erdik et al. (2000).

In figure 2.16 the peak ground motions for the İzmir area are shown for a recurrence period of 475 years (10% probability of exceedance within 50 years) for hard rock (a) and soft soil (b). The values of the peak ground motion are, in the case where the attenuation relation used is for hard rock, in the range of 0.2-0.4 g on the bedrock, whereas the peak ground accelerations are slightly higher in the case of the soft soil attenuation relation, which is to be expected.

The maps showing peak ground acceleration in figure 2.16 give a better picture of the hazard than the intensity map in figure 2.15 and can partially be correlated with the local tectonics in the surrounding area of İzmir. In figure 2.16 (a and b) north-south striking isolines can be observed for the peak ground acceleration along the Karaburun Peninsula, with the highest values surrounding the Gülbahçe fault identified by Emre et al. (2005). Further towards the east another set of north-south striking isolines is seen, which deviate to an east-west trending orientation along the southern coast of İzmir; these lines correspond to the location of the Seferihisar fault and the İzmir fault (see figure 2.6). There is however no indication of the Tuzla fault, located to the east of the Seferihisar fault in the hazard maps.

The hazard maps showing peak ground acceleration also agree with the two more regional studies with respect to the expected increased ground motion northwest of İzmir towards Foça.

2.3.2 Methods to determine seismic hazard estimations

Seismic hazard can be obtained either as a probabilistic or a deterministic analysis. In this thesis deterministic seismic hazard analysis is conducted, and the methodology used to obtain the analysis is described chapter 3. In the following, various methods of seismic hazard analysis are briefly described with more emphasis on the deterministic approaches due to the scope of this thesis.

Probabilistic seismic hazard assessments

Probabilistic seismic hazard analysis for a given site yield the probability of exceeding a specified ground motion level within a specified time period. A

probabilistic seismic hazard analysis is built on an earthquake recurrence model. Such an analysis is set up in four steps: define the earthquake source, assess the recurrence relationship, estimate the ground motion attenuation, and finally determine the hazard at the given site. There are two basic assumptions concerning the earthquake recurrence in a probabilistic hazard analysis: a Poissonian or a time-dependent approach. In the Poissonian approach all earthquakes are independent, and an earthquake source therefore has no memory. This leads to the conclusion that earthquakes can occur anywhere inside the earthquake source zone irrespective of the past occurrence of earthquakes from the same source. In the time-dependent approach, on the other hand, the probability of occurrence of a future e.g. is dependent on the previous e.g. occurrence (also called renewal model). The recurrence relationship of an earthquake source indicates the chance that an earthquake of a given size will occur inside the source during a given time period. The most important difference between a probabilistic and a deterministic seismic hazard analysis is that in the probabilistic case the hazard is not defined by one controlling earthquake, which is the case in the deterministic seismic hazard analysis (Reiter, 1990).

Deterministic seismic hazard assessments

A deterministic seismic hazard analysis as opposed to the probabilistic seismic hazard analysis focuses on a single earthquake. The probability of occurrence of the earthquake is not taken into account. The effects of the assumed future earthquake are estimated either by a simple function of seismic attenuation based on existing relations or by ground motion simulations using complex dynamic or kinematic fault models. There are however several different methods to simulate ground motions, which are briefly described in the following. Dynamic ground motion modeling is based on rate and state dependent friction laws and a pseudo-dynamic approach (i.e. by using a kinematic representation with randomly varying parameters) and is outside the scope of this thesis.

The kinematic ground motion simulation methods can be divided into three main groups; deterministic (low frequencies), stochastic (high frequencies) (chapter 3.2.2) and hybrid (broad band). The deterministic approach uses a kinematic source model and requires the slip along the fault to be known (section 3.2.1). This method is only

successful for frequencies less than 3 Hz. In the stochastic approach the earthquake ground motion is modeled as random noise in the high-frequency range. The spectral shape is given by the simple ω^{-2} -model (Brune, 1970) (section 3.2.2). The hybrid method is a combination of the deterministic and stochastic methods, where the low-frequency wave propagation are modeled deterministically, while the high-frequency part is based on the stochastic method (Somerville et al., 1991).

One of the most common methods in kinematic simulations is Empirical Green's Functions (EGF) (Hartzell, 1978). The EGF method is the simplest way to take the fact that the combined effect of the source process and wave propagation path, which can not be predicted by simplified one-dimensional or purely stochastic modeling techniques, into account (see section 3.2.2). The main limitation of the method is that to conduct the ground motion simulation, records of small events in the area of the main shock are needed, to be considered as Green's functions. However, such records are rare, especially in areas of future large earthquakes (Kamae et al., 1998). In cases where previous large earthquakes and their aftershocks are recorded from the target fault rupture the method applies already existing recordings of aftershocks or small earthquakes from a previous main event in order to calculate the ground motions for this event. The requirements are that the used aftershocks are well distributed across the entire ruptured fault plane, of the same focal mechanism as the main event, and that each aftershock is recorded at the same station as the main event. The fault plane of the main event is then divided into a distribution of point sources. The ground motion for an aftershock closest to a given point source is used as the point source response. The simulated ground motion for the main event is then obtained by summing all the point source contributions, taking the phase delay into account. In this method it is important that the magnitude of the aftershock is small enough to satisfy the magnitude of the point source but also large enough to excite response from the earth (Hartzell, 1978).

Due to the limitations in the EGF method later studies have resulted in further improvement of this method, called the Hybrid Green's Functions (HGF). In this method synthetic Green's functions are computed, instead of adopting Green's functions from the aftershocks as in the EGF method. The synthetic Green's functions

are calculated based on a hybrid scheme, which combines different methods to calculate the low- and high-frequency of the ground motion, deterministically and stochastically respectively (Kamae et al., 1998). The main advantage of this method is obvious compared to the EGF, since the HGF method allows one to simulate ground motions for future earthquakes, even if records of previous earthquakes are not available.

The HGF method combines the advantages of the deterministic and stochastic modeling and simulates broadband ground motions. The method is able to incorporate complexities of the source, wave path and local site effects into strong ground motion simulations (Pitarka et al., 2000). Further development of the HGF method by e.g. Somerville et al. (1991), Pitarka et al. (2000) and Pulido et al. (2004) has improved the representation of the frequency dependent radiation pattern and geometrical spreading resulting in a better representation of the ground motions for the simulated earthquake.

In HGF method the high-frequency ground motions are simulated in a stochastic manner, following Boore (1983), see section 3.2.2. The acceleration amplitude of the obtained high-frequency part of the simulated Green's functions follows the ω^{-2} -model, with a high-frequency cutoff and a frequency dependent Q-value. The low-frequency part of the ground motion is calculated by assuming a point source and adopting a velocity model (1D or 3D) of the heterogeneous structure. The HGFs are then calculated by combining the low- and high-frequency ground motions. Finally the strong ground motions for the large earthquake are simulated by summation of the HGFs following the same approach as in the EGF method (Kamae et al., 1998).

The EGF and HGF methods are based on one-dimensional velocity models, however, if available 3D velocity structures can also be used for the wave propagation. Such a hybrid three-dimensional finite-difference method combines a complex source and wave propagation for a regional one-dimensional velocity model with site effects calculated for a local three-dimensional structure. In cases where 3D-velocity models exist for the entire wave path, three-dimensional finite difference schemes can also be used for the low-frequency part of the motion.

In this hybrid method of the three-dimensional finite-difference model the wave field is calculated in a local model containing a complex three-dimensional structure within a regional-structure medium. The method combines the source, path and the site effects in a two-step procedure. First the ground motions time-series are calculated for receivers in the regional area containing the local site of interest. This calculation is done for a one-dimensional crustal velocity structure, by e.g. one of the methods described above or the method adopted in this thesis described in section 3.2. The calculations are made for a seismic source located outside the site of interest and for a regional one-dimensional velocity model. The second step is a three-dimensional finite-difference scheme that is used to calculate the spectral amplifications within the study area for the local three-dimensional velocity structure. This approach makes it possible to calculate a full three-dimensional wave field. The local area with the detailed three-dimensional velocity structure usually comprises only a small fraction of the regional area considered in the first step. The hybrid method ensures that the boundaries around the local area are fully transparent in the second step, letting the seismic waves travel freely across the boundary (Sørensen et al., 2006).

New approaches in seismic hazard assessments

Most recently approaches in seismic hazard analysis are based on earthquake rupture forecasts integrated to a ground motion model (Field, 2007). Volume 78 of *Seismological Research Letters* (January/February 2007) is a special issue dedicated to earthquake likelihood models. In connection with earthquake rupture forecasts artificial seismic catalogs can be produced for areas where few previous records exist. This provides a significant advantage when conducting a probabilistic seismic hazard assessment. However, since this thesis is focused on the deterministic scenarios based on ground motion simulations, the earthquake rupture forecasts are considered to be outside its scope.

The method applied for obtaining the ground motion simulations in this study is described in detail in chapter 3.2.

3 Methodology

In this study seismic hazard in İzmir and the surrounding area is estimated based in ground motion simulations using earthquake rupture scenarios. The methodology used for the ground motion simulations is a hybrid approach and has been found to produce realistic results in previous studies, (Pulido and Kubo, 2004; Pulido et al., 2004; Sørensen et al., 2007).

The general theory for constructing waveforms is described in this chapter and the essential terminology is introduced. The specific methodology used in the study follows Pulido and Kubo (2004) and Pulido et al. (2004). Finally the parameters needed to conduct ground motion simulations are explained.

In order to keep track on the notations used in this chapter, there have been created a list with symbols and explanations, which is found in appendix B.

3.1 Waveform modelling

In order to simulate ground motions and thereby produce synthetic seismograms a basic model of the displacement field for the seismic waves and a description of each contribution that makes up the seismogram are needed, this is given in the following.

3.1.1 Basic model of a seismogram

A seismogram is combined of several contributors, which are needed in order to be able to construct seismograms and conduct ground motion simulations.

The ground motion felt at a station placed away from the fault is a function of the earthquake source, $x(t)$, the earth structure through which the seismic waves propagate, $e(t)$ and $q(t)$, the seismometer response to the seismic signal, $i(t)$, and the local site effects. The terms concerning the seismometer response and the local site effect will not be discussed in this section, since it is not possible to come up with a

general description of these; they vary with instrument and region. The two components describing the earth structure, $e(t)$ and $q(t)$, represent the elastic and anelastic wave propagation respectively. In the time domain the seismogram is expressed as a convolution of the different terms as given in equation 3.1.

$$u(t) = x(t) * e(t) * q(t) * i(t) * s(t) \quad \text{Eq. 3.1}$$

All contributors are dependent on the frequency, ω , of the seismic waves, and they can therefore both be represented in the time and the frequency domain. When equation 3.1 is transformed into the frequency domain, by Fourier transformation, the seismogram is given as the product of the different terms, given in equation 3.2.

$$U(\omega) = X(\omega) \cdot E(\omega) \cdot Q(\omega) \cdot I(\omega) \cdot S(\omega) \quad \text{Eq. 3.2}$$

(Stein and Wysession, 2003).

Earthquake source

When the distance from the fault to the station, Δ , is much larger than the length of the fault, L , a far-field approximation, the source can be represented as a point. In this case the fault is represented as a circular fault with radius L (Brune, 1970). However for the near-field case the following has to be taken into account.

The earthquake source, $x(t)$, is the source time function and it is the derivative of the seismic moment function, which describes the faulting process from the rigidity of the material, μ , the slip, $D(t)$, and the fault area, $S(t)$. The seismic moment function is given in equation 3.3.

$$M(t) = \mu D(t) S(t) \quad \text{Eq. 3.3}$$

(Stein and Wysession, 2003). If a fault slips instantaneously, the seismic moment function is a step function.

In the case of a *real* fault this is not described with a point source, and the rupture will occur along the length of the fault, giving rise to a more complicated source time function. If such a fault is described with point sources it can be compared to pearls on a string pushing each other indicating rupture of each single *sub-source*. However a pearl will not move or *rupture* if it is not influenced by the pearl before, except for the pearl representing the rupture initiation point. The total wave field of the rupture will therefore become a sum of each wave field radiated by each single sub-source.

The duration of the signal from the rupture along the fault, of length L , at a station located away from the fault therefore lasts from the time of the arrival of the wave-field from the rupture initiation point, till the end point of the fault has ruptured and the wave-field from this part of the source has reached the station. The rupture time, T_R , is described in figure 3.1 and equation 3.4.

$$T_R = L \left(\frac{1}{V_R} - \frac{\cos \theta}{v} \right) = \left(\frac{L}{v} \right) \left(\frac{v}{V_R} - \cos \theta \right) \quad \text{Eq. 3.4}$$

With $r \approx r_0 - L \cos \theta$, v is the wave velocity and V_R is the rupture velocity, which is typically 0.7 to 0.8 of the shear wave velocity, θ is the angle between the strike of the fault and r_0 .

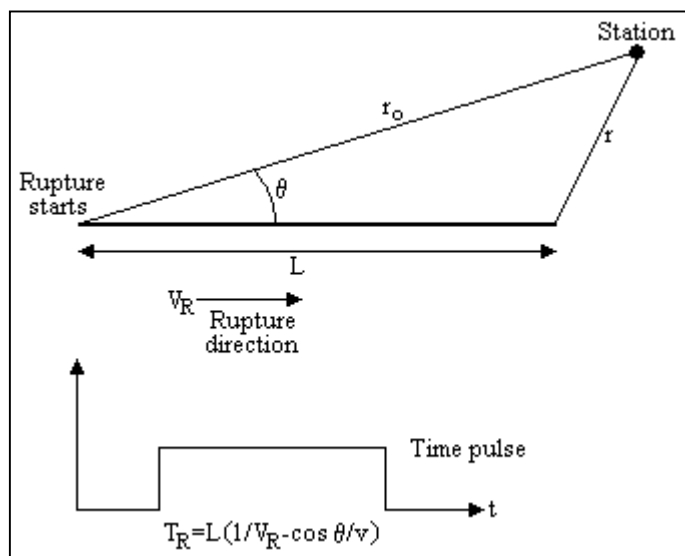


Figure 3.1: The source time function for a fault of length L depends on the azimuth and the ratio between rupture velocity and wave velocity. From Stein and Wysession (2003).

Another complication of the source time function is that slip does not occur instantaneously. The rupture needs a certain time before the rupture velocity is reached, this time is called rise time and is a function of slip. The rupture time from figure 3.1 and equation 3.4 therefore has to be convolved with the slip function describing the rise time of the rupture. The new

source time function is therefore described as a trapezoid or a ramp function.

From equation 3.4 it is observed that the seismic signal for an earthquake is different depending on at which azimuth the signal is obtained. This results in different shapes of the radiated pulse, but the area of the pulse is the same for all azimuths, since the same energy will arrive at the different stations, and the amplitude of the source time function is therefore inversely proportional with the source duration; this is pictured in figure 3.2.

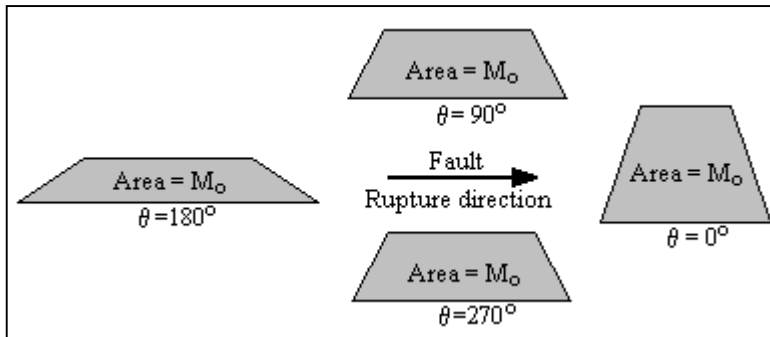


Figure 3.2: Sketch of the dependence of azimuth between station and fault and how the length of the source time function changes. From Stein and Wyssession (2003).

It is seen from figure 3.2 that the amplitude of the seismic signal is much higher, though with a shorter duration, at stations located in the direction (in front) of the rupture propagation.

Similarly, a longer signal is observed with lower amplitudes in the opposite direction. This effect is known as directivity of the seismic waves, and the largest ground motions will therefore be felt in the direction of the rupture, also known as the directivity effect.

Body wave radiation patterns

Motion or slip along a fault plane can be described with a pair of force couples, which is a pair of forces acting in opposite direction. However, two pairs of forces can, equally explain the resulting four quadrants where, two are compressional and two are dilatational. Slip along a fault plane will result in two pairs of forces located perpendicular to each other due to symmetry. In the same way will motion along two perpendicular fault planes result in the same representation of forces, see figure 3.3. Two pairs of forces is called a double couple (Stein and Wyssession, 2003).

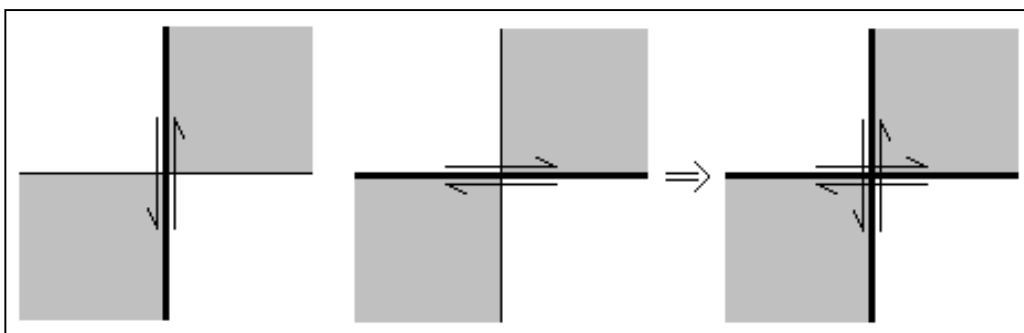


Figure 3.3: Motion along two perpendicular faults results in the same pattern of areas for which there is experienced compression and dilation. The slip from an earthquake is therefore represented with a set of forces called a double couple as illustrated to the right in the figure.

The areas of compression and dilation are determined from observations of first motions on seismograms recorded at various azimuths, θ , and distances, Δ , to the fault. The first motion on a seismogram reveals the polarity of the first body wave

when it arrives at the station, which can either be up, for compressional motion, when the material near the fault moves towards the station, or down for a dilatational motion, when the movement is away from the station. This polarity changes according to the direction (azimuth) in which the recording station is located with respect to the fault (Stein and Wysession, 2003).

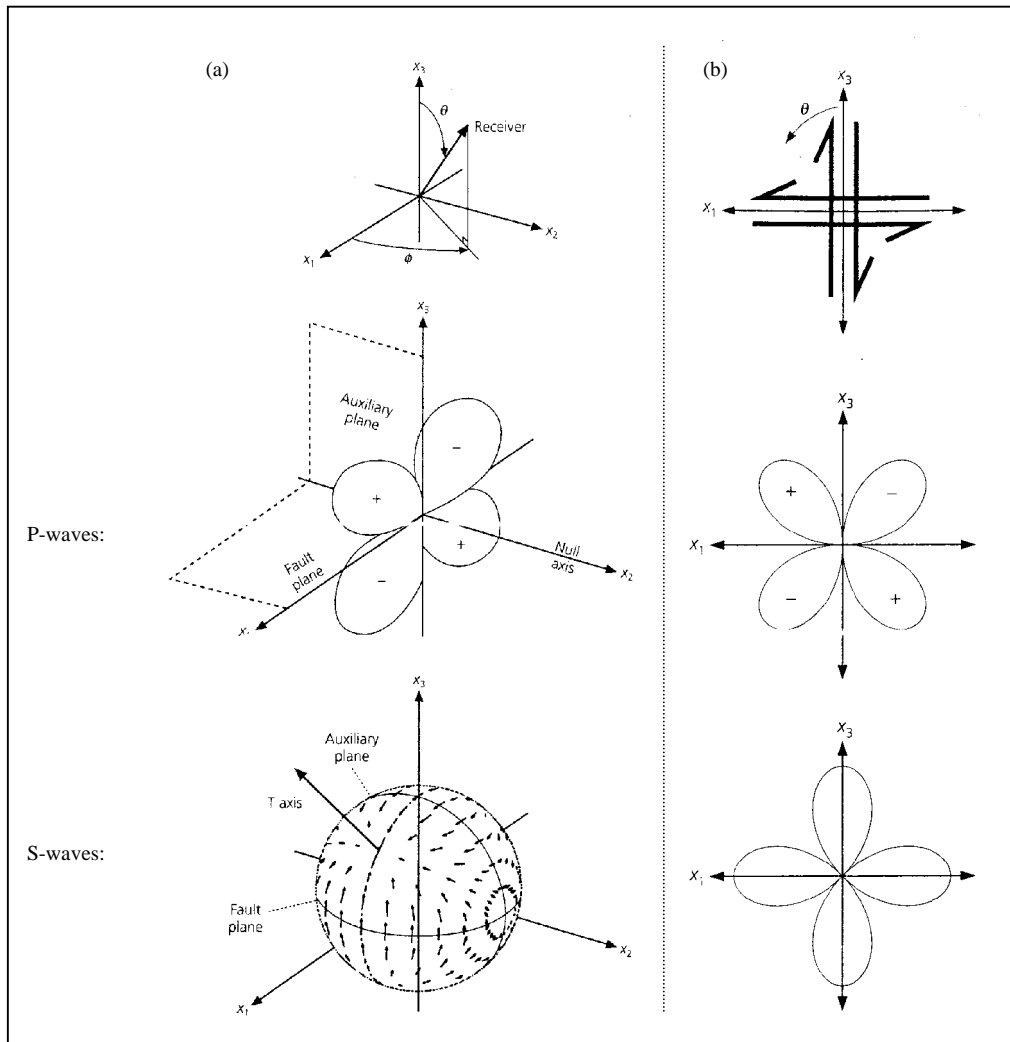


Figure 3.4: (a) Body wave radiation pattern for a double couple source in spherical coordinates. The radiation pattern for the P-waves is four lobed and it goes to zero at the nodal planes while the S-wave radiation pattern describes a vector displacement field. (b) The radiation amplitude patterns for P- and S-waves with the double couple (top) placed in the x_1 - x_3 plane about the x_2 plane. From Stein and Wysession (2003), modified by the author

This the first motions will separate the area around the fault into four quadrants, as it is also illustrated in figure 3.3, two compressional and two dilatational. The divisions between the quadrants represent the fault plane and a plane perpendicular to it called the auxiliary plane, again related to the double couple concept. The double couple

representation exists due to the fact that on seismic records it is not possible to differentiate whether one or the other nodal plane causes the motion. By plotting the first motions patterns of compression and dilation as observed in figure 3.3, the two nodal planes defining the four quadrants, can be obtained. This is called the earthquake focal mechanism, which describes the geometry of the fault.

The radiated energy from a fault to a given azimuth depends on the focal mechanism. As it is shown in figure 3.4 P- and S-waves are radiated differently with respect to the fault plane. The displacement field for a seismic wave is therefore dependent on the radiation pattern of the seismic wave for which the displacement is calculated and consequently different for P waves, SH and SV waves. Elastic radiation resulting from a double couple consists of a pair of forces of which one couple is oriented along the slip of the fault on each side with opposite directions, and the other couple is oriented correspondingly on either side of the auxiliary plane (Stein and Wysession, 2003). The radiation patterns and radiation amplitude pattern for P- and S-waves are given in figure 3.4.

From seismic source theory the displacement field from a compressional wave is given along the radial component, r , and is given in equation 3.5.

$$u_r = \frac{1}{4\pi\rho\alpha^3 r} \dot{M}(t - r/\alpha) \sin 2\theta \cos \phi \quad \text{Eq. 3.5}$$

First part of equation 3.5 is the amplitude term. This is dependent on the density, ρ , and the P-wave velocity, α , of the medium through which the seismic wave travels. The amplitude term is also dependent on the inverse of the distance (r) from the source to the station due to geometrical spreading. The term $\dot{M}(t)$ is the seismic moment rate function or source time function. This describes the pulse propagation away from the fault with the P-wave velocity and arrival at the station at time $t-r/\alpha$. The term involving sine and cosine is the P-wave radiation pattern, as given in figure 3.4(a) (Stein and Wysession, 2003).

The shear wave displacement field, equation 3.6, is similar to the P-wave displacement field given in equation 3.5, but since shear waves are divided into two

components, SH and SV, the displacement field, u , is equally given in two components: along the θ and ϕ components.

$$u_{\theta} = \frac{1}{4\pi\rho\beta^3 r} \dot{M}(t - r/\beta) \cos 2\theta \cos \phi \quad \text{Eq. 3.6a}$$

$$u_{\phi} = \frac{1}{4\pi\rho\beta^3 r} \dot{M}(t - r/\beta) (-\cos \theta \sin \phi)$$

Eq. 3.6b

Where β is the S-wave velocity (Stein and Wysession, 2003).

Anelastic attenuation

The Q -term is the anelastic attenuation of the seismic waves due to energy loss when they are converted into heat. This is described in equation 3.7, which is an exponential function dependent on the frequency of the seismic waves.

$$f(t) = A e^{i\omega t} e^{-\omega/2Q} \quad \text{Eq. 3.7}$$

A is an amplitude term and ω is the frequency. In this equation Q is the attenuation factor, and it is dependent on the crustal properties for which the ground motion simulation is conducted. From equation 3.7 it is seen that high frequencies are damped more than low frequencies, and that a high Q indicates a slow decay of the waves (Stein and Wysession, 2003).

Q is a frequency dependent attenuation, given in equation 3.8, and it is empirically determined for a given region.

$$Q = Q_0 \cdot \omega^{\epsilon} \quad \text{Eq. 3.8}$$

Q_0 is the attenuation coefficient. The more complex the structure of the crust is the higher is the attenuation.

Elastic earth structure

The elastic structure represents the effects of reflections and transmissions along the ray path. The term mainly concerns interactions near the earth's surface.

For deep earthquakes the surface reflections, and other later arrivals such as reflected, refracted and diffracted waves arrive at the station much later than the direct P-wave, and the modeling of the P-wave does not have to take these arrivals into account. At distances of $30^\circ < \Delta < 90^\circ$ from the source triplications from the mantle and the

structure of the core of the earth can be ignored. Accordingly, the structure parameter can be ignored when it comes to deep earthquakes and stations located at large distances from the source, and hence the first pulse of the seismogram can be described as a function of the earthquake source, the attenuation and the instrument response alone (Stein and Wysession, 2003).

When it comes to shallow earthquakes, as in this study (hypo-center depth is less than 15 kilometers for all the conducted earthquake scenarios), the arrivals of reflections from the earth's surface will arrive almost at the same time as the first direct wave arrival. Therefore, when modeling the first few seconds of a seismogram, modeling the sum of the first three arrivals; P, pP and sP, is needed. By using equations 3.1 and 3.2 it is possible to model synthetic body waves. In the case of an initial P-wave arrival at a distance of $30^\circ < \Delta < 90^\circ$ from the source, the displacement as a function of time, t , distance, Δ , and azimuth, θ , is given by the following.

$$u(t, \Delta, \theta) = i(t) * q(t) * \frac{M_0}{4\pi\rho_h\alpha_h^3} \frac{g(\Delta)}{a} C(i_0) \times$$

$$\left[R^P(\theta, i_h)x(t - \tau^P) + R^P(\theta, \pi - i_h)\Pi^{PP}(i_h)x(t - \tau^{pP}) \right. \tag{Eq. 3.9}$$

$$\left. + R^{SV}(\theta, \pi - j_h) \frac{\alpha_h \cos i_h}{\beta_h \cos j_h} \Pi^{SP}(j_h)x(t - \tau^{sP}) \right]$$

(Stein and Wysession, 2003).

The displacement of the sum of the first three arrivals is a function of the instrument response and the attenuation. Furthermore, the signal consists of a complicated term taking the source and structure into account.

The first term ($M_0/(4\pi\rho_h\alpha_h)$) is the amplitude scale factor, and it is dependent on the depth of the source (hypo-center depth). The fraction $g(\Delta)/a$, where a is the earth's radius, describes the geometrical spreading of the rays. The term $C(i_0)$ corrects the signal amplitude for the effect of the free surface, where the rays arrive at an angle of incidence, i_0 , to the receiver. Three terms corresponding to each of the three arrivals for which the displacement is modeled are shown inside the brackets. These terms all consist of the source time function, $x(t)$, where τ^x is the travel time for the ray of interest and $R(\theta, i/j)$ is the radiation pattern for the specific wave. The radiation

pattern is dependent on the take-off angle (i for P-waves and j for S-waves), the azimuth to the station, θ , and the fault geometry parameters strike, ϕ , dip, δ , and rake, λ . The amplitude of the reflected phases also include the plane wave potential reflection coefficients at the free surface, $\Pi^{PP}(i_h)$ and $\Pi^{SP}(j_h)$; these depend on the angle of incidence. Since SH waves arrive later, they are not taken into consideration in equation 3.9, but they are modeled in a similar way, just by summing S and sS waves instead of P, pP and sP waves.

3.2 Ground motion simulation

Being able to describe the displacement field of seismic waves, the method used for conducting ground motion modelling in this thesis will be described in the following. These simulations are calculated for different frequency ranges, and the methodology follows the approach of Pulido and Kubo (2004) and Pulido et al. (2004). A hybrid method is applied in order to model ground motions on various faults in the area around İzmir. The simulation is made in the frequency range from 0.1 to 10 Hz and is combined of a deterministic simulation at low frequencies (0.1-1.0 Hz) and a semi-stochastic simulation at high frequencies (1-10 Hz). In order to get a smooth transition from the low to the high frequency domain, a frequency-dependent radiation pattern is applied, ensuring that the theoretical double-couple at low frequencies is smoothly transformed into a uniform radiation pattern at higher frequencies. Finally, the different contributions are summed. The different parts of the modelling are combined from previous studies, which will be described in the following paragraphs.

3.2.1 Low-frequency ground motion

The low-frequency ground motion (0.1-1.0 Hz) is obtained by subdividing the fault plane into several subfaults that are treated as several independent point sources, see figure 3.5.

The total ground motion is found by adding the different contributions assuming a constant rupture velocity within each subfault. The seismograms for the low-frequency motion are obtained numerically by the discrete wave number theory

developed by Bouchon (1981). This method computes the wave propagation in a flat-layered velocity structure for a given focal mechanism and source time function and is described below.

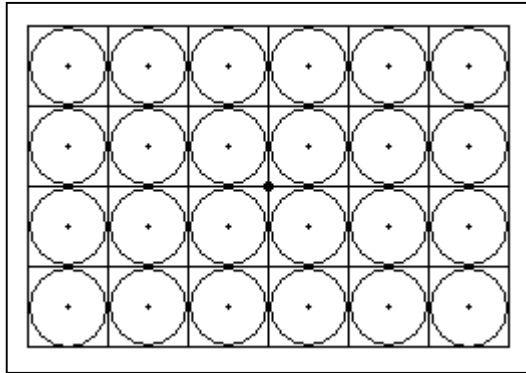


Figure 3.5: Geometry of the point source array. In the center is placed source representing the rupture initiation point.

Bouchon (1981) calculates Green's functions for an elastic layered media. A Green function is a special type of function that is used to solve inhomogeneous differential equations with boundary conditions. The Green's functions for a layered media are given as a double integral over the frequency and the horizontal wave number, k . In the study made by Bouchon (1981) it is shown that

the integral over the wavenumber in the Green's functions can be exactly represented by a discrete summation. This theory is called the *discrete wave number theory*. The theory is achieved by adding an infinite set of specified circular sources to a point source. The circular sources are placed around the point source at equal and specific distance from another. The distance between the point sources is dependent on the time the source needs to respond, and it is therefore a function of the wave velocity and the distance between the sources. This distance determines the discretized set of horizontal wavenumbers and will therefore give the solution to the problem.

The displacement field produced by an earthquake is used to compute the seismograms for the low-frequency domain. In order to obtain solutions for the displacement field it is necessary to start with the compressional displacement potential given for the elastic wave field radiated for a single pulsating point source in a homogeneous medium. When the displacement potential for a single source is obtained a superposition of all the contributions to the radiated displacement potential due to the infinite set of sources placed in the source array is computed. The total radiation potential is therefore given as a sum over all the individual radiation potentials from the contributing sources.

Now a source array is obtained, however in the end a source placed at the origin (corresponding to the hypocenter of the fault) is added. This ensures that the elastic wave field from the entire source array is obtained. When the displacement potential is obtained the displacement is calculated by partial differentiation.

The solutions found by Bouchon (1981) for discretization in the one-dimensional wave field k are throughout the study compared to the discretization in the two-dimensional wave field of k_x and k_y , which was developed by Bouchon (1979). The results from both studies are in good agreement, which indicates a great accuracy of the two methods, and it is therefore reasonable to use the 1D method instead of the 2D method. Furthermore, there have been made tests of the solutions obtained, which compare the obtained solution for discretization in the k space with discretization in the k_x and k_y space. These tests are based on simple flat-layered models of the earth's crust. In the case where several layers are present, which is normally the situation, the discretization method using both k_x and k_y become prohibitive because of the large numbers of operations required. The one-dimensional discretization is therefore used and gives reasonable results. The cut-off frequency used in the study is 3 Hz, and the method has therefore been proven to work for low frequencies where the radiation pattern still can be represented by a double-couple representation (Bouchon, 1981).

3.2.2 High-frequency ground motion

The high frequency ground motion (1-10 Hz) is calculated from a finite asperity model as the case for the low frequency ground motion, see figure 3.5. The point source ground motions are however calculated using the semi-stochastic approach of Boore (1983). Finally the summation of the high-frequency ground motion for each point source is obtained by applying the empirical Green's function method (Irikura, 1986).

Semi-stochastic model

Boore (1983) calculates a stochastic simulation of high-frequency ground motion, which is based on seismological models of the radiated spectra. The simulations use both frequency- and time domain and the aim of the method is to filter a suite of

windowed stochastic time series in such a way that the amplitude spectrum equals a specified spectrum on average. The method is a combination of empirical and predictive methods, and the idea was to develop a method in order to calculate time series from windowed and filtered Gaussian noise, for which the amplitude spectrum is comparable with an acceleration spectrum, up to a specified cut-off frequency. The method only considers shear-wave contributions to the ground motion, since these waves dominate the ground motion, especially on the horizontal component. In the following, the method developed by Boore (1983) is outlined.

To obtain transient time series with a spectrum matching on average with a specified amplitude spectrum windowing a time sequence of a band-limited random Gaussian white noise - having zero mean and the variance chosen to give unit spectral amplitude on the average - is conducted. The spectrum of the time series is then multiplied with a specific chosen spectrum in order to obtain the form of this spectrum. Afterwards it is transformed back into the time domain yielding the final time series.

This method requires a spectral shape as a function of earthquake magnitude, which is called the target spectrum. It is assumed that the cut-off frequency is not dependent on the earthquake size. The two parameters, seismic moment, M_o , and corner frequency, f_c , control the shape of the spectra for different earthquake sizes. These parameters are related to each other by equation 3.10.

$$f_c = 4.9 \cdot 10^4 \beta \cdot \left(\frac{\Delta\sigma}{M_o} \right)^{1/3} \quad \text{Eq. 3.10}$$

where f_c is in Hz, β is the shear wave velocity in kilometres per second, $\Delta\sigma$ is the stress drop in MPa and the seismic moment, M_o , is given in Nm (Brune, 1970). The stress drop is thought as a parameter controlling the strength of the high-frequency radiation (Boore, 1983).

The method to simulate high-frequency ground motion is a unique combination of stochastic simulation and physically based spectral amplitudes and record duration. The method was tested by comparing simulated spectra with values obtained from many strong motion records as well as smaller earthquakes.

The acceleration spectrum to calculate the high-frequency ground motion is based on a source spectrum of the ω -squared model. The method can be applied to the ground motion simulation from several small events, because the source size of the event is small enough to neglect the rupture propagation effect (Kamae et al., 1998). In the model developed by Boore (1983) there is a problem with the average radiation pattern, which can differ up to 10-20%, depending on whether an equal weighting for the whole focal sphere is used and whether the rms or mean radiation pattern is applied. This problem has later been taken care of by Pulido and Kubo (2004), and their method is described in section 3.2.3.

Empirical Green's functions

The empirical Green's method was originally given by Hartzell (1978), and has later been improved by Irikura (1986). The improved method accounts for the problems arising when combining source process and wave propagation path (Kamae et al., 1998).

In the method proposed by Irikura (1986) the ground motion of a large earthquake can be represented as a superposition of the ground motion records from small events as the rupture of single subfaults shown in figure 3.4. The ground motion is given as:

$$U(t) = C \sum_{i=1}^N \sum_{j=1}^N \frac{\Delta}{r_{ij}} F(t - t_{ij}) * u(t) \quad \text{Eq. 3.11}$$

$$t_{ij} = \frac{r_{ij} - r_0}{\beta} + \frac{\xi_{ij}}{V_R} \quad \text{Eq. 3.12}$$

$$F(t) = \delta(t) + \frac{1}{n} \sum_{k=1}^{(N-1)n'} \delta \left[t - (k-1) \frac{\tau}{(N-1)n'} \right] \quad \text{Eq. 3.13}$$

here $U(t)$ is the ground motion for the large event and $u(t)$ is the observed ground motion for a small event used as the empirical Green's function. The terms Δ , r_{ij} , r_0 and ξ_{ij} are the distances from the site to the hypocenter of a small event, from the site to the (i, j) subfault, from the site to the starting point rupture on a fault plane of a large event and between the starting point rupture and the (i, j) subfault respectively. The shear wave velocity is given by β , and V_R and τ denotes the rupture velocity and the rise time of the large event respectively. C is the stress drop ratio of the large and the small events and $F(t)$ is a stochastic component included in the speed of the

rupture propagation in order to simulate the heterogeneities in the kinematics of the rupture (Pitarka et al., 2000). In the expression for $F(t)$ n' is an arbitrary integer number, shifting artificial periodicity to a frequency higher than that of interest. N is a scaling parameter given as:

$$N = \left(\frac{M_{0l}}{C \cdot M_{0s}} \right)^{\frac{1}{3}} \quad \text{Eq. 3.14}$$

with M_{0l} and M_{0s} as the seismic moments for the large and small events respectively.

3.2.3 Frequency-dependent radiation pattern

The radiation pattern for low-frequency ground motion follows the theoretical double couple, whereas the radiation pattern for high-frequency ground motion is isotropic and spherical (Pitarka et al., 2000). This variation in radiation pattern with frequency for a SH-wave for a point source with a pure strike-slip mechanism is shown in figure 3.6.

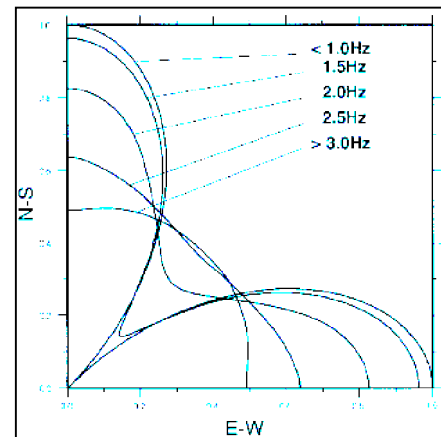


Figure 3.6: Frequency-dependent SH-wave radiation pattern for a point source with a pure strike-slip mechanism (Pitarka et al., 2000).

To be able to take the variation of the radiation pattern for SV and SH waves into account Pulido and Kubo (2004) developed a method, which gives a smooth transition from the low-frequency pattern to the high-frequency pattern. As it is seen in figure 3.6 the variation in the smooth transition is needed in the intermediate frequency interval from 1 to 3 Hz, where the pattern changes from a pure double-couple representation to an isotropic spherical pattern. The method developed insures that the radiation-pattern coefficient is no longer dependent on the source-receiver azimuth and take-off angle as the frequency increases. The paragraphs below are based on the work done by Pulido and Kubo (2004).

The traditional radiation pattern coefficients for SV and SH waves are given as:

$$F^{SV} = F_m(\phi, \delta, \lambda, i, \theta) = \frac{[(\gamma \cdot n)(\dot{\vec{u}} \cdot \hat{p}) + (\gamma \cdot \dot{\vec{u}})(n \cdot \hat{p})]}{\dot{\vec{u}}}$$

$$F^{SH} = F_m(\phi, \delta, \lambda, i, \theta) = \frac{[(\gamma \cdot n)(\dot{u} \cdot \hat{\phi}) + (\gamma \cdot \dot{u})(n \cdot \hat{\phi})]}{\dot{u}} \quad \text{Eq. 3.15}$$

(Aki and Richards, 2002). ϕ , δ and λ is the strike, dip and rake respectively at a receiver with take-off angle i and azimuth θ . In the second expression for the radiation pattern coefficient γ is the unit vector at the source, directed along the ray path, n is the fault normal and \dot{u} is the velocity evaluated in $(t-r/\beta)$. The vectors \hat{p} and $\hat{\phi}$ denote the SV and SH directions. The frequency-dependent radiation pattern used in the ground motion simulations is given in equation 3.16.

$$R_{pm}(i, \theta, \omega) = F_m(\phi, \delta, \lambda, i, \theta) \quad \text{for } \omega \leq \omega_1 \quad \text{Eq. 3.16A}$$

$$R_{pm}(i, \theta, \omega) = F_m(\phi, \delta, \lambda, i, \theta) + \left[\frac{R_{S,ave}}{\sqrt{2}} - F_m(\phi, \delta, \lambda, i, \theta) \times \frac{(\omega - \omega_1)}{(\omega_2 - \omega_1)} \right] \quad \text{for } \omega_1 < \omega < \omega_2 \quad \text{Eq. 3.16B}$$

$$R_{pm}(i, \theta, \omega) = \frac{R_{S,ave}}{\sqrt{2}} \quad \text{for } \omega \geq \omega_2 \quad \text{Eq. 3.16C}$$

in which $R_{S,ave}$ is the average radiation pattern coefficient for the total S-wave. This is calculated for all rays departing in the upper focal sphere ($\theta = 0^\circ$ to 180°) and is given in equation 3.17 by Boore and Boatwright (1984). The factor of square root 2 is due to the partitioning of the S-wave into SH and SV components.

$$R_{S,ave} = \left[\sum_{m=SH,SV} \left(\frac{\int_{\pi/2}^{\pi} \int_0^{2\pi} F_m(\phi, \lambda, \delta, i, \theta) \sin i \cdot d\theta \cdot di}{\int_{\pi/2}^{\pi} \int_0^{2\pi} \sin i \cdot d\theta \cdot di} \right) \right] \quad \text{Eq. 3.17}$$

The model for the transition of the radiation pattern has been tested and proven to efficiently remove the radiation pattern coefficients' dependence on take-off angle, i , and azimuth, θ , with increasing frequency (Pulido and Kubo, 2004). Also the radiation pattern for frequencies above 3 Hz is found to be completely isotropic, and the frequency range for where the frequency-dependent radiation pattern is used is therefore chosen to be 1-3 Hz in the conducted study around İzmir.

With the frequency-dependent radiation pattern coefficient the ground motion for high frequencies at a receiver, i , is calculated by the use of equation 3.18:

$$A_m(\omega) = \frac{R_{pm}(i, \theta, \omega) \cdot M_o \cdot S(\omega, f_c) \cdot F_S e^{-\pi \cdot \omega \cdot \Delta / Q(\omega) \beta} \cdot P(\omega, \omega_{max})}{4\pi\rho\beta^3 \Delta} \quad \text{Eq. 3.18}$$

which is the m 'th component of the acceleration Fourier spectrum for a point source, and can be compared with the displacement field given in equation 3.9. In equation 3.18, M_o is the point-source seismic moment, $S(\omega, f_c)$ is the ω -squared source model, with the corner frequency f_c which is given in equation 3.10, F_S is the amplification due to the free surface, Δ is the distance between the source and the receiver and $P(\omega, \omega_{max})$ is the high-frequency cut-off of the point-source acceleration spectrum. In order to calculate the ground motion an average asperity radiation pattern coefficient is found for all the ray paths between the point sources on the asperity and the receiver at every frequency (Pulido and Kubo, 2004).

Using the method described above it is possible to calculate the wave propagation in a flat-layered crustal velocity structure for at particular focal mechanism and source moment function. The point source moment function is given as

$$M(t) = \frac{M_o}{2} \cdot \left(1 + \tanh\left(\frac{4 \cdot (t - \tau_a / 2)}{\tau}\right) \right) \quad \text{Eq. 3.19}$$

This is a smooth ramp function, and M_o is the source seismic moment, t is the rupture time and τ_a is the asperity rise time (Pulido and Kubo, 2004).

3.3 Parameters used in ground motion simulations

When applying the above described method to an area several parameters are needed: regional, finite fault model parameters and parameters related to the simulation method.

The regional parameters are a velocity structure (1D) and an attenuation relation for the area of interest in order to be able to give an estimate of the wave-propagation of the seismic waves that are produced in the earthquake scenario.

The finite fault model parameters are the geometry of the fault and values for the rupture velocity and rise time. An earthquake results in a slip pattern, where there will be areas of the fault plane experiencing a larger slip than other parts. This is described

as asperities, and these can for past earthquakes be found by waveform inversions such as the case of the 2000 Tottori and 2004 Sumatra earthquakes (Pulido and Kubo, 2004; Yagi, 2004). In a predictive manner situations like the future Istanbul earthquake and in this study where the last large earthquake occurred before instrumental time, estimates of the locations of the high slip area, and thereby the locations of the asperities on the fault plane are needed. The high slip area of the fault is an area that experience a higher stress drop compared to the rest of the fault plane. Ideally, stress drop for both high and low slip areas should be known as well as the magnitude of the simulated earthquake.

The parameters determined in the method are the different frequency band and the maximum frequency for the simulations. In this study the low-frequency band is from 0.1-1.0 Hz and the high-frequency band is 1-10 Hz, with a frequency-dependent radiation pattern in the range of 1-3 Hz, corresponding to what is observed in figure 3.6. The maximum frequency for which ground motion simulations are made is 10 Hz. All these frequencies are taken from the examples of previous studies (Pulido and Kubo, 2004; Pulido et al., 2004; Sørensen et al., 2007).

All the earthquake rupture scenarios prepared in this thesis are described in chapter 4.4. To each description follows a sketch of the assumed fault plane and a table summarizing the parameters used in the earthquake scenario. In table 3.1 a similar table is given. This table, however, contains the symbols of the parameters in order to make it possible to relate the symbols with the equations given in the previous sections.

Table 3.1: Table similar to the tables given in chapter 4.4, which summarizes the parameters used in the earthquake rupture scenarios. In this table the symbols for the different parameters are given.

	Symbol
Moment magnitude	M_w
Seismic moment	M_0 [Nm]
Fault plane solution	ϕ [°]/ δ [°]/ λ [°]
Hypocenter depth	h [km]
Average stress drop	$\Delta\sigma$ [Bar]
Asperity stress drop (high-slip)	$\Delta\sigma_{asp}$ [Bar]
Background stress drop (low-slip)	$\Delta\sigma_{bg}$ [Bar]
Rise time	τ [s]
Rupture velocity	V_R [s]
f_{max}	ω_{max} [Hz]
Q	$Q_0 \cdot \omega^\epsilon$

A complete list of symbols and explanations are given in appendix B.

4 Input parameters and earthquake scenarios

Conducting ground motion simulations requires several parameters. These parameters can be divided into three main groups: regional, fault rupture and finite fault parameters, and will be described in this order. Each fault is described separately and fault specific parameters are explained for each scenario. The finite fault model for each scenario is described with a sketch where the geometrical representation of the fault and the asperities are shown. There is also a table for each scenario earthquake summarizing the parameters used in the ground motion simulations. In addition there is also a short description of the databases and the corresponding spreadsheets developed or improved during the thesis work.

There is in this chapter referred to various appendices. Appendix C gives an overview on the calculations done in order to define grid points on the fault planes of the earthquake scenarios. Appendix D contains a list of normal fault events related to extensional regimes. Appendix E is a description of the program package used in order to conduct the ground motion simulations. Appendix F is a full database of all the input parameters needed for each program used in the ground motion simulations. There is also referred to the enclosed CD, which contains databases compiled during the work with this thesis-

4.1 Regional parameters

Regional parameters are dependent on the geology in the area for which the ground motion simulations are done. Of geological parameters a velocity model and attenuation relations are needed in order to conduct the ground motion simulations for seismic waves.

4.1.1 Velocity model

The velocity model used in this study originates from a previous study (Horasan et al., 2002). Horasan et al. (2002) determined the crustal structure by computing waveforms for the April 21, 2000 Denizli (Honaz) and July 9, 1998 İzmir (Doğanbey) earthquakes in the Aegean. The waveforms are synthesized by using the discrete wave number technique (Bouchon, 1981). Different layering of the area has been used in order to obtain synthetic seismograms comparable with the observed ones. The determined crustal and upper mantle structure of the İzmir/Aegean region showed a midcrustal low-velocity zone in the area and the crust is found to be 33 km thick. This is comparable with other studies (Saunders et al., 1998). The mid-crustal low-velocity zone is related to a warm crust due to the volcanic activity in the area arising because of the Hellenic subduction zone. The velocity model used in the ground motion simulations is given in table 4.1.

Table 4.1: Crust and upper mantle model for the Aegean Region determined from the 21 April 2000 Denizli (Honaz) and 9 July 1998 İzmir (Doğanbey) Earthquakes (Horasan et al., 2002).

Thickness (km)	V_p (km/sec)	V_s (km/sec)	Density (g/cm ³)	Q_p	Q_s
02	4.50	2.60	2.00	100	80
08	5.80	3.35	2.50	200	100
05	5.50	3.20	2.35	190	95
18	6.10	3.87	2.80	350	175
	7.85	4.53	3.10	1000	500

This velocity model, by Horasan et al. (2002), is adopted in the present work including the density and the Q-values, which are used in the ground motion simulations for the low frequencies.

4.1.2 Attenuation relations

In the case of west and northwestern Turkey several estimates of the regional attenuation have been performed. These studies are made for different attenuation relations and Q-values as Q_p , Q_s , Q_c , Q_0 and Q_{Lg} all based on different datasets (Akinci et al., 1995; Akinci et al., 2004; Akinci et al., 1994; Bindi et al., 2006a; Bindi et al., 2006b; Cong and Mitchell, 1998; Zor et al., 2007). In the case where Q_0 were estimated, the resulting values lie between 150-300 for the Turkish and Iranian Plateaus, with the lowest values in western Anatolia due to the high heat flow in the

crust and upper mantle (Cong and Mitchell, 1998). In the study conducted by Zor et al. (2007), the Q_0 values were found to be between 70-100 in the eastern Anatolian plateau and slightly higher (60-150) in the western Turkey around the Mendere Massif. For one of the estimates in the North Anatolia Fault Zone the Q_P attenuation mean value is found to be 25-60 in a distance range of 5-90 km (Akinici et al., 2004).

From the aftershocks following the 1999 Izmit earthquake frequency-dependent attenuation relations for both P and S waves have been determined in the frequency range of 1-10 Hz and for distances 10-140 km and the quality factors can be approximated to:

$$\begin{aligned} Q_S(f) &= 17 \cdot f^{0.80}, \text{ for } 1 \leq f \leq 10 \text{ Hz} \\ Q_P(f) &= 56 \cdot f^{0.25}, \text{ for } 2.5 \leq f \leq 10 \text{ Hz} \end{aligned} \quad \text{Eq. 4.1}$$

(Bindi et al., 2006a).

In western Anatolia, studies of Q_c and Q_{Lg} have been conducted. Q_c depends on the lapse time and there is given examples for attenuation relations of lapse times of 30 s and 190 s in table 4.2. It is concluded that the frequencies in this study are practically constant (Akinici et al., 1994).

Table 4.2: Frequency dependence of Q_c for different lapse times for western Anatolia (Akinici et al., 1994).

Lapse time	Frequency dependence of Q_c
30 s	$Q_c(f) = 50.7 \cdot f^{1.01}$
190 s	$Q_c(f) = 183.2 \cdot f^{0.76}$

The latest attenuation relation is based on Lg surface-waves, (Akinici et al., 1995). The frequency dependence in the crust is determined for a frequency range of 1.5-10.0 Hz with a geometrical spreading coefficient in the range of 0.6-0.9. The obtained relation is given in equation 4.2:

$$Q_{Lg}(f) = 82.0 \cdot f^{1.0}, \text{ for } 1.5\text{-}10\text{-Hz} \quad \text{Eq. 4.2}$$

This result is found by using the coda normalization method and thereby eliminate the source and site effects from the observed spectra of the Lg waves (Akinici et al., 1995).

In the ground motion simulation two attenuation models are needed; one for the low frequency and another one for the high frequency results. For the low frequency part of the modeling the attenuation values associated with the chosen velocity model (Horasan et al., 2002) are used, see table 4.1. The advantage of these is that a variation of the attenuation with depth has been taken into account in contrast to the results of Cong and Mitchell (1998) and Akinçi et al. (2004).

In the case of the high frequency attenuation a frequency dependent attenuation is needed in the ground motion simulation and three studies are available to choose from. The coda attenuation relation is an average of both high and low frequencies and will therefore take low-frequency attenuation into account. Since the ground motion simulations differ between the high and low frequency calculations, this relation is not used. The relations based on Q_P , Q_S and Q_{Lg} all cover the high frequency range in the study, and they could therefore all be used. However in this study the seismic hazard is obtained by setting up worst-case scenarios. Since the Lg waves give larger amplitudes than the S waves on the horizontal components of a seismogram, which indicates larger ground motions, the frequency dependent relation of Q_{Lg} (Akinçi et al., 1995) given in equation 4.2 is used.

4.2 Fault rupture parameters

Rupture complexities are closely related to the heterogeneities along the fault surface, and therefore the location of asperities. Fault rupture parameters are dependent on the rupture complexities and rupture dynamics. Rupture velocity and rise time are found to be two parameters, which vary with fault mechanism. Stress drop is also a parameter that is dependent on the fault mechanism and this parameter will therefore also be described in the following.

4.2.1 Rupture velocity

The size of the rupture velocity is roughly dependent on the earthquake mechanism. Rupture velocities seem to be larger for strike-slip faults than for normal faults. The

rupture velocity has a significant impact on the size of the simulated ground motions in the near fault area (Sørensen et al., in press).

In the case of the normal faults, previous studies of the rupture velocities for the 1999 Athens and Oaxaca and the 1983 Borah Peak events yield values of 2.1 km/s, 3.0 km/s and 2.9 km/s respectively (Hernandez et al., 2001; Mendoza and Hartzell, 1988; Sargeant et al., 2002). The average of these three studies yields 2.67 km/s.

Other studies use a rupture velocity corresponding to 0.7-0.8 of the shear wave velocity at the depth of the hypocenter (Dalguer et al., 2004; Hutchings et al., 1998; Stein and Wysession, 2003). In this study, the depth of the hypocenters for the earthquake scenarios on normal faults is in the range of 9.43-11.09 km. This corresponds to shear wave velocities in the chosen velocity model of 3.35 and 3.20 km/s, respectively. An average of these two values yields a shear wave velocity of 3.28 km/s and with a rupture velocity of 0.75 percent of the shear wave velocity; this yields a rupture velocity of 2.46 km/s. Both methods used to determine the rupture velocities give values around 2.5 km/s, and this value has therefore been adopted with a variability of ± 0.5 km/s for all the earthquake scenarios on normal faults (scenarios 1A-C IF and 5A-C MF). This value is also in agreement with the study conducted by Somerville et al. (1999).

In the case of the earthquake scenarios on strike-slip faults, the 2000 Tottori, 1999 Izmit, 1999 Düzce, 1995 Kobe and 1992 Landers events have been considered and they have rupture velocities of 2.5-3.5 km/s. The high velocity of 3.5 km/s occurred for the 1999 Izmit earthquake, and is a super-shear velocity. It is not assumed that this velocity will be reached at the relatively short fault lengths in this study. In the case of the ground motion simulations for the future Istanbul event a rupture velocity of 3 km/s was used (Pulido et al., 2004). This value is also adopted in this study, with a variability of ± 0.5 km/s, which is the average of the values obtained for the five events considered above.

4.2.2 Rise time

The rise time has a significant influence in the simulated ground motions, and a small variation in rise time can result in large variations in the simulated ground motions, (Sørensen et al., in press).

Concerning rupture velocity the rise time is also roughly dependent on the fault mechanism. This is clearly seen in various fault rupture models, (Mai, 2007). Thrust faults are in general found to have the highest rise times. There is, however, not given many examples of normal faulting events in the database of finite-source rupture models (Mai, 2007) ($M=6.77$, 1983 Borah Peak, Idaho and $M=7.25$, 1999 Oaxaca, Mexico events are the only ones), so a direct comparison between rise times for strike-slip events and normal fault events is not possible. However, rise time seems to be larger for strike-slip faults than for normal faults as it is the case for rupture velocity.

In this study ground motion simulations were conducted for both normal and for strike-slip faults. Among events in recent time and nearby regions the September 7, 1999 Athens event and the 1981 Gulf of Corinth earthquake sequence are available when adopting a rise time for the normal faulting events in this study (scenarios 1A-C IF and 5A-C MF). In the case of the earthquake sequence in the Gulf of Corinth extraordinary long rise times were obtained, both for the main shock (4 s) and the following two aftershocks (2.5 s) (Kim et al., 1984). For the Athens earthquake the rise time is determined by both numerical and empirical modeling and these yields very short values of 0.1-0.3 s (Tselentis and Zahradnik, 2000). The rise times found for the 1983 Borah Peak and the 1999 Oaxaca events are 0.6 s and 1.86 s respectively (Hernandez et al., 2001; Mendoza and Hartzell, 1988). The rise time used for the normal faults in this study is 1 ± 0.4 s. This is based on a rough mean value of the different rise times from the events mentioned above.

In case of the strike-slip events in this study (scenario 2-4) the rise time is selected to be larger than for the normal faults. The reason for this is the large amount of data found, for strike-slip faults where well known events such as the 2000 Tottori, 1999 Izmit, 1999 Düzce, 1995 Kobe and 1992 Landers events all have rise times of 2.7-3.5

s, (Mai, 2007). In a study conducted by Pulido et al. (2004) of a scenario earthquake in the Marmara Sea, the rise time adopted was 3 s, which is a rough average value for the above-mentioned different events. For this reason the rise time for the earthquake scenarios occurring on strike-slip faults in this study has been selected to be 3 ± 0.5 s.

4.2.3 Stress drop

Variation of the stress drop for different earthquakes is in general poorly understood and implies significant uncertainty. However, this parameter is in the same time also the most important parameter in the dynamics of faulting process that can be determined seismically (Lay and Wallace, 1995). An example of this uncertainty is illustrated by two different studies made on the September 7, 1999 Athens earthquake, where Tselentis and Zahradnik (2000) estimated a stress drop of 2.7 MPa (27 bars) and Sargeant et al. (2002) estimated the stress drop to be 0.54 MPa (5.4 bars).

Becker and Abrahamson (1998) have found median values using Boore-Joyner amplifications (Boore and Joyner, 1997) of 47 and 52 bars for normal and strike-slip faulting respectively, while the values are only a minor different: 45 and 59 bars when Silva's transfer functions (Becker and Abrahamson, 1998) are used. Several formulae for stress drop exist; some of these are given in table 4.3.

Table 4.3: Stress drop relations from different authors. In the relation from Abe (1975), β is the shear-wave velocity, ρ is the density, D/T is the slip-velocity. In the relation from Kanamori and Anderson (1975) have C as a fault geometry constant, μ is the rigidity of the crust and S/L is the representative strain change. In the relations by Stein and Wyssession (2003) M_0 is the seismic moment, R is the radius of the circular fault, w is the width of the fault and L is the length of the fault.

Source	Stress drop
Abe (1975)	$\Delta\sigma = \beta \cdot \rho \cdot (D/T)$
Kanamori and Anderson (1975)	$\Delta\sigma = C \cdot \mu \cdot (S/L)$
Stein and Wyssession (2003) (circular fault)	$\Delta\sigma = \frac{7}{16} \cdot \frac{M_0}{R^3}$
Stein and Wyssession (2003) (rectangular strike-slip fault)	$\Delta\sigma = \frac{2}{\pi} \cdot \frac{M_0}{(w^2 \cdot L)}$
Stein and Wyssession (2003) (rectangular dip-slip fault)	$\Delta\sigma = \frac{8}{3\pi} \cdot \frac{M_0}{(w^2 \cdot L)}$

The three relations for the stress drop by Stein and Wyssession (2003) require fault dimension, which can be difficult to obtain.

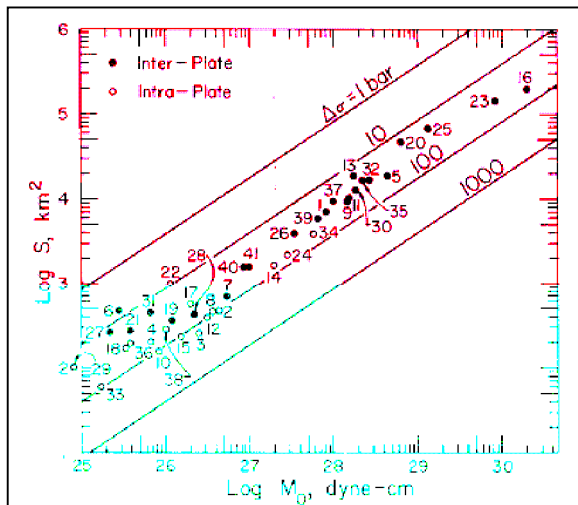


Figure 4.1: Relation between S (fault surface area) and M_0 (seismic moment). The straight lines give the relations for circular cracks with constant $\Delta\sigma$ (stress drop) (Kanamori and Anderson, 1975).

Studies made by Stein and Wysession (2003) and Lay and Wallace (1995) both refer to Kanamori and Anderson, (1975), which have plotted both interplate and intraplate earthquakes in terms of the logarithmic fault area and logarithmic seismic moment (lines of constant stress drop is given as solid lines), see figure 4.1.

From figure 4.1 it is seen that stress drop for all earthquakes is between 10-100 bars. The stress drop for intraplate earthquakes is found to be higher (around 100 bars) than the stress drop for the interplate earthquakes (around 30 bars). This is consistent with the longer recurrence interval for the intraplate earthquakes, resulting in a relatively larger energy release compared to the fault area. This difference is easily illustrated by stress drop from two normal fault earthquakes: the interplate 1983 Borah Peak and the intraplate 1999 Oaxaca which had stress drops of 17 bars and 90 bars respectively (Mai, 2007).

In a stress drop analysis of world wide shallow earthquakes in the period 1900-1998 it is found that stress drop for normal faulting events is between 0.6-100 bars with a mean value of 21 bars (Bayrak and Yilmazturk, 1999). In the same study, the stress drop average for strike-slip faults is found to be between 2 and 199 bars, and the stress drop is thereby higher for strike-slip events than for normal fault events.

The study area is not located at a plate boundary, however due to the high deformation resulting from the westward migration of the Anatolian plate and the Hellenic subduction zone it would also be misleading to define the area as an intraplate area and the stress drop for the events should therefore be in the lower end. With regard to the normal fault earthquakes in this study there were chosen an average stress drop of 30 bars. The value is consistent with the study of the September 7, 1999 Athens earthquake conducted by Tselentis and Zahradnik (2000). A relatively high value for the stress drop has been selected since the final aim of this study is a

hazard analysis where the simulated ground motions are calculated for a realistic worst-case scenario.

In the case of the earthquake scenarios for the strike-slip events in this study the equation for obtaining stress drop used in the study by Pulido et al. (2004) is adopted. Here, the ratio between the total asperity area and the total fault area is taken from Somerville et al. (1999) to be 0.22, which when inserted in the relation for the total seismic moment takes the form:

$$M_0 = \frac{16}{7} \cdot \Delta\sigma_{ave} \cdot r \cdot R^2 \cdot \left(\frac{24}{7 \cdot \pi} \right)^2 \quad Eq. 4.3$$

(Das and Kostrov, 1986). Substituting the ratio into equation 4.3 and solving for $\Delta\sigma$ gives:

$$\Delta\sigma = \frac{M_0}{0.229 \cdot S^{3/2}} \quad Eq. 4.4$$

The average stress drop for, both normal and strike-slip faults, are divided out on the background (low-slip) and the asperity (high-slip). This is done with the area ratio of the background and the asperity:

$$\Delta\sigma_{ave} = 0.78 \cdot \Delta\sigma_{bg} + 0.22 \cdot \Delta\sigma_{asp} \quad Eq. 4.5$$

The ratio of stress drops between the background and asperity is chosen to be 0.05 (Dalguer et al., 2004).

An example of the stress drop calculations is given for earthquake scenario 2 GF, Gülbahçe fault, which is 45 km long and 15 km wide and has a seismic moment of 3.22E19 Nm, (see section 4.3.3 for calculating earthquake magnitudes). The average stress drop is found to be:

$$\Delta\sigma_{ave} = \frac{3.22 \cdot 10^{19} \text{ N} \cdot \text{m}}{0.229 \cdot (45 \cdot 10^3 \text{ m} \cdot 15 \cdot 10^3 \text{ m})} = 8.018 \cdot 10^6 \text{ N/m}^2$$

$$\Delta\sigma_{ave} = \underline{\underline{80.18 \text{ bar}}}$$

With a stress drop ratio of 0.05, the asperity and background stress drop is found to be:

$$\Delta\sigma_{asp} = \frac{\Delta\sigma_{ave}}{0.78 \cdot 0.05 + 0.22} \Rightarrow$$

$$\Delta\sigma_{asp} = \frac{80.18 \text{ bars}}{0.78 \cdot 0.05 + 0.22} = \underline{\underline{309.57bars}}$$

$$\Delta\sigma_{bg} = 0.05 \cdot \Delta\sigma_{asp} \Rightarrow$$

$$\Delta\sigma_{bg} = 0.05 \cdot 309.57 \text{ bars} = \underline{\underline{15.48bars}}$$

4.3 Finite fault models

For each fault where a scenario earthquake is prepared, the coordinates for defining the fault were adopted from Emre et al. (2005). The different scenario earthquakes presented in this work are placed at already mapped faults, as it is shown in the work of MTA (Emre et al., 2005b). Geometry of the faults is based on the MTA-study, (Emre et al., 2005b) combined with a rough morphology analysis. The length of the different faults has been based on a combination of the length on the available fault maps, and on length that can agree with a subfault length of either 2.5 km or 3 km. Furthermore; the faults have been determined to consist of linear segments, which are not according to reality, but a good approximation.

In the following scenarios the asperities are typically placed in the center on the fault plane, since there is no further information of slip distribution from earlier events. In a single case, scenario 2GF, the Gülbahçe fault; the two asperities are however placed attached to the mid-segment, at a bend, based on the morphology information given by *Google Earth*. The total size of the asperities is in previous studies found to be about 22% of the total ruptured area (Somerville et al., 1999).

In Somerville et al. (1999) the sizes of the asperities on the fault plane were compared to each other and it was found that the largest asperity takes up 17.5 % of the entire fault plane. This information is, however, not used in the geometry of the earthquake scenarios in this study. In most of the scenario earthquakes of this study there is only one asperity per fault, and in the cases of several asperities an asperity size corresponding to 22% of the segment area has been adopted. This choice of the size of the individual asperities is consistent with previous studies where earthquake ground motion simulations have been conducted (Pulido and Kubo, 2004; Pulido et al., 2004; Sørensen et al., 2007). The poor knowledge of the geomorphology in the study area

also sets limits to estimates of areas of high slip distribution on the fault planes, and the geometry of the asperities on the fault planes is therefore made as simple as possible.

4.3.1 Fault plane geometry

In nature faults have complicated geometry, however, in this study - and also inferred in other modeling studies - earthquake scenarios are based on rectangular faults. The length of the fault is defined along strike and the width of the fault is defined along the dip orientation.

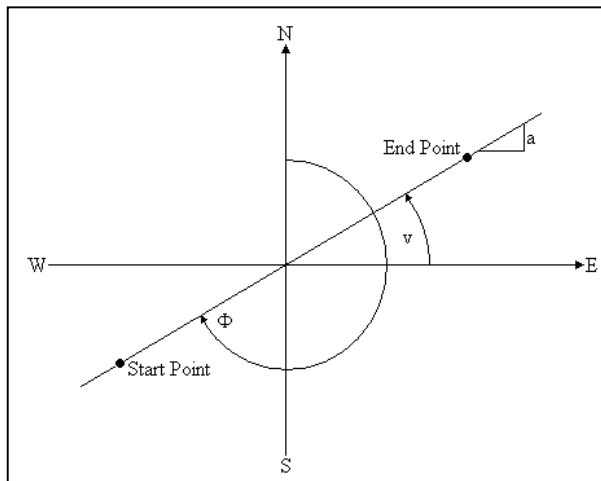


Figure 4.2: Geometry of the setup when defining a fault line from two end points. The slope is described by “a” and the strike with respect to the north is given by “Φ”. Which angle to use (smaller or larger than 180 °, is determined by using the right hand rule.

Even though the real faults are more complex in their geometry, e.g. the faults curve and are therefore three-dimensional and the rupture history is complicated, it is possible to model earthquakes by means of a two-dimensional fault plane and superposition of several simple events.

Once the end-points of a fault have been determined, it is by simple vector calculation possible to calculate the strike of the fault with respect to north. A full example of how to calculate all the different parameters and thereby points on the fault plane needed for input in the ground motion simulation is given for the case of scenario 1A WIF, Western İzmir Fault below.

The strike is found by drawing a line through the two end-point and finding the slope, a , of this line, see figure 4.2.

$$a = \frac{E_{lat} - S_{lat}}{E_{long} - S_{long}} \quad \text{Eq. 4.6}$$

Here a is related to the angle of the east-west/horizontal line by:

$$a = \tan(v) \Leftrightarrow v = \arctan(a) \quad \text{Eq. 4.7}$$

The direction of strike Φ is defined with the **right hand rule**: *place the right hand with the fingers pointing in the direction of the dip and the inside of the hand towards the fault plane; the strike is measured from north to the fault line to the end where the thumb is pointing*. When the orientation of the fault is found, the strike is calculated by subtracting v from 90° and if the orientation requires it, by adding 180° .

Example of calculations

To set up the geometry of a scenario earthquake strike, dip and reference points on the background fault plane and on the asperity are needed as well as the hypocenter of the event. Calculating the different parameters and points needed from the two end-points of the fault are formalized in a spreadsheet calculation routine. A print out of this sheet and explanations to it is given in appendix C.

The following is a description of how points on the fault plane for scenario 1A WIF Western İzmir Fault, have been calculated. Since the calculations for finding the points are similar, only one example of the calculations is given, using the data shown in table 4.4, for the point in the background asperity.

Table 4.4: Start and end-point for the Western İzmir Fault used in scenario 1A WIF. The dip of the fault and the scale in the longitude and latitude direction in the study area are also given. These parameters are used to calculate points on the fault plane needed in order to make ground motion simulations.

Start longitude	26.8799°E
Start latitude	38.3743°N
End longitude	27.0845°E
End latitude	38.3983°N
Dip	60°
Scale longitude	87.14 km/deg
Scale latitude	111.2 km/deg

The slope of the line between the two end-points of the fault is found from equation 4.6:

$$a = \frac{38.3983 - 38.3743}{27.0845 - 26.8799} = 0.12$$

This gives an angle from the horizontal of:

$$\nu = \arctan(0.1173) = 6.69^\circ$$

Since the fault is dipping towards the northwest using the *right hand rule*; the strike is larger than 180° , and the strike is therefore found as:

$$\Phi = 90^\circ - \nu + 180^\circ = \underline{\underline{263.31^\circ}}$$

The point that needs to be found in the plane of the background asperity is placed 1.5 km along strike, $|s|$, and 1.5 km along dip, $|c|$, from the start-point of the fault. Since the fault plane is dipping with 60° , the horizontal distance along the dip is found by:

$$|p| = \cos(\delta) \cdot |c| \Rightarrow \quad \text{Eq. 4.8}$$

$$|p| = \cos(60^\circ) \cdot 1.5 \text{ km} = 0.75 \text{ km}$$

By Pythagoras a vector can be divided into two components: one in the east-west direction, dx , and another in the north-south direction, dy :

$$|s| = \sqrt{dx^2 + dy^2} \quad \text{Eq. 4.9}$$

The component dy can be found from the slope of the fault line, a , as described in figure 4.2:

$$dy = a \cdot dx \quad \text{Eq. 4.10}$$

Inserting equation 4.10 into equation 4.9 and solving for dx gives:

$$|s| = \sqrt{dx^2 + (a \cdot dx)^2} \Leftrightarrow$$

$$dx = \sqrt{\frac{|s|^2}{(1 + a^2)}} \quad \text{Eq. 4.11}$$

Finding the point on the background asperity is done in two steps. First by moving along the fault plane in the strike direction and afterwards moving along the dip direction, using an orientation perpendicular to the strike of the fault ($=173.31^\circ\text{N}$). The contributions, dx and dy , are added after each calculation.

The components $dx_{_S}$ and $dy_{_S}$ of the vector $|s|$ are the contributions in the east west and north south directions respectively that should be added to the reference point when moving 1.5 km along the strike from the start-point given in table 4.4. Using equation 4.11 $dx_{_S}$ can be found, and afterwards equation 4.10 is used to find $dy_{_S}$:

$$dx_{-s} = \sqrt{\frac{|1.5 \text{ km}|^2}{(1 + 0.12^2)}} = \underline{1.49 \text{ km}}$$

$$dy_{-s} = 0.12 \cdot 1.49 \text{ km} = \underline{0.18 \text{ km}}$$

Before adding these coordinate changes to the starting point, they have to be calculated into contributions in degrees, using the scale parameters for longitude and latitude in the area given in table 4.4. This gives coordinates for the point located 1.5 km from the start-point of the fault following the strike direction:

$$dx_{-s} = \frac{1.49 \text{ km}}{87.14 \text{ km/deg}} = \underline{0.02^\circ}$$

$$dy_{-s} = \frac{0.18 \text{ km}}{111.2 \text{ km/deg}} = \underline{0.002^\circ}$$

$$x_{_Strike} = x_{_start} + dx_{-s} \Rightarrow$$

$$x_{_Strike} = 26.88^\circ + 0.02^\circ = \underline{26.90^\circ}$$

$$y_{_Strike} = y_{_start} + dy_{-s} \Rightarrow$$

$$y_{_Strike} = 38.374^\circ + 0.002^\circ = \underline{38.376^\circ}$$

Next step is to calculate the coordinate change when moving 1.5 km along dip, dx_{-D} and dy_{-D} , which corresponds to 0.75 km along the dip on the horizontal plane. The procedure is the same as above, except that the slope along which the coordinates are changed is perpendicular to a .

$$a_{\perp} = b = \frac{-1}{a} \Rightarrow \quad \text{Eq. 4.12}$$

$$b = \frac{-1}{0.12} = -8.33$$

Using equation 4.11 and 4.10 gives:

$$dx_{-D} = \sqrt{\frac{|0.75 \text{ km}|^2}{(1 + (-8.33)^2)}} = \underline{0.09 \text{ km}}$$

$$dy_{-D} = |-8.33| \cdot 0.09 \text{ km} = \underline{0.74 \text{ km}}$$

These contributions are calculated into contributions in degrees and then added to the coordinates $x_{_Strike}$ and $y_{_Strike}$ and give the longitude and latitude coordinates for the point on the background asperity located 1.5 km from the start-point of the fault

following the strike for 1.5 km and then the dip for 1.5 km (0.75 km horizontal distance):

$$dx_{-D} = \frac{0.09 \text{ km}}{87.14 \text{ km/deg}} = \underline{0.001^\circ}$$

$$dy_{-D} = \frac{0.74 \text{ km}}{111.2 \text{ km/deg}} = \underline{0.01^\circ}$$

$$x_{background} = x_{Strike} - dx_{-D} \Rightarrow$$

$$x_{background} = 26.90^\circ - 0.001^\circ = \underline{\underline{26.89^\circ}}$$

$$y_{background} = y_{Strike} + dx_{-D} \Rightarrow$$

$$y_{background} = 38.38^\circ + 0.01^\circ = \underline{\underline{38.39^\circ}}$$

The depth $|d|$ of this point is found by the sinus relation given in equation 4.13:

$$|d| = \sin(\delta) \cdot |c| \quad \text{Eq. 4.13}$$

Since in all the earthquake scenarios fault planes are placed 2 km underneath the surface, this has to be added resulting in a depth of the background asperity point of:

$$|d| = \sin(60^\circ) \cdot 1.5 \text{ km} = 1.30 \text{ km}$$

$$|D| = |d| + 2 \text{ km} = \underline{\underline{3.30 \text{ km}}}$$

Whether the contributions in the east west (x) and north south (y) directions are added or subtracted from the reference point depends on the fault geometry, and it is therefore not consistent among the earthquake scenarios in this study. It is described in more detail in the appendix C.

4.3.2 Rupture initiation point

In a previous study the hypocenter location and regions of large slip have been correlated and it was found that for strike-slip and dip-slip earthquakes the rupture nucleates in the deeper sections of the fault. Furthermore it was found that the rupture initiation point is not randomly located at fault planes, but that the rupture nucleates within or close to regions of large slip, (Mai et al., 2005).

Based on the study of Mai et al. (2005) the rupture initiation points for the ground motion simulations conducted in this study are placed in one of the lower corners on the edge between the asperity (high-slip area) and the background (low-slip) area of the fault. Since this study consists of very simple earthquake scenarios the slip distribution across the asperity is assumed identical. Given that this work is a deterministic hazard assessment, the hypocenter has been placed to give a worst-case scenario for the city of İzmir. In order to obtain this hypocenters are in the different scenarios placed so the directivity occurring due to the propagation of the rupture along the fault points in the direction of the city center of İzmir. The simplest example is found for the scenario made for the western İzmir fault (scenario 1A WIF and 1B EIF), a fault starting to the west of the city and ending in the east, all placed underneath the city. To get the highest ground motions in the city center of İzmir the hypocenter is placed in the western lower corner of the asperity, and thereby giving rupture propagation towards east and the city center.

4.3.3 Magnitude

To be sure not to overestimate the magnitudes of the earthquake scenarios, a list over large normal fault earthquakes related to extensional regimes has been drawn up. This list is given in appendix D. The largest normal fault events are found to have a moment magnitude of up to magnitude 7.6 for the August 18, 1959 Hebgen Lake, USA event. In the surroundings of the study area in western Turkey no normal fault event larger than 7.1, as the February 22, 1653 Menderes and the March 28, 1970 Gediz events have been observed and it is therefore not reasonable to set up an earthquake scenario with a larger magnitude.

Several empirical relations based on different datasets reaching from worldwide to regional have been made (Ambraseys and Jackson, 1998; Anderson et al., 1996; Somerville et al., 1999; Wells and Coppersmith, 1994). In the work carried out by Somerville et al. (1999) most events used are from the US except the 1995 Kobe, Japan and the 1978 Tabas, Iran events. The obtained relations for the different parameters are not divided into rupture types as it is done in the work made by Wells

and Coppersmith (1994). Also there is given no relation between magnitude and fault length since the faulting area is used instead.

In the work of Wells and Coppersmith (1994) the dataset used to develop the relations is much larger than the one used by Somerville et al. (1999) (244 events compared to 15 events in the database from Somerville et al. (1999)), and the dataset is world wide with 18 events in Turkey, where one has occurred in the study area around İzmir. However, the work only covers geometric relations as magnitude versus fault length, down dip rupture width, rupture area, displacement etc.. Information about asperities, rise time, slip time etc., which Somerville et al. (1999) works with, is therefore lacking.

In Ambraseys and Jackson's work (1998) the data is from the eastern Mediterranean region, the dataset consisting of 150 events, of which 7 events are located in the defined area of interest. The empirical relations found in this study are concerning magnitude versus fault length. The geometrical relations for magnitude versus fault length/down dip rupture width/rupture area/displacement are very similar in all three studies.

Since the relations obtained by Somerville et al. (1999) are not based on any data from the study area, information from this work has only been used in the cases where no other information was available, e.g. for asperity size. In the case of the work done by Ambraseys and Jackson (1998) there is no distinction between the fault types when the empirical relations are obtained. If the relation for magnitude versus fault length is compared with the one obtained in the general case by Wells and Coppersmith (1994), they are found to be similar, even though the results are based on two different datasets.

In order to test the empirical relations obtained from Wells and Coppersmith (1994) and Somerville et al. (1999) respectively, the September 20, 1899 Menders Massif earthquake was used. This normal fault event occurred within the study area with a hypocenter of 37.9°N and 28.8°E, and is estimated to have a surface-wave magnitude, M_s , of 6.9 (Ambraseys and Jackson, 1998). The maximum displacement of this event has been estimated to be of 1.5-2 m (Altunel, 1998). Using the relations from Wells

and Coppersmith (1994) and Somerville et al. (1999), where the moment magnitude is calculated from displacement, equation 4.14 and 4.15 respectively and the values of 1.5 m and 2 m displacement gives the corresponding magnitudes shown in table 4.5.

$$M = 6.61 + 0.71 \cdot \log(MD) \quad \text{Eq.4.14}$$

$$M = \frac{1}{3} \sqrt[3]{\frac{1}{1.56 \cdot 10^{-7}} \cdot D} \quad \text{Eq. 4.15}$$

It is found that the moment magnitude is smaller and closer to the estimated magnitude from Ambraseys and Jackson when the empirical relation from Wells and Coppersmith is used. It is reasonable to compare surface-wave magnitude and moment magnitude in the interval $M=6-7.5$ (Heaton et al., 1986).

Table 4.5: Moment magnitudes found from the empirical relations obtained from Wells and Coppersmith (1994) and Somerville et al. (1999) using displacements of 1.5 m and 2 m respectively.

Relation:	1.5 m slip	2.0 m slip
Wells and Coppersmith (1994)	6.73	6.82
Somerville et al. (1999)	7.23	7.48

When the moment magnitude for a scenario earthquake on a fault is to be determined, the empirical relations found in the study by Wells and Coppersmith are used. The reason is that the dataset for this study consists partly of events from Turkey and the relations found by Somerville et al. (1999) seem to overestimate the moment magnitudes in this area. In the calculations of the magnitudes both the relations for surface rupture length and for fault area have been used. The fault type has also been taken into account, and the adopted relations are given in table 4.6.

Table 4.6: Empirical relations of Surface Rupture Length, SRL, and Rupture Area, RA, to Moment Magnitude, M used in this study, (Wells and Coppersmith, 1994).

	Fault type:	
	Normal fault	Strike-slip fault
Surface Rupture Length	$M = 4.86 + 1.31 \cdot \log(SRL)$	$M = 5.16 + 1.12 \cdot \log(SRL)$
Rupture Area	$M = 3.93 + 1.02 \cdot \log(RA)$	$M = 3.98 + 1.02 \cdot \log(RA)$

When the moment magnitudes are obtained, they are converted into seismic moment; the relation is given in equation 4.16,

$$M_w = \frac{2}{3} \cdot \left(\log\left(\frac{M_o}{N \cdot m}\right) - 9.1 \right) \Rightarrow M_o = 10^{\left(\frac{3}{2} \cdot M_w + 9.1\right)} N \cdot m \quad \text{Eq. 4.16}$$

(Hanks and Kanamori, 1979; Kanamori, 1977).

The two moment magnitudes, the average and the corresponding seismic moments are given for each scenario earthquake in table 4.7.

Table 4.7: Calculated values for the moment magnitude, M , by using Surface Rupture Length, SRL, and Rupture Area, RA. The average value of the two magnitudes is shown and the relation given in equation 4.16 calculates this into seismic moment, M_o , in Nm.

Fault	M_{SRL}	M_{RA}	$M_{average}$	M_o (Nm)
1A WIF	6.517	6.410	6.463	6.24E+18
1B EIF	6.606	6.478	6.542	8.18E+18
1C IF	6.986	6.785	6.886	2.69E+19
2 GF	7.012	6.866	6.939	3.22E+19
3 TF	6.942	6.803	6.872	2.56E+19
4 SF	6.674	6.559	6.617	1.06E+19
5A WMF	6.517	6.410	6.463	6.24E+18
5B IMF	6.412	6.329	6.371	4.53E+18
5C EMF	6.645	6.509	6.577	9.23E+18

Using relations for surface rupture length and rupture area gives small variations in the calculated moment magnitudes. As it is seen, there is no significant difference between the moment magnitudes found from either surface rupture length or rupture area. Surface rupture length may be better constrained than the rupture area, since this requires detailed knowledge of the fault in depth, but since the minor differences of 0.1-0.15 are within the uncertainties of these relations it was found reasonable to use an average of the two values. The good congruity of the two magnitude relations also tells us that the width of the faults used in this study is reasonable.

In the ground motion simulations the seismic moment is distributed on the faults in two sections; in the background and in the asperities, which is divided as 60/40 respectively. In the case where there are several asperities and segments, the seismic moment is divided according to the size of these by the following relations:

$$M_{0, asp1} + M_{0, asp2} = 0.4 \cdot M_0 \quad Eq. 4.17$$

$$\frac{M_{0, asp1}}{M_{0, asp2}} = \left(\frac{A_{asp1}}{A_{asp2}} \right)^{1.5} \quad Eq.4.18$$

The same equations are used concerning the background, although the total background seismic moment equals 60% of the total seismic moment. See more details on this in the manual for the program package, which is enclosed in appendix E.

4.4 Fault rupture scenarios

The Mineral Research and Exploration Institute, Ankara, Turkey, (MTA) has mapped the active faults in the area around İzmir (Emre et al., 2005b). In total 40 faults were mapped as active in the area, see figure 2.6.

In this thesis there is constructed earthquake scenarios on some of these faults and computed the corresponding ground motion. Since the aim is to compute the hazard in İzmir, there is selected a set of 5 faults, which are the most relevant, and closest to the city. These are shown in figure 4.3. Although on figure 2.6 a fault is shown crossing the northern part of the city of İzmir south of Spil Mountain, this fault is not considered since it is classified as a lineament (Emre et al., 2005b).

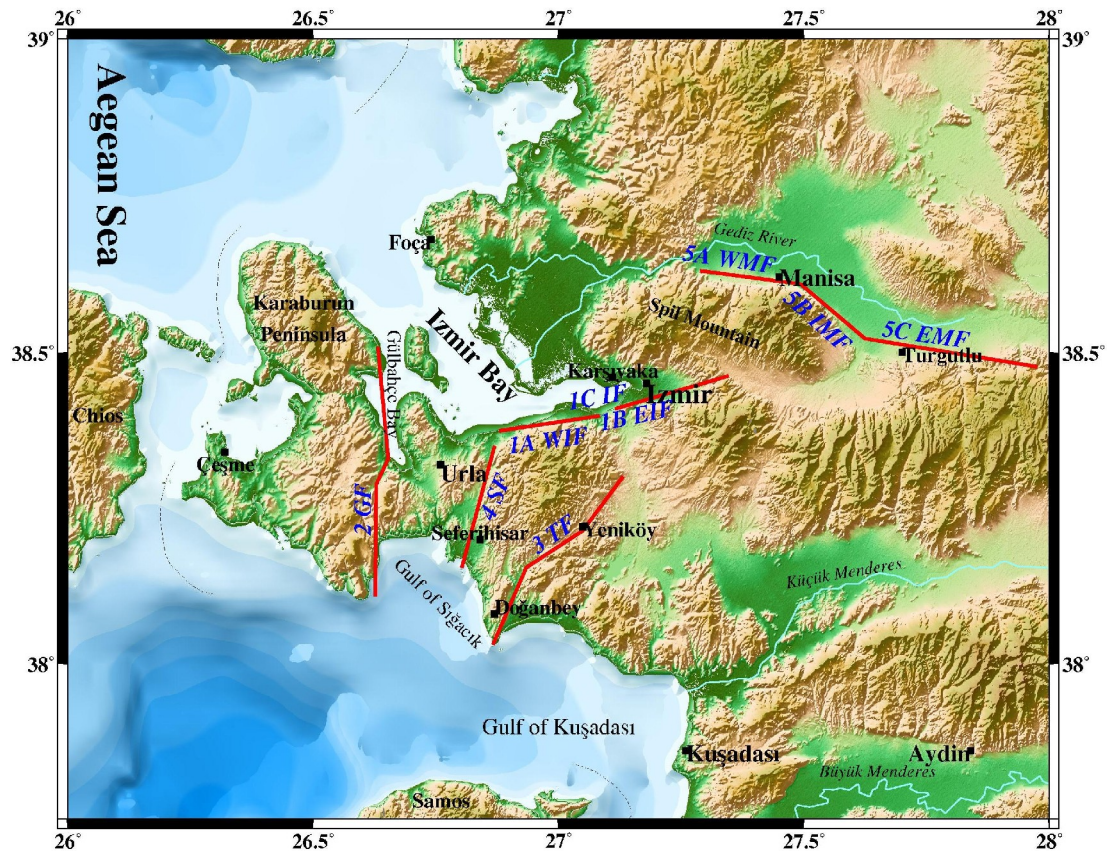


Figure 4.3: Map showing the simplified faults for which there have been conducted ground motion simulations for in this study. The code for the different scenarios is written in blue next to the respective faults. The scenario 1C IF is a combined scenario of fault 1A WIF and 1B EIF, with a step-over of 3 kilometers in the middle part of the fault

In the following a description of each fault rupture scenario is given. For each scenario a simple sketch is prepared to illustrate the coordinates defining the fault, the location of the fault asperities, the subfault size used and the rupture initiation point

(RIP). In the fault descriptions the focal mechanism for each scenario earthquake is also given.

4.4.1 İzmir fault

The metropolitan area of İzmir is situated above an active fault oriented east west parallel to the southern coast of the İzmir bay. Western and eastern segments are separated by a step-over of approximately 3 kilometers. The two segments are oriented in almost the same direction, although there is a slight deviation in strike of approximately 6° . In general the fault, although visible on the topography, does not show any clear outcrops due to partly dense urban development and partly because it enters offshore in the westernmost end.

Caused by the segmentation along the İzmir fault, three different earthquake rupture scenarios were set up for this fault; the western part, the eastern part and a combined rupture of both fault segments, with a 3 kilometer segment in between.

Although the strikes of the segments are slightly different, the dip and slip used for the segments are assumed to be the same. The dip of the fault is determined from the Global CMT catalog for the normal fault events in the area, with emphasis on the $M_w = 5.3$, June 16, 1979 earthquake, which occurred on the İzmir fault. The earthquake focal mechanisms with strikes corresponding to the strikes of the İzmir fault segments ($250^\circ - 270^\circ$), are found to have dips of 58° or 59° (Larson, 2006). The dip of the İzmir fault is determined to be 60° towards north in the study made by the MTA, (Emre et al., 2005b). From these results the dip of the segments of the İzmir fault is assumed to be 60° in the conducted ground motion simulations.

The slip angle on these fault segments has been determined based on the values from the Global CMT catalog, which gives values between -124° to -93° . The regional stress field and the rotation of Western Anatolia indicate a north-south extension, resulting in east-west oriented normal faults with opening in the western end. If this is the case, it implies that the rake of the fault must be between -135° and -90° , which indicates a slip of the hanging wall block towards northeast. The slip used for the

İzmir segments has been chosen to be -100° , since this gives a normal faulting event with a small strike-slip component, and the value is consistent with previous observations.

The İzmir fault is known to have ruptured both during historical and instrumental times. In July 10, 1688 the fault ruptured ($M_w = 6.8$) causing tremendous damage to the city of İzmir, (Ambraseys and Finkel, 1995). In the instrumental period an earthquake occurred at the İzmir fault in 1977 and 1979, the moment magnitude of this event was recorded to be 5.5 and 5.3 respectively (Emre et al., 2005b).

1A WIF, Western İzmir Fault segment

Scenario 1A WIF is the earthquake simulated on the westernmost part of the İzmir fault. A sketch of the fault plane is given in figure 4.4, where the size of the subfaults used in the simulation is shown.

Table 4.8 summarize the parameters used in the ground motion simulations from the earthquake scenario 1A WIF.

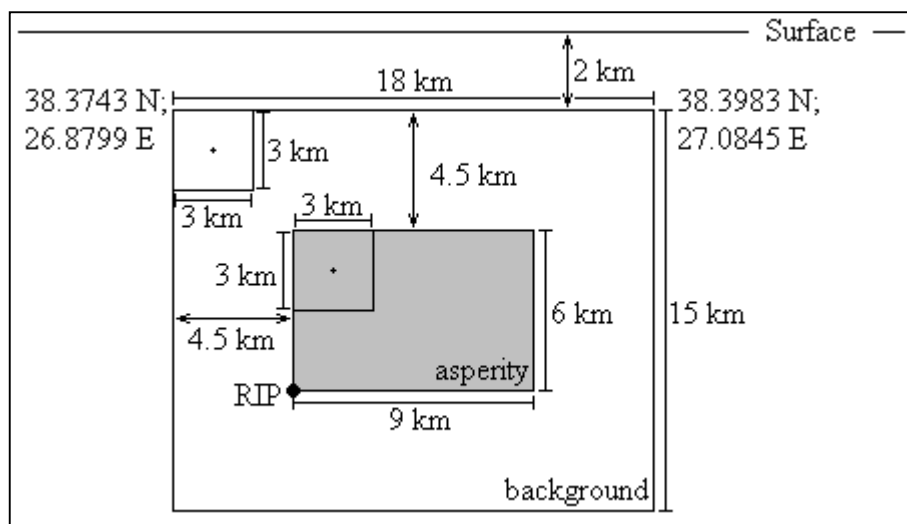


Figure 4.4: Sketch of the western segment of the İzmir fault, scenario 1A WIF. The coordinates for the start and end points are given. Rupture initiation point (RIP) is found in the lower most western part of the asperity.

The hypocenter of the earthquake scenario is placed in such a way that it produces a worst-case scenario with respect to ground motions in the center of İzmir. Therefore

the rupture initiation point (hypocenter) is placed in the western end of the fault in order to get a directivity effect towards the city.

Table 4.8: The source parameters used in the ground motion simulations for the scenario 1A WIF, Western İzmir fault. The fault plane solution is given as strike/dip/rake.

Moment magnitude, M_w	6.463
Seismic moment, M_0	6.24E+18 Nm
Fault plane solution	263.31°/60°/-100°
Hypocenter depth	11.09 km
Average stress drop	30 Bar
Asperity stress drop (high-slip)	115.83 Bar
Background stress drop (low-slip)	5.79 Bar
Rise time	1.0 ± 0.4 s
Rupture velocity	2.5 ± 0.5 s
f_{max}	10 Hz
Q	82 · f^{-1}

1B EIF, Eastern İzmir Fault segment

The eastern segment of the İzmir fault is 3 km longer than the western segment. This yields in a larger seismic moment for this earthquake scenario. Details of this event are given in figure 4.5 and table 4.9.

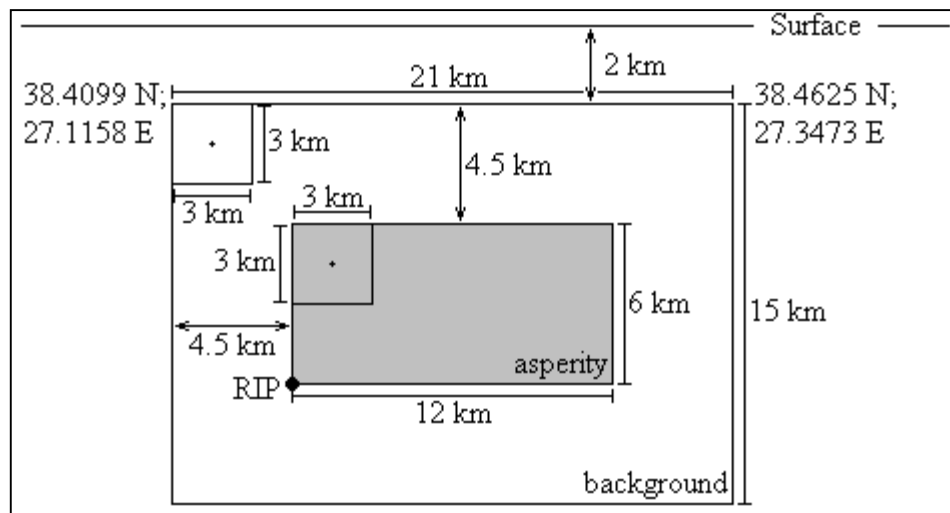


Figure 4.5: Sketch of the eastern segment of the İzmir fault, scenario 1B EIF. The coordinates for the start and end points are given. Rupture initiation point (RIP) is found in the lower most western part of the asperity.

Table 4.9: The source parameters used in the ground motion simulations for the scenario 1B EIF, Eastern İzmir fault. The fault plane solution is given as strike/dip/rake.

Moment magnitude, M_w	6.542
Seismic moment, M_0	8.18E+18 Nm
Fault plane solution	257.20°/60°/-100°
Hypocenter depth	11.09 km
Average stress drop	30 Bar
Asperity stress drop (high-slip)	115.83 Bar
Background stress drop (low-slip)	5.79 Bar

Rise time	1.0 ± 0.4 s
Rupture velocity	2.5 ± 0.5 s
f_{\max}	10 Hz
Q	$82 \cdot f^{-1}$

The rupture initiation point is, as in the case of the westernmost segment placed in the western end of the asperity to ensure rupture directivity towards east and the city center of İzmir.

1C IF, İzmir Fault

In a separate scenario the entire İzmir fault is defined including the two segments from scenario 1A WIF and 1B EIF combined from the westernmost point in scenario 1A WIF to the easternmost point in segment 1B EIF, with a small segment of 3 km in the middle, combining the two fault segments. A sketch of the fault plane is given in figure 4.6 and details on the used input parameters are given in table 4.10.

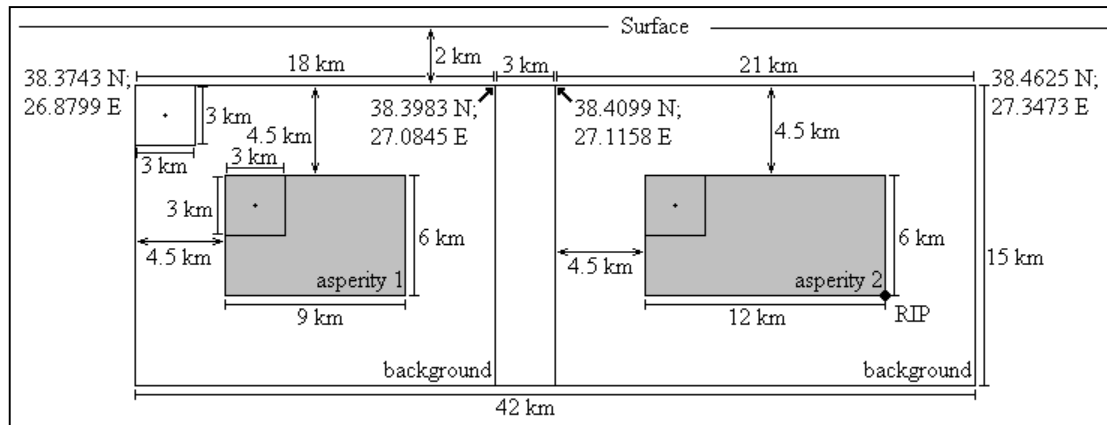


Figure 4.6: Sketch of the İzmir fault, scenario 1C IF. The coordinates for the start and end points are given. Rupture initiation point (RIP) is found in the lower most eastern part of asperity 2.

The rupture initiation point is placed in the eastern end of asperity to in order to obtain the ground motions in the city center of İzmir.

Table 4.10: The source parameters used in the ground motion simulations for the scenario 1C IF, İzmir fault. The scenario earthquake consists of two segments, a western and an eastern part; fault plane solutions are given for both segments. The fault plane solutions are given as strike/dip/rake.

Moment magnitude, M_w	6.886
Seismic moment, M_0	$2.69E+19$ Nm
Fault plane solution, west segment	$263.31^\circ/60^\circ/-100^\circ$
Fault plane solution, mid segment	$249.66^\circ/60^\circ/-100^\circ$
Fault plane solution, east segment	$257.20^\circ/60^\circ/-100^\circ$
Hypocenter depth	11.09 km
Average stress drop	30 Bar
Asperity stress drop (high-slip)	115.83 Bar
Background stress drop (low-slip)	5.79 Bar
Rise time	1.0 ± 0.4 s
Rupture velocity	2.5 ± 0.5 s
f_{\max}	10 Hz
Q	$82 \cdot f^{-1}$

4.4.2 Gülbahçe fault

Parallel to the east coast of the Karaburun peninsula there is located an almost north-south striking fault with a right bend in the middle part, figure 4.7. Most of the fault is found offshore in the outlet of the İzmir bay, but it becomes visible on land along the Gülbahçe bay before it continues on the seabed south of the peninsula in the Gulf of Sığacık.

Based on the regional stress pattern, the Gülbahçe fault is found to be left lateral strike-slip (Zhu et al., 2006). However, if the geomorphology of the area is taken into account this suggest a right lateral movement, since a bend to the right on a left lateral strike-slip fault would suggest a compression and therefore there is expected a restraining bend with a visible uplift. However, by first view there is observed a lowland north of the fault bend compared to the surroundings.

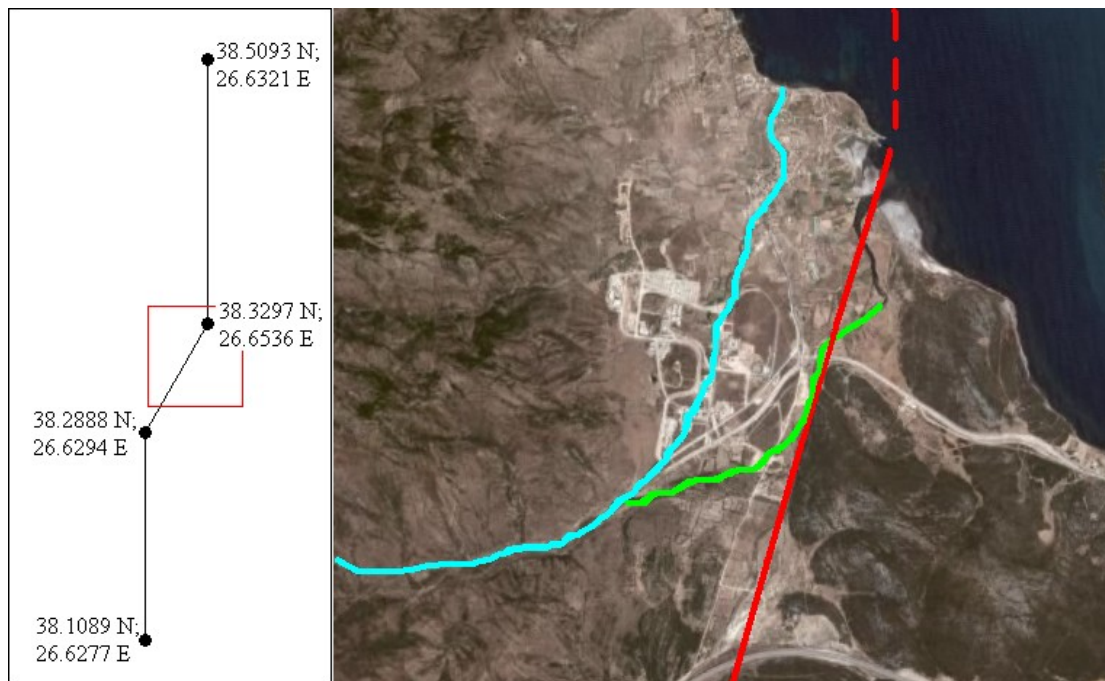


Figure 4.7: Map view of the north-south going Gülbahçe fault. To the left is shown a sketch of the entire fault and the coordinates for the endpoints and the bends are given. To the right is an air-photo of the area around the northern most bend of the fault, approximately marked by the red square in the sketch to the left. The blue line sketches the original river patterns and the green line sketches the deflected river as a consequence of the stress pattern of the region today. The red line shows the fault. (From Google Earth, modified by the author.)

Looking closer into the details of the area, figure 4.7, a river (blue line) is observed in the middle between the two mountain blocks and parallel to the fault trend (red line). Due to the north-northeastern south-southwestern extension (approximately 15° from

north) the left lateral motion and a right bend along the Gülbahçe fault implies a restraining bend with ongoing uplift, which also results in eastern migration of the river channel (green line), see figure 4.7.

In the case of all the strike-slip faults for which there have been made earthquake scenarios in this study, the dip found by the MTA categorize the strike-slip faults in the İzmir area to be vertical (Emre et al., 2005b; Larson, 2006). Experience tells, however, that strike-slip faults are not often completely vertical. The three $M_w=5.4-5.8$ October 17, 2005 earthquakes occurring near the southern part of the Gülbahçe fault, also show a deviation from vertical with focal mechanisms suggesting dips of 85° , 81° and 73° towards west (Benetatos et al., 2006). From this the dip used in the case of the Gülbahçe fault is 80° .

The slip of the fault is determined from the October 17, 2005 earthquake sequence to be -8° , -11° and -25° respectively, these values for rake all correspond to a left lateral strike-slip fault, since they are between -45° and 0° . The value used for the slip in the earthquake scenario is -10° in order to have a large strike-slip component and a smaller normal component.

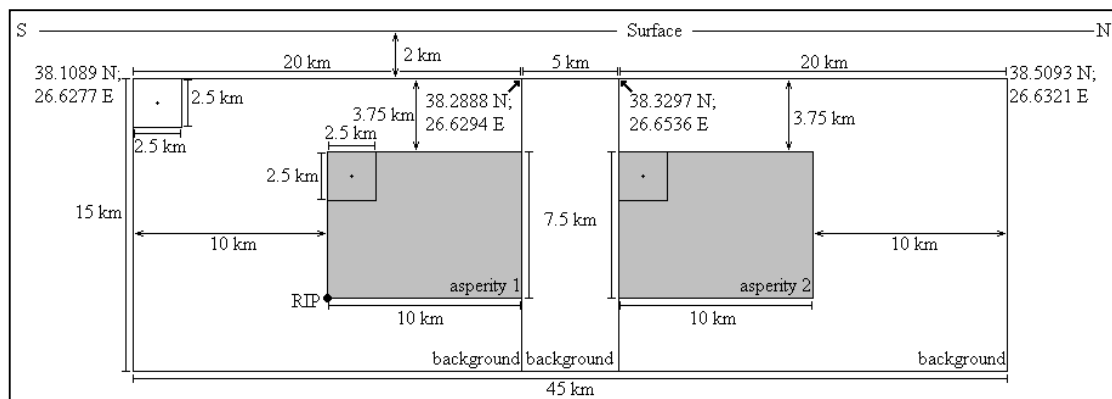


Figure 4.8: Sketch of the Gülbahçe fault placed west of İzmir along the Karaburun peninsula, scenario 2 GF. The coordinates for the start and end points are given, and also the points for the bends. Rupture initiation point (RIP) is found in the lower most southern point of asperity 1

The Gülbahçe fault has ruptured several times during the instrumental time period: in 1953, 1979, 1994 and latest the earthquake sequence on October 17, 2005. All these events have been recorded to have moment magnitudes between 5.0 and 5.8 (Emre et al., 2005a; Emre et al., 2005b).

Figure 4.8 and table 4.11 summarize the parameters used in the ground motion simulation for scenario 2 GF, Gülbahçe fault. On figure 4.8 no asperity is placed in the intermediate fault segment of the Gülbahçe fault.

The choice of the rupture initiation point is based on the earthquake activity during the autumn 2005 in the Gulf of Sığacık. An activity like that may indicate a future larger rupture with a hypocenter close by, therefore the hypocenter in the earthquake scenario for this fault is placed in the southernmost end, on the edge of asperity 1. This also gives rupture propagation northwards that will result in a directivity of seismic waves towards the north, which may partly influence the city of İzmir, especially in the northern part of the city (Karşıyaka).

Table 4.11: The source parameters used in the ground motion simulations for scenarios 2 GF, Gülbahçe fault. The scenario earthquake consists of three segments, a southern, intermediate and a northern part; fault plane solutions are given for all segments. The fault plane solutions are given as strike/dip/rake.

Moment magnitude, M_w	6.939
Seismic moment, M_0	$3.22E+19$ Nm
Fault plane solution, south segment	$180.54^\circ/80^\circ/-10^\circ$
Fault plane solution, mid segment	$210.61^\circ/80^\circ/-10^\circ$
Fault plane solution, north segment	$173.17^\circ/80^\circ/-10^\circ$
Hypocenter depth	13.08 km
Average stress drop	80.18 Bar
Asperity stress drop (high-slip)	309.57 Bar
Background stress drop (low-slip)	15.48 Bar
Rise time	3.0 ± 0.5 s
Rupture velocity	3.0 ± 0.5 s
f_{\max}	10 Hz
Q	$82 \cdot f^{-1}$

A fault length of 45 km might be an underestimate of the dimension for the Gülbahçe fault. The fault extends 70 km towards the north and is interpreted to continue offshore (Altinok et al., 2005; Emre et al., 2005b).

The fault length of 45 km is comparable with the November 12, 1999 strike-slip Düzce earthquake with a magnitude of $M_w=7.2$ that occurred following the August 17, 1999 Izmit earthquake along the North Anatolian Fault. To estimate the strike-slip event on the Gülbahçe fault to be smaller than the Düzce event is reasonable since the rupturing fault is not part of a large fault system like the North Anatolian Fault, and it is not expected to get rupture velocities of 3.5 km/s in the Gülbahçe event as it was observed in the Düzce event, indicating a higher energy release.

4.4.3 Tuzla fault

The Tuzla fault strikes northeast southwest and extends from the Gulf of Sığacık towards the city of İzmir. The fault is not clearly visible on the surface but its existence is indicated by the geomorphology and the hot springs in the south near Doğanbey (figure 4.3).

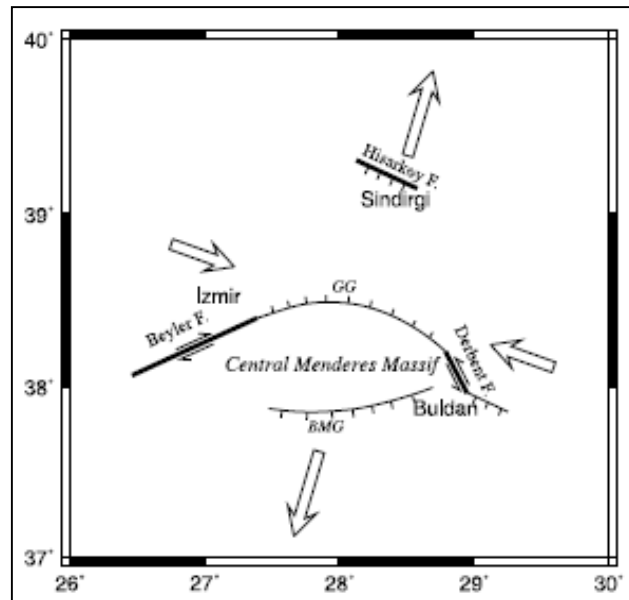


Figure 4.9: A pure-shear model explaining orientations and slip directions of active faults in western Turkey. Arrows show the extensional and compressional directions inferred from averaging all fault plane solutions in the study made by Zhu et al. 2006.

The mechanism of the fault is a right lateral strike-slip fault according to the stress pattern in the area and shown in the study by Zhu et al. (2006) which shows that southwest northeast oriented faults in the study area must be of right lateral strike-slip mechanism according to the regional stress pattern and block rotations of the area. This is illustrated in figure 4.9.

In the intermediate segment of the fault, which is more east west oriented than the two end segments, there is a morphological depression (a valley) between the mountains. This is another indication of a right lateral motion along the Tuzla fault, since a bend to the right will result in a pull-apart basin if the deformation continues. From the instrumental period there is one example of a magnitude 6.0 earthquake on the Tuzla fault in 1992, (Emre et al., 2005b).

The dip of the fault is determined to be vertical (Emre et al., 2005b). However as also mentioned in the description of the Gülbahçe fault this is rarely the case and looking into the Global CMT catalog for fault parameters of the November 6, 1992 event ($M_w=6.0$) occurring at the Tuzla fault gives a dip of $77^\circ-85^\circ$ (Larson, 2006). From this, the dip of the Tuzla fault in the earthquake scenario is assigned to be 80° .

The rake of the Tuzla fault is said to be -167° . This is consistent with a right lateral strike-slip motion with a minor normal component. The value for the rake is based on the focal mechanism of the November 6, 1992 earthquake.

The geometry and the parameters of the earthquake scenario at the Tuzla fault are summarized in figure 4.10 and table 4.12. The asperity on the middle segment of the fault is made relatively smaller compared to the background area of the other segments. This geometry is selected since the middle part of the segment indicates a pull-apart basin. Along this fault segment less slip is therefore expected to occur during a future rupture.

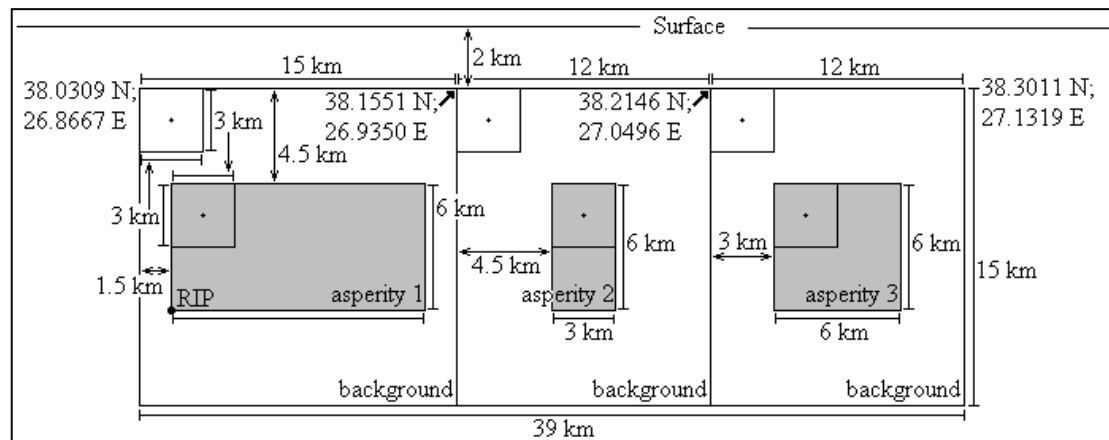


Figure 4.10: Sketch of the Tuzla fault striking from Sığacık in the southwest to İzmir in the northeast, scenario 3 TF. The coordinates for the start and end points are given, and also the points for the bends. Rupture initiation point (RIP) is found in the lower most southern point of asperity 1.

The rupture initiation point of the earthquake scenario of the Tuzla fault is placed in the southern end of the fault to ensure rupture directivity towards İzmir and thereby create a worst-case scenario for the city of İzmir.

Table 4.12: The source parameters used in the ground motion simulations for scenario 3 TF, Tuzla fault. The scenario earthquake consists of three segments, a southern, intermediate and a northern part; fault plane solutions are given for all segments. The fault plane solutions are given as strike/dip/rake.

Moment magnitude, M_w	6.872
Seismic moment, M_0	$2.59E+19$ Nm
Fault plane solution, south segment	$28.81^\circ/80^\circ/-167^\circ$
Fault plane solution, mid segment	$62.56^\circ/80^\circ/-167^\circ$
Fault plane solution, north segment	$43.57^\circ/80^\circ/-167^\circ$
Hypocenter depth	12.34 km
Average stress drop	79.04 Bar
Asperity stress drop (high-slip)	305.17 Bar
Background stress drop (low-slip)	15.26 Bar
Rise time	3.0 ± 0.5 s
Rupture velocity	3.0 ± 0.5 s
f_{max}	10 Hz
Q	$82 \cdot f^{-1}$

4.4.4 Seferihisar fault

The Seferihisar fault is located west of the Tuzla fault and east of the city Urla. The fault starts in the south in the Gulf of Sığacık and ends in the north close to the western most point of the İzmir fault. The fault is by the MTA defined to have a strike of 20°N and dipping towards east (Emre et al., 2005b). However, the mapping of the fault is just west of the mountain range separating the Tuzla and Seferihisar fault, and the fault must therefore dip towards west resulting in a strike of approximately 200°N .

The Seferihisar fault is known to have ruptured in recent times, latest in 2003, where an earthquake with a moment magnitude of 5.6 was recorded (Emre et al., 2005b).

The Seferihisar fault has a northeast southwest orientation similar to the Tuzla fault, and is therefore a right lateral strike-slip fault, (Zhu et al., 2006). As discussed earlier, the dip of the fault is by the MTA determined to be vertical, however earthquake focal mechanisms from the April 10 and 17, 2003 events, with M_w of 5.7 and 5.2 respectively, yields a fault dip of 76° - 79° (Benetatos et al., 2006; Larson, 2006). In the Seferihisar fault earthquake scenario the dip has been set to 80° , similar to the other strike-slip faults in this study.

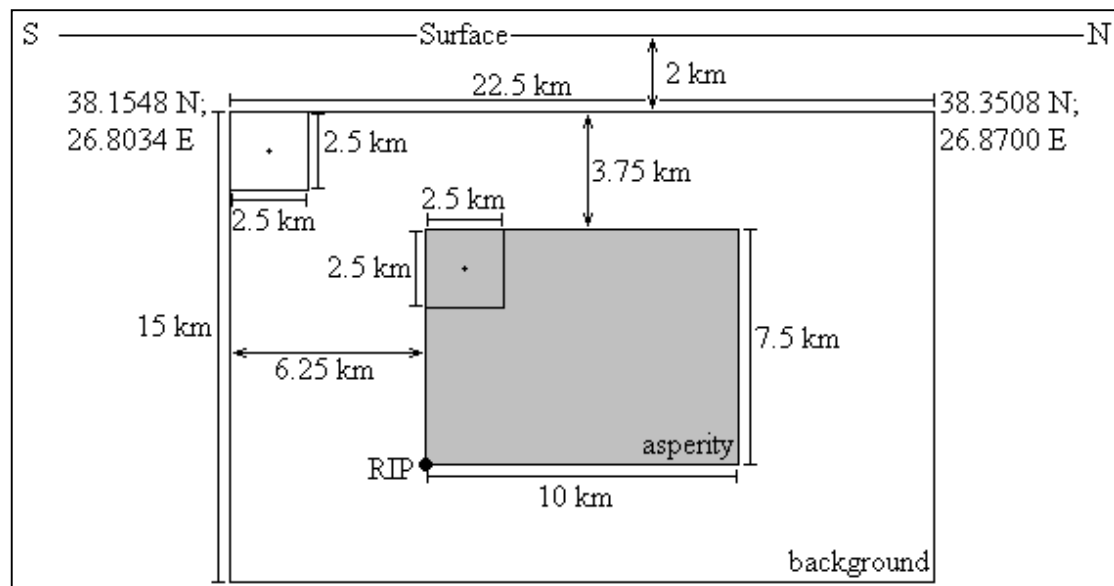


Figure 4.11: Sketch of the Seferihisar fault striking from the city Seferihisar in the south and parallel to the mountain range separating the Tuzla and the Seferihisar fault. The end of the fault in the northern end is close to the western most point of the İzmir fault. The coordinates for the start and end points are given, and the rupture initiation point (RIP) is found in the lower southern corner of the asperity.

The slip of the fault is determined to be -149° , which is the average slip of the two April 2003 event (-159° and -139° respectively), (Larson, 2006). This corresponds to a right lateral strike-slip fault, as it was predicted by the study of Zhu et al. (2006). The normal component in this focal mechanism is slightly larger than in the case of the Tuzla fault. The geometry and the parameters of the earthquake scenario on the Seferihisar fault are summarized in figure 4.11 and table 4.13.

Table 4.13: The source parameters used in the ground motion simulations for scenario 4 SF, Seferihisar fault. The fault plane solution is given as strike/dip/rake.

Moment magnitude, M_w	6.617
Seismic moment, M_0	1.06E+19 Nm
Fault plane solution	198.77°/80°/-149°
Hypocenter depth	12.59 km
Average stress drop	74.58 Bar
Asperity stress drop (high-slip)	287.95 Bar
Background stress drop (low-slip)	14.40 Bar
Rise time	3.0 ± 0.5 s
Rupture velocity	3.0 ± 0.5 s
f_{\max}	10 Hz
Q	$82 \cdot f^{-1}$

The rupture initiation point of the fault is located in the southern end of the fault to obtain the directivity effect of the wave propagation, resulting in higher ground motion towards İzmir. Also the high seismic activity in the Gulf of Siğaçık in the autumn of 2005 can, as it was mentioned in the description of the Gülbahçe fault, be interpreted as a precursor for a possible large earthquake. The probable hypocenter will then most likely be found close to this pre-seismicity.

4.4.5 Manisa fault

The Spil Mountain (figure 4.3) north of İzmir is approximately 50 km long and 15 km wide. On the northern and eastern side this block is bounded by a normal fault following the topographical boundary between the mountain and the valley. The fault runs parallel to the block from west of Manisa and bends along the mountain block in the east and continues in the lower-lying area for finally to pass Turgutlu, see figure 4.3.

Due to excavation of sediments in the area on the northeastern side of the mountain block the fault plane is clearly exposed on the surface, shown in figure 4.12.



Figure 4.12: The fault plane of the Manisa fault is visible due to excavation in the area. Several smaller pictures, all taken on the northeastern side of the mountain block, along which the Manisa fault is located, are joined together to make a panorama of the area. The height of the visible part of the fault plane is estimated to be 60 m. (Bozkurt and Sözbilir, submitted) The author took the pictures during a field trip to the fault in October 2006.

Due to the large deviation in the strike along the Manisa fault, the fault has in this study been divided into three segments: western, intermediate and eastern. For all three segments the ground motion simulations are based on earthquake scenarios at only one segment at a time. The bends separating the segments are assumed to be too large to let the rupture propagate, and the three segments are therefore treated separately in the ground motion simulations.

The dip of the fault is determined in several studies, but it is not constant along the whole fault, and even in a small distance of a few meters the dip changes with several degrees. Bozkurt and Sözbilir (submitted) have in a thorough study of the Manisa fault found the dip to vary between 36° and 58° towards east and southeast. On single locations where measurements have been made the average dip is found to be 49° - 50° (Bozkurt and Sözbilir, submitted). In the study conducted by the MTA the average dip

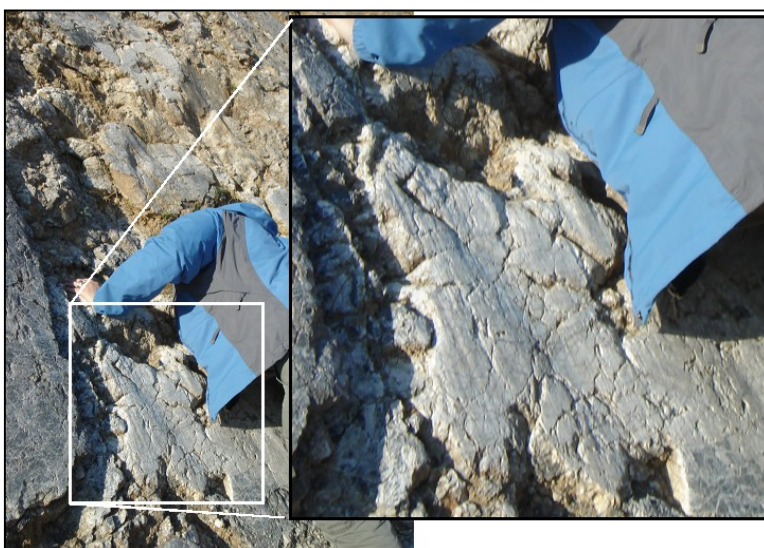


Figure 4.13: Slickensides at the fault plane of the Manisa fault. Mathilde Böttger Sørensen as scale.

is found to be 55° (Emre et al., 2005b). During the field trip to İzmir in the autumn of 2006 the dip of the fault was measured on two locations, both locations had large deviations in the dip in a short horizontal distance. The dip of the Manisa fault was measured to be

between 40° - 56° . The dip used in the scenario earthquake is based on the work done by Bozkurt and Sözbilir (submitted) and own observations, and is assumed to be 48° .

At the exposed fault plane almost vertical slickensides were clearly observed, see figure 4.13. This indicates an almost pure normal component, which is consistent with the value of -83° (rake found in the study of the Manisa fault (Bozkurt and Sözbilir, submitted)). In the earthquake scenarios for the three segments of the Manisa fault a slip of 83° is adopted.

The fault is active as was manifested by an $M_w=5.2$ earthquake in 1994 (Emre et al., 2005b). There are also records of a historical $M_w=6.7$ earthquake in 1845, (Papazachos and Papazachou, 1997).

5A WMF, Western Manisa Fault segment

Scenario 5A WMF is the earthquake scenario simulated on the most western part of the Manisa fault. The geometry and the parameters of the earthquake scenario on the western segment of the Manisa fault are summarized in figure 4.14 and table 4.14.

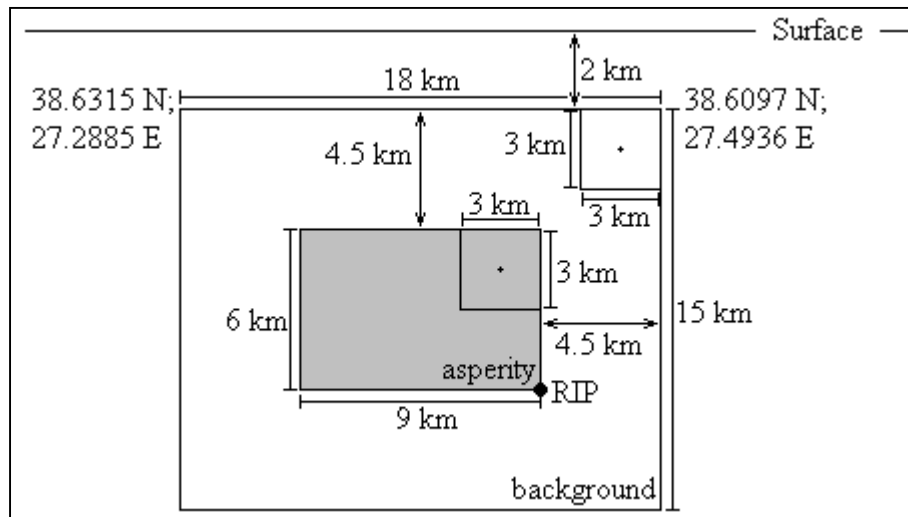


Figure 4.14: Sketch of the western segment of the Manisa fault, scenario 5A WMF. The coordinates for the start and end points are given. Rupture initiation point (RIP) is found in the lower most eastern part of the asperity.

The rupture initiation point of the earthquake scenario is placed in order to produce a worst-case scenario in respect of ground motions in the center of İzmir, and therefore the rupture is simulated to propagate from east to west in order to get a directivity effect towards the city.

Table 4.14: The source parameters used in the ground motion simulations for scenario 5A WMF, Western Manisa fault. The fault plane solution is given as strike/dip/rake.

Moment magnitude, M_w	6.463
Seismic moment, M_0	6.24E+19 Nm
Fault plane solution	276.07°/48°/-83°
Hypocenter depth	9.80 km
Average stress drop	30 Bar
Asperity stress drop (high-slip)	115.83 Bar
Background stress drop (low-slip)	5.79 Bar
Rise time	1.0 ± 0.4 s
Rupture velocity	2.5 ± 0.5 s
f_{max}	10 Hz
Q	82 · f^{-1}

5B IMF, Intermediate Manisa Fault segment

The earthquake scenario on the intermediate Manisa fault is on a slightly shorter fault than in the case of the western segment. The end point in the west of this segment corresponds to the easternmost end point of the western segment of the Manisa fault. In the east the segment is bounded by the eastern segment of the fault. The geometry and the parameters for the earthquake scenario on the intermediate segment of the Manisa fault are given in figure 4.15 and table 4.15.

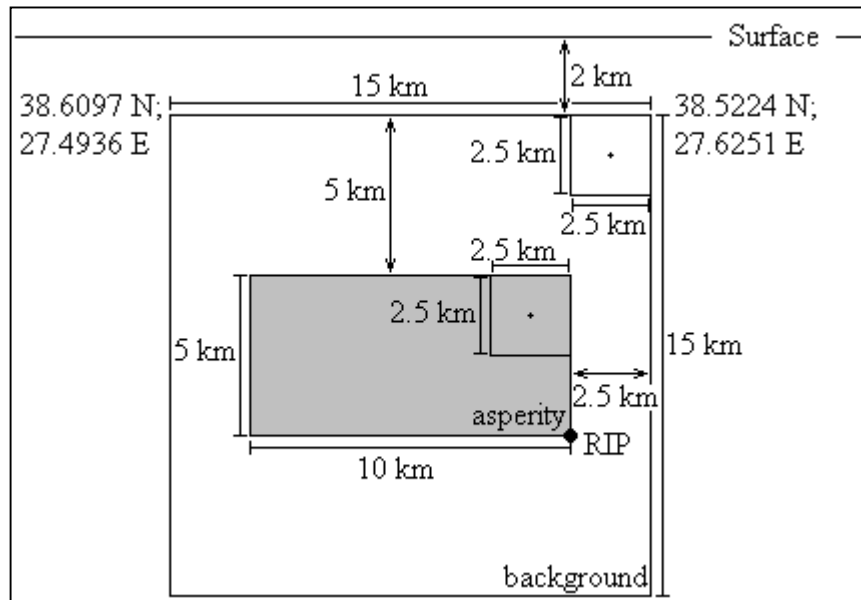


Figure 4.15: Sketch of the intermediate segment of the Manisa fault, scenario 5B IMF. The coordinates for the start and end points are given. Rupture initiation point (RIP) is found in the lower most eastern part of the asperity.

The rupture initiation point is, as in the case for the western segment, placed in the eastern lower corner of the asperity in order to construct a worst-case scenario for the city of İzmir.

Table 4.15: The source parameters used in the ground motion simulations for scenario 5B IMF, Intermediate Manisa fault. The fault plane solution is given as strike/dip/rake.

Moment magnitude, M_w	6.371
Seismic moment, M_0	6.24E+19 Nm
Fault plane solution	303.58/48°/-83°
Hypocenter depth	9.43 km
Average stress drop	30 Bar
Asperity stress drop (high-slip)	115.83 Bar
Background stress drop (low-slip)	5.79 Bar
Rise time	1.0 ± 0.4 s
Rupture velocity	2.5 ± 0.5 s
f_{max}	10 Hz
Q	82 · f^{-1}

5C EMF, Eastern Manisa Fault segment

The eastern segment of the Manisa fault is the longest of the Manisa segments with 22.5 km. The fault strikes in a more east west oriented direction than the intermediate segment, since it no longer follows the Spil mountain range but instead runs in the valley towards Gediz graben.

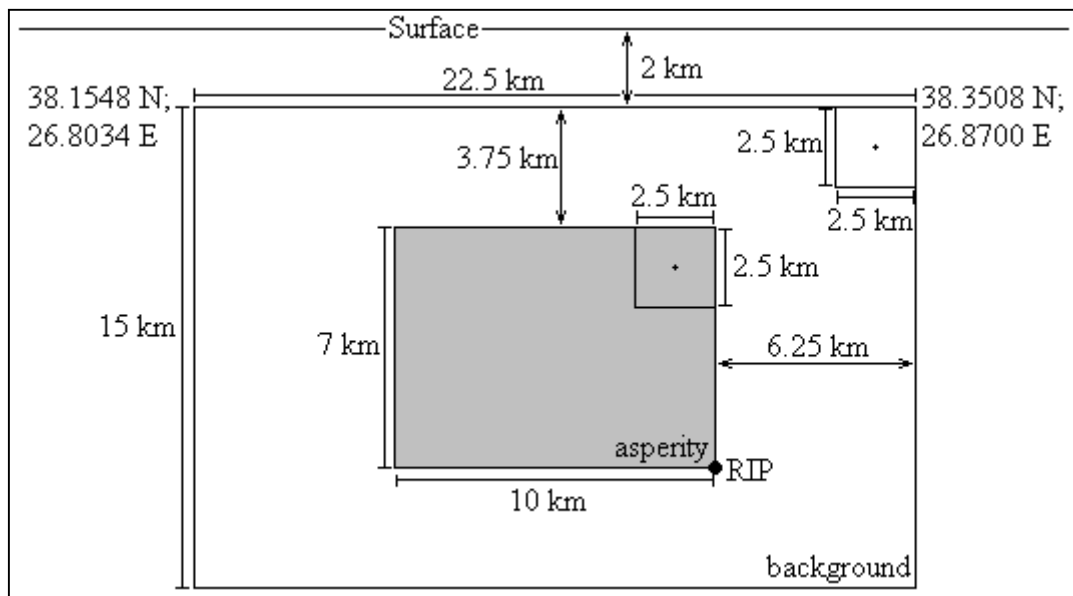


Figure 4.16: Sketch of the eastern segment of the Manisa fault, scenario 5C EMF. The coordinates for the start and end points are given. Rupture initiation point (RIP) is found in the lower most eastern part of the asperity.

The details of the eastern segment of the Manisa fault are given in figure 4.16 and in table 4.16, where the parameters used in the scenario earthquake are given.

Table 4.16: The source parameters used in the ground motion simulation 5C EMF, East Manisa fault. The fault plane solution is given as strike/dip/rake.

Moment magnitude, M_w	6.577
Seismic moment, M_0	6.24E+19 Nm
Fault plane solution	277.39°/48°/-83°
Hypocenter depth	9.99 km

Average stress drop	30 Bar
Asperity stress drop (high-slip)	115.83 Bar
Background stress drop (low-slip)	5.79 Bar
Rise time	1.0 ± 0.4 s
Rupture velocity	2.5 ± 0.5 s
f_{\max}	10 Hz
Q	$82 \cdot f^{-1}$

The rupture initiation point of the scenario earthquake is placed in the lower eastern corner of the asperity in order to ensure the directivity effect to be towards İzmir and thereby creating a worst-case scenario for the city.

4.5 Databases

During the work with this thesis several different databases were created such as a database containing all relevant information in order to conduct the ground motion modeling and different earthquake catalogs. These different databases are all described in the following.

4.5.1 Fault parameter database

The conduct of the ground motion simulations in this study is based on a program package consisting of different Fortran™ programs and Matlab™ scripts (for description see appendix E). For the Fortran programs there are various input files, as there are several different Matlab scripts that are used to run the routines in Matlab. The parameters used in describing the earthquake scenario are therefore typed in several times during a single ground motion simulation. In order to keep track of these parameters an Excel-file is developed, which is used for each earthquake scenario and contains spreadsheets for all the programs used in a ground motion simulation. During the work with this study these spreadsheets are adopted and improved.

There is an Excel-file for each earthquake scenario and hence a database, which contains all needed information about the faults in the near range of İzmir in order to calculate ground motion simulations. This database is useful for keeping track of the used parameters and for future ground motion simulations on the same faults with a

variety of parameters. The database is included in Appendix F, and is also available on the appended CD.

4.5.2 Point calculations

As mentioned in the section 4.3.1 a spreadsheet is developed, which calculates the different points needed in order to define the background, the asperity and the hypocenter on a fault plane with correct geographical coordinates. The only input needed in order to obtain these points on the fault plane is the end points of the fault and the dip of the fault.

Having prepared this spreadsheet result is faster calculations of the points and a decrease in the amount of possible mistakes in the manual calculations. One feature missing in this Excel-sheet is the ability to take the geometry of the fault into account automatically, and thereby decide if the small contributions in the east west or north south directions should be added or subtracted from the reference point. A more thorough description of the spreadsheet and this geometry problem is given in Appendix C, where also the spreadsheet used in this study is available.

4.5.3 Earthquake catalogs

In order to investigate the seismic activity for a background study of the entire Mediterranean region Centroid-Moment Tensor (CMT) solutions were gathered from the databases of several different institutions: Aristotle University of Thessaloniki (AUTH), Centre Polynésien de Prévention des Tsunamis (CPPT), Eidgenössische Technische Hochschule Zürich (ETHZ), Istituto Nazionale di Geofisica (ING), Istituto Nazionale di Geofisica e Vulcanologia (INGV), Institut de Physique du Globe de Paris (IPGP), Kandilli Observatory and Earthquake Research Institute (KOERI), National Observatory of Athens (NOA), Uppsala University (UPSL), United States Geological Survey (USGS) and Global moment tensor solutions. The catalogs from the agencies AUTH, CPPT, ETHZ, ING, INGV, IPGP, KOERI, NOA and UPSL are obtained from the homepage of the European-Mediterranean Seismological Center (EMSC), while the catalogs from USGS and the Global

Centroid Moment Tensor solutions (global CMT) have been obtained from their respective homepages (EMSC, 2007; Larson, 2006; USGS, 2007).

When all the existing catalogs were gathered into one file, the total number of events was 1490 in the time span from 1976 to March 2007. However, there were several duplicates in the combined catalog, and therefore a catalog clean up has been conducted in order to remove these. The criteria for removing events were set up by combining occurrence time, location and magnitudes for the recorded events. When deleting an event in the compiled catalog the record containing most information and details of the duplicated event has been kept. After the catalog clean up 1116 events were left, that is 374 events were removed. The magnitude range for the catalog is $2.9 < M_w < 8.9$, however, no attempt was done in unifying the magnitudes as it is outside the scope of this work. Since the earthquake catalog is not used directly in the ground motion simulations, this possible variation on the magnitude types will therefore not affect the simulation results.

All the events in the combined earthquake catalog contain information of at least one nodal plane. In order to be able to graphically show the pure double couple of the focal mechanisms on a map by GMT (see figure 2.2) however, two nodal planes are needed. For this reason 710 events were extracted (time span: 1976-2006) for which all information on the two nodal planes was available. This part of the catalog is gathered from the databases of INGV, USGS and global CMT solutions (Larson, 2006; Pondrelli et al., 2004; Pondrelli et al., 2002; Pondrelli et al., 2006; USGS, 2007) and the two databases are given on the enclosed CD.

For investigating the seismic activity in the local area around İzmir an earthquake catalog has been gathered with information on time of occurrence, location and magnitude and intensity. This catalog contains events with magnitudes larger than 6 (though for the last years in the catalog, events of magnitude 5.2 are also mentioned). This earthquake catalog covers a time span from 496 BC to 1994 and is based upon literature from Papazachos et al. (1997), Papazachos and Papazachou (1997) and Ambraseys and Finkel (1995). This catalog is also given on the enclosed CD.

5 Ground motion simulation results

The results obtained from the ground motion simulations from the nine different earthquake scenarios are given in this chapter. For each scenario waveforms are calculated at all the simulation sites in the study area (longitude 25.4° - 29° and latitude 37° - 39.8°). The calculations have been made for bedrock conditions. In order to get an insight in the distribution of strong ground motion the peak ground motions (PGA and PGV) for each simulation point have been extracted and plotted on separate maps. For each earthquake scenario input and output of the calculations are summarized in a separate table. Finally, waveforms for each scenario in both acceleration and velocity are calculated for the station located in the İzmir center. The corresponding frequency spectra are also shown in separate diagrams.

The duration of the obtained waveforms are calculated on the vertical component of the acceleration time series. This is found by using the SEISAN program package (Havskov and Ottemöller, 2003). The durations are determined from the ratio between the short-term average (STA) and the long-term average (LTA) of the signal. STA/LTA ratio of 1.2 is adopted. Due to short durations of signals STA over 1 second is used. Furthermore the signals have all been band pass filtered at 10-15 Hz.

5.1 İzmir Fault

On the İzmir fault three different rupture scenarios were used to perform the ground motion simulations: two segments alone and a rupture of the combined two segments with a 3 kilometer segment in between (described in section 4.4.1). The earthquake scenarios on the İzmir fault are all of normal mechanisms on east-west striking faults with dips of 60° to the north.

5.1.1 1A WIF, Western İzmir Fault segment

The peak ground motions for the earthquake scenario on the western segment of the İzmir fault are given in figure 5.1, showing an even distribution of ground motion on both the footwall and hanging wall block for the peak ground acceleration as well as the velocity. The strongest ground shaking occurs close to the rupturing fault plane and is centered at the fault plane in line with the location of the asperity. The distribution of the significant part of the peak ground acceleration and velocity covers more or less the same area.

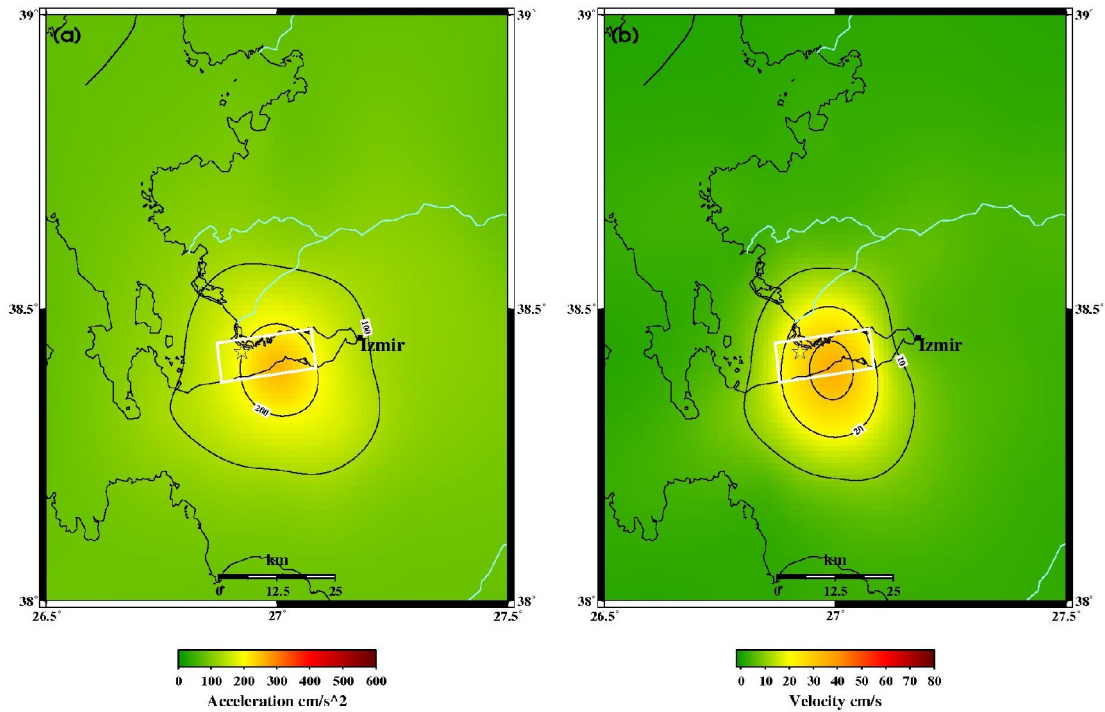


Figure 5.1: Peak ground motion distribution in the area around İzmir due to the earthquake scenario on the western segment of the İzmir fault. (a) Peak ground acceleration (cm/s^2) and (b) peak ground velocity (cm/s). The white boxes illustrate the surface projection of the fault plane. The yellow star shows the location of the epicenter. The city center of İzmir is given as a black dot, indicating the station for which the waveforms below are given.

The parameters obtained for the earthquake scenario are given in table 5.1 and the details of the input parameters are summed up in table 4.8.

Table 5.1: The primary input parameters used and output parameters obtained in the ground motion simulations for the scenario 1A WIF, Western İzmir Fault. The fault plane solution is given as strike/dip/rake.

Moment magnitude, M_w	6.463
Fault plane solution	263.31°/60°/-100°
Hypocenter depth	11.09 km
PGA, scenario, max	256 cm/s^2
PGV, scenario, max	35 cm/s
PGA, İzmir	150.9 cm/s^2

PGV, İzmir	10.3 cm/s
Signal duration	5 s

The seismograms and corresponding frequency spectra calculated for the earthquake scenario on the western part of the İzmir fault are shown in figure 5.2. It is seen that the acceleration time series have much higher frequency content than the velocity time series, which is to be expected. The spectra in the bottom of figure 5.2 reveal the variation within the whole frequency range (0.1-10 Hz).

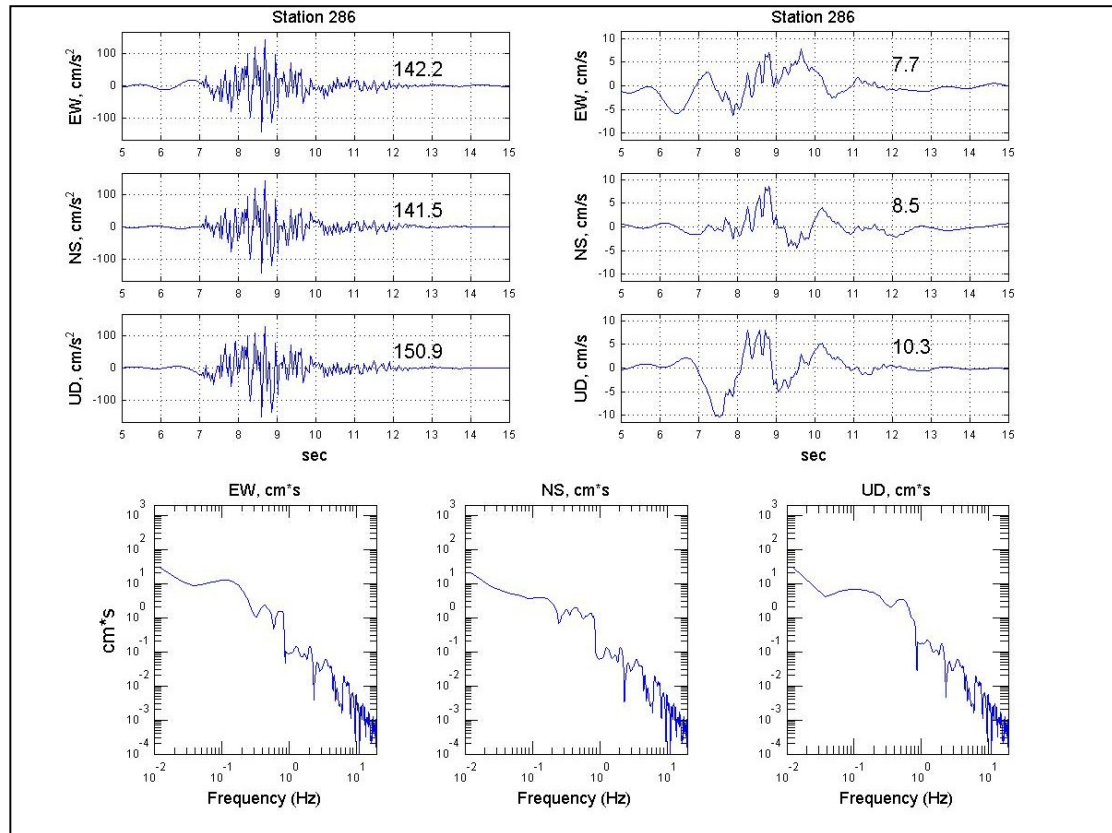


Figure 5.2: Simulated waveforms for the earthquake scenario on the western İzmir fault segment. Left is the acceleration and right is the velocity time series. In the bottom of the figure the spectras for the east-west, north-south and the vertical components are shown.

The duration of the ground shaking at the station located in İzmir is determined to be 5 seconds. The peak ground motions simulated for the station in İzmir are only approximately 60% and 30% of the peak ground acceleration and velocity for the entire scenario respectively. This is because the ruptured fault is located away from the station, where the attenuation of seismic waves becomes significant.

5.1.2 1B EIF, Eastern İzmir Fault segment

The peak ground motions for the earthquake scenario on the eastern segment of the İzmir fault are given in figure 5.3. The distribution of significant ground motions is divided equally on both the footwall and the hanging wall block for the peak ground acceleration as well as the velocity.

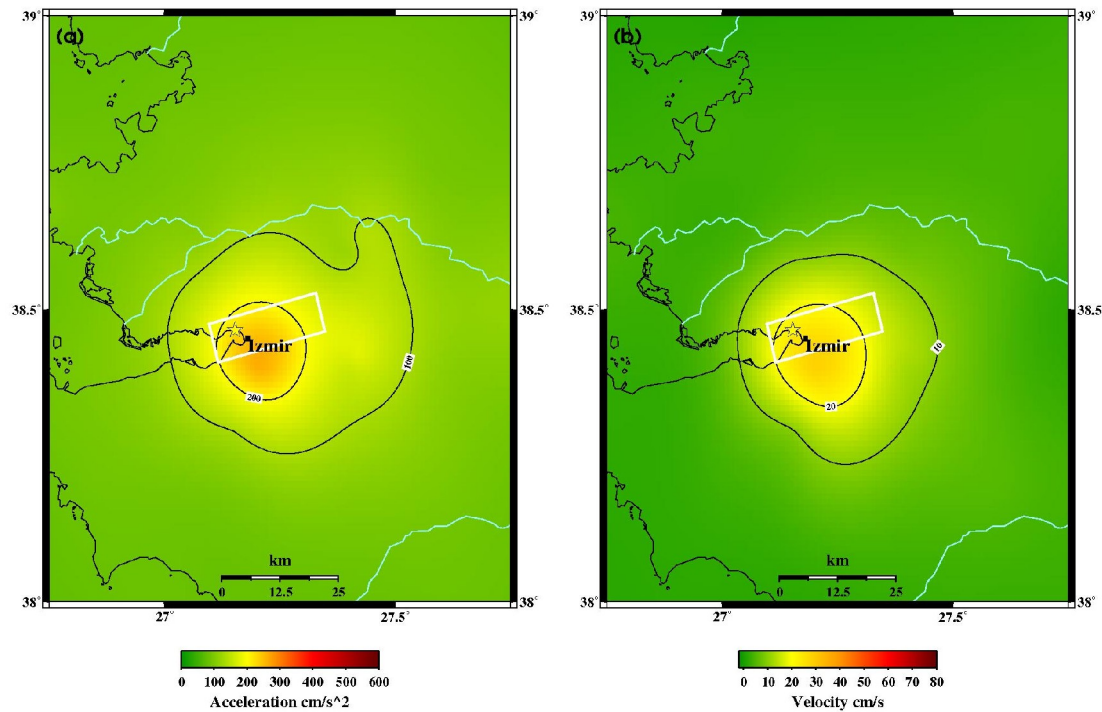


Figure 5.3: Peak ground motion distribution in the area around İzmir due to the earthquake scenario on the eastern segment of the İzmir fault. (a) Peak ground acceleration (cm/s^2) and (b) peak ground velocity (cm/s). The white boxes illustrate the surface projection of the fault plane. The yellow star shows the location of the epicenter. The city center of İzmir is shown as a black dot, indicating the station for which the waveforms given below are obtained.

The directivity effect is observed, especially regarding the acceleration. The strongest ground shaking occurs close to and above the rupturing fault plane according to the location of the asperity. The distribution of significant peak ground acceleration and velocity covers more or less the same area.

The parameters obtained for the earthquake scenario are given in table 5.2, the details of the input parameters are summed up in table 4.9.

Table 5.2: The primary input parameters used and output parameters obtained in the ground motion simulations for the scenario 1B EIF, Eastern İzmir Fault. The fault plane solution is given as strike/dip/rake.

Moment magnitude, M_w	6.542
Fault plane solution	257.20°/60°/-100°
Hypocenter depth	11.09 km

PGA, scenario, max	262 cm/s ²
PGV, scenario, max	28 cm/s
PGA, İzmir	226.6 cm/s ²
PGV, İzmir	23.5 cm/s
Signal duration	7 s

The seismograms and corresponding frequency spectra calculated for the earthquake scenario on the eastern part of the İzmir fault are shown in figure 5.4. The acceleration time series have much higher frequency content than the velocity time series. The spectra in the bottom of figure 5.4 reveal the variation for the whole frequency range (0.1-10 Hz).

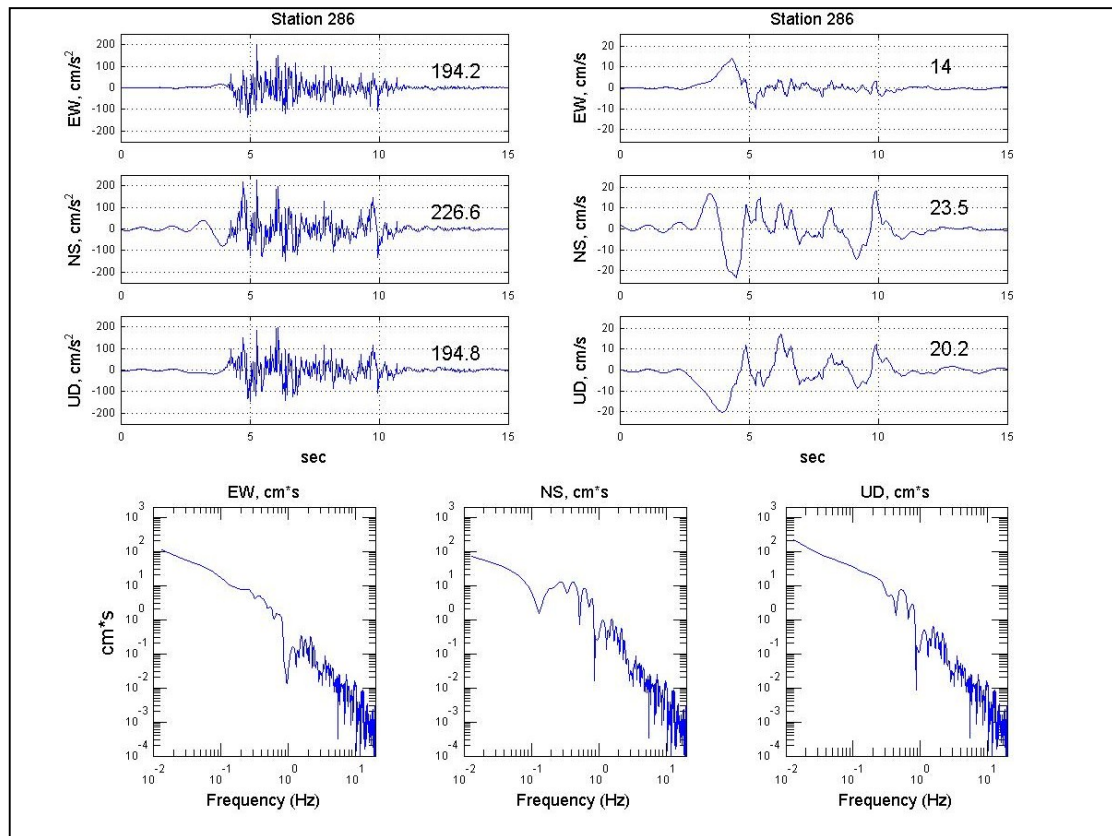


Figure 5.4: Synthetic waveforms for the earthquake scenario on the eastern İzmir fault segment. The acceleration is shown on the left and the velocity on the right. In the bottom of the figure the spectras for the east-west, north-south and vertical components are shown.

The duration of the ground shaking is determined from the waveform of the vertical acceleration signal and is found to be of 7 seconds. The values for the maximum peak ground motions and the peak ground motions observed in the city of İzmir are comparable. The peak ground motions in İzmir are approximately 80% of the peak ground motions in the scenario. This is because the ruptured fault crosses the city center of İzmir.

5.1.3 1C IF, İzmir Fault

The earthquake scenario 1C IF is built up of a combined rupture on the two segments from scenario 1A WIF and 1B EIF. The peak ground motions for the earthquake scenario on the İzmir fault are given in figure 5.5.

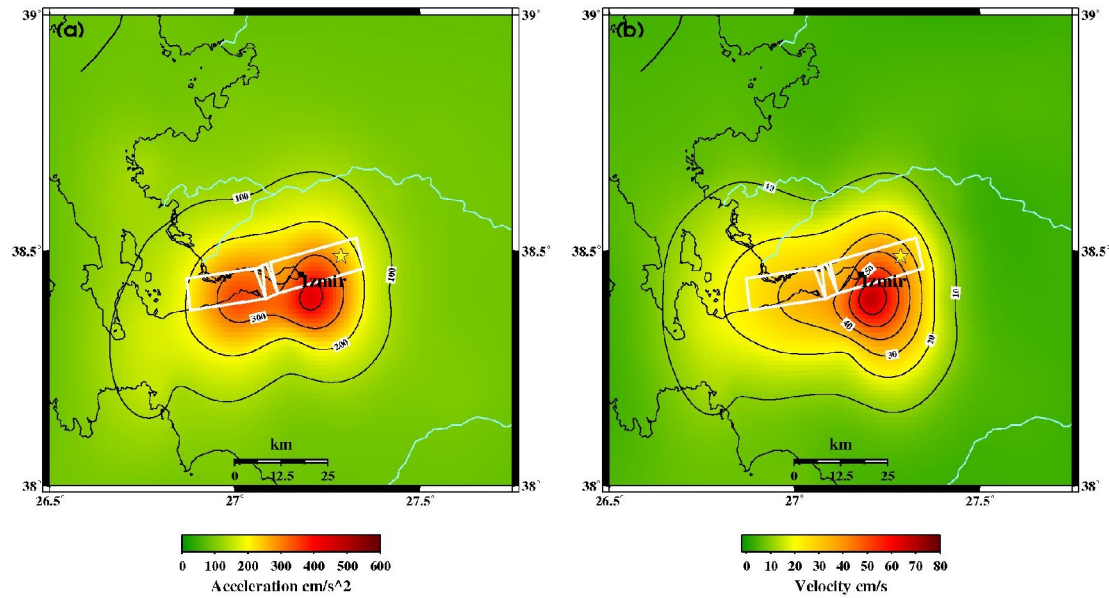


Figure 5.5: Peak ground motion distribution in the area around İzmir due to the earthquake scenario on the İzmir fault consisting of both the western and the eastern fault segments. (a) Peak ground acceleration (cm/s^2) and (b) peak ground velocity (cm/s). The white boxes illustrate the surface projection of the fault plane segments. The yellow star shows the location of the epicenter. The city center of İzmir is shown as a black dot, indicating the station for which the waveforms given below are obtained.

The distribution of significant ground acceleration and velocity is relatively homogeneous and is divided equally on both the footwall and the hanging wall block. The strongest ground shaking occurs close to and above the rupturing fault plane in line with the location of the asperities - especially the asperity in the easternmost segment - for the rupture scenario in which the hypocenter is placed. Indications of the directivity effect in the ground motion distribution for both acceleration and velocity towards the west are observed.

The parameters obtained for the earthquake scenario are given in table 5.3, the details of the input parameters are summed up in table 4.10.

Table 5.3: The primary input parameters used and output parameters obtained in the ground motion simulations for the scenario 1C IF, İzmir Fault. The fault plane solutions are given as strike/dip/rake.

Moment magnitude, M_w	6.886
Fault plane solution, west segment	263.31°/60°/-100°
Fault plane solution, mid segment	249.66°/60°/-100°

Fault plane solution, east segment	257.20°/60°/-100°
Hypocenter depth	11.09 km
PGA, scenario, max	438 cm/s ²
PGV, scenario, max	68 cm/s
PGA, İzmir	291.4 cm/s ²
PGV, İzmir	47.6 cm/s
Signal duration	13 s

The seismograms and the corresponding frequency spectra calculated for the earthquake scenario on the western part of the İzmir fault are shown in figure 5.6. The spectra in the bottom of figure 5.6 reveal that the simulated ground motions show significant variation for the whole frequency range (0.1-10 Hz).

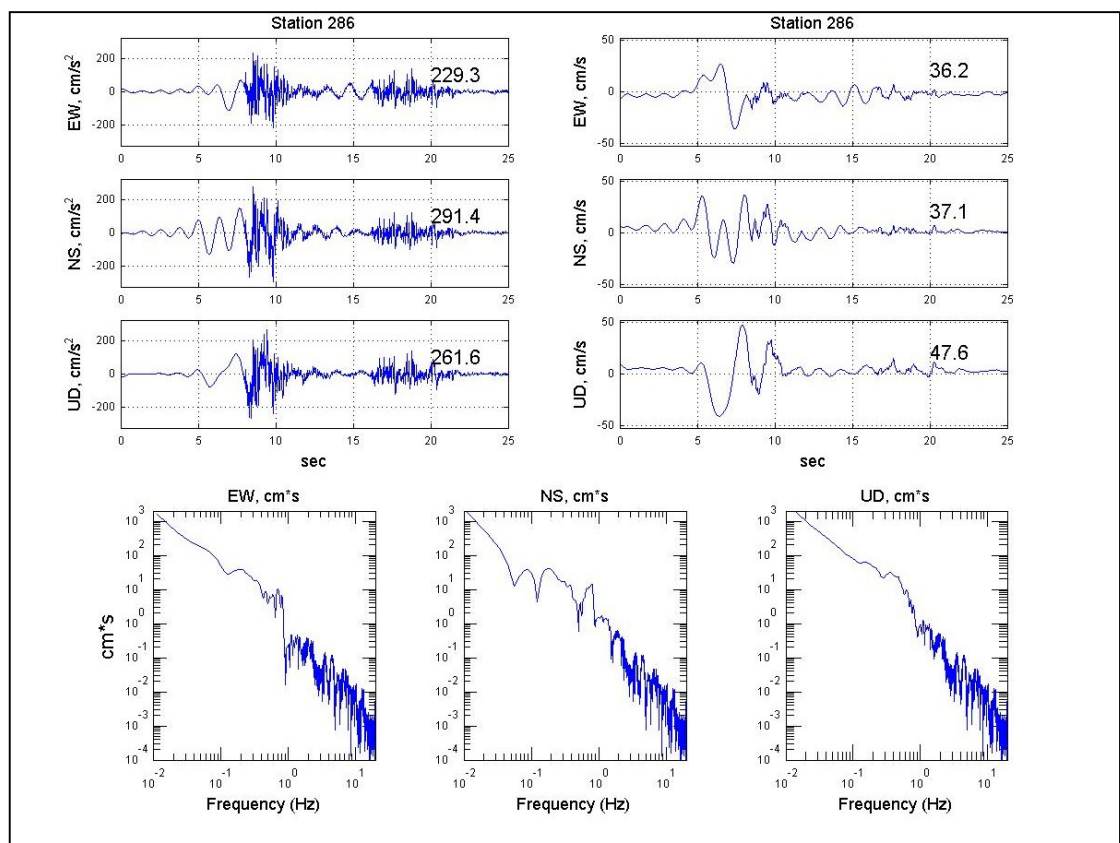


Figure 5.6: Simulated waveforms for the earthquake scenario on the İzmir fault consisting of both the western and the eastern fault segments. To the left the acceleration and to the right the velocity time series are shown. In the bottom of the figure the spectras for the east-west, north-south and vertical components are shown.

The waveforms for the combined rupture of the two segments of the İzmir fault are of longer duration and with larger peak values than the waveforms for the two segments alone. The duration of the signal, simulated for the center of İzmir, is of 13 seconds. The contributions of the simulated ground motions from the two segments are easily observed in figure 5.6, especially in the case of the simulated acceleration waveform. The ruptured fault is located underneath the station for the İzmir center and the peak

ground motions observed in İzmir correspond to approximately 70% of the peak ground motions for the earthquake scenario, which indicates that the waves have not been significantly attenuated due to the short distance from the fault to the station in İzmir center.

5.2 Gülbahçe Fault

On the Gülbahçe fault a single earthquake scenario is considered along a 45 km long fault with a right bend in the middle. The earthquake scenario on the fault is of strike-slip mechanisms on a north-south striking fault with a dip of 80° to the west. The earthquake scenario is described in section 4.4.2.

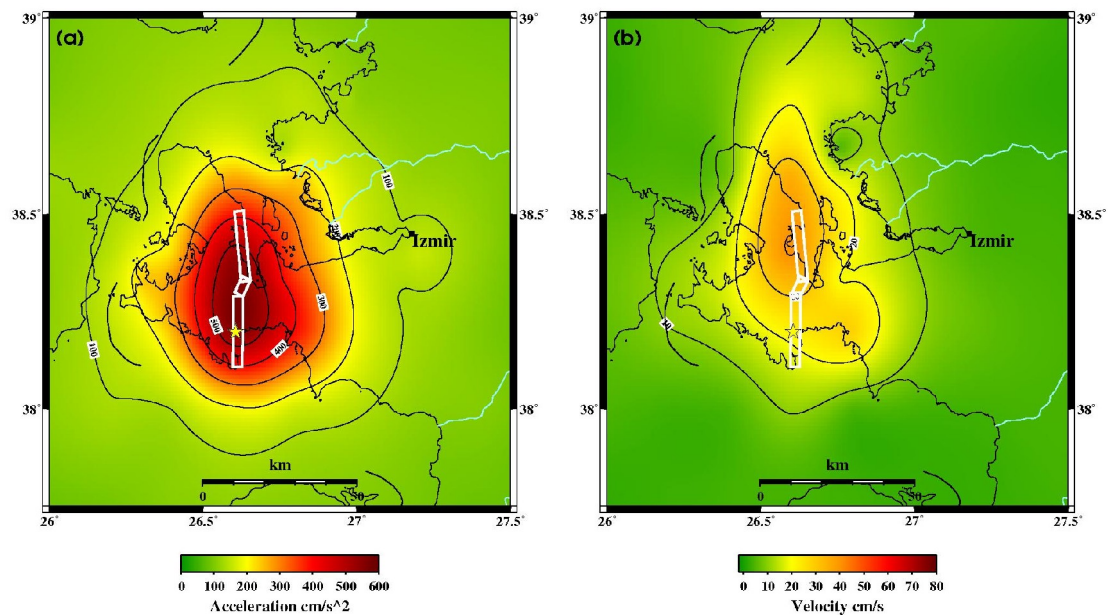


Figure 5.7: Peak ground motion distribution in the area around İzmir due to the earthquake scenario on the Gülbahçe fault. (a) Peak ground acceleration (cm/s^2) and (b) peak ground velocity (cm/s). The white boxes illustrate the surface projection of the fault plane segments. The yellow star shows the location of the epicenter. The city center of İzmir is given as a black dot, indicating the station for which the waveforms given below are obtained.

The peak ground motions for the earthquake scenario on the Gülbahçe fault are shown in figure 5.7. The distribution of significant ground motion is divided equally on both sides of the fault. The pattern for the ground motions is elongated in the north-south direction corresponding to the geometry of the fault. The directivity effect of the ground motions is especially observed in the figure showing the peak ground velocity. The strongest ground shaking, when it comes to the ground acceleration, is located on top of the central part of the fault. In case of the ground velocity the strongest motion

is moved to the northern part of the fault as a consequence of the directivity of the seismic waves.

Table 5.4: The primary input parameters used and output parameters obtained in the ground motion simulations for the scenario 2 GF, Gülbahçe Fault. The fault plane solutions are given as strike/dip/rake.

Moment magnitude, M_w	6.881
Fault plane solution, south segment	180.54°/80°/-10°
Fault plane solution, mid segment	210.61°/80°/-10°
Fault plane solution, north segment	173.17°/80°/-10°
Hypocenter depth	13.08 km
PGA, scenario, max	559 cm/s^2
PGV, scenario, max	40 cm/s
PGA, İzmir	103.1 cm/s^2
PGV, İzmir	5.8 cm/s
Signal duration	11 s

The parameters obtained for the earthquake scenario are given in table 5.4 and the details of the input parameters are summed up in table 4.11.

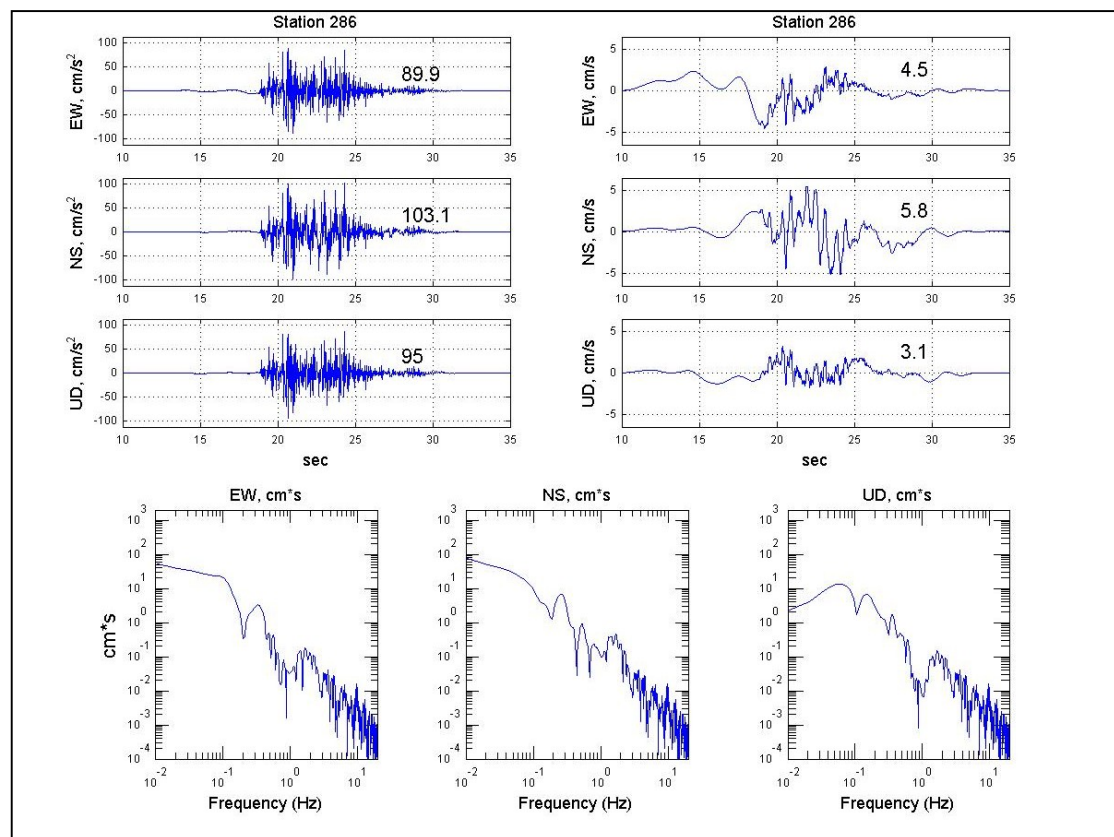


Figure 5.8: Simulated waveform for the earthquake scenario on the Gülbahçe fault. To the left the acceleration and to the right the velocity time series are shown. In the bottom of the figure the spectras for the east-west, north-south and vertical components are shown.

The seismograms and corresponding frequency spectra calculated for the earthquake scenario on the western part of the İzmir fault are shown in figure 5.8. The spectra in

the bottom of figure 5.8 reveal the significant variation for the whole frequency range (0.1-10 Hz).

The duration of the ground shaking simulated for İzmir as a consequence of the earthquake scenario on the Gülbahçe fault is found to be of 11 seconds. Because of the distant location of the Gülbahçe fault with respect to the city of İzmir, the simulated peak ground motions in the city center correspond to only 15-18% of the peak ground motions for the total earthquake scenario for both acceleration and velocity. The distance of approximately 60 km from the fault to the station ensures that the peak values of the acceleration and velocity are diminished due to attenuation.

5.3 Tuzla Fault

On the Tuzla fault ground motions were calculated for a single earthquake scenario on a 39 km long fault with a right bend in the middle. The earthquake scenario on the fault is of strike-slip mechanisms on a northeast southwest striking fault with a dip of 80° to the southeast. The earthquake scenario is described in section 4.4.3.

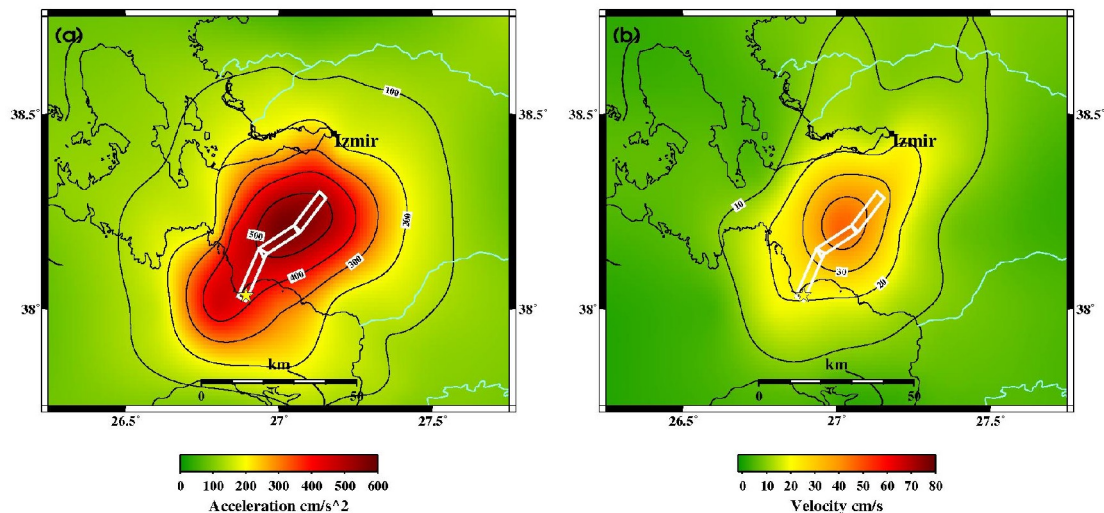


Figure 5.9: Peak ground motion distribution in the area around İzmir due to the earthquake scenario on the Tuzla fault. (a) Peak ground acceleration (cm/s^2) and (b) peak ground velocity (cm/s). The white boxes illustrate the surface projection of the fault plane segments. The yellow star shows the location of the epicenter. The city center of İzmir is given as a black dot, indicating the station for which the waveforms given below are obtained.

The peak ground motions for the earthquake scenario on the Tuzla fault are given in figure 5.9. The distribution of significant peak ground motion is divided equally on both sides of the fault for both acceleration and velocity. The pattern for the ground

motions is elongated along the fault corresponding to the geometry of the fault. The directivity effect of the ground motions is especially observed in the figure showing the peak ground velocity, where high ground motions are observed northeast of the fault (towards the city of İzmir) compared to an equal distance southwest of the fault. The strongest ground shaking is located on top of the two most northeastern segments of the fault.

Table 5.5: The primary input parameters used and output parameters obtained in the ground motion simulations for the scenario 3 TF, Tuzla Fault. The fault plane solutions are given as strike/dip/rake.

Moment magnitude, M_w	6.872
Fault plane solution, south segment	28.81°/80°/-167°
Fault plane solution, mid segment	62.56°/80°/-167°
Fault plane solution, north segment	43.57°/80°/-167°
Hypocenter depth	12.34 km
PGA, scenario, max	574 cm/s ²
PGV, scenario, max	47 cm/s
PGA, İzmir	260.0 cm/s ²
PGV, İzmir	13.6 cm/s
Signal duration	6 s

The parameters obtained for the earthquake scenario are given in table 5.5, the details of the input parameters are summed up in table 4.12.

The seismograms and corresponding frequency spectra calculated for the earthquake scenario on the western part of the İzmir fault are shown in figure 5.10. It is seen that the acceleration time series have much higher frequency content than the velocity time series, which is to be expected. The spectra in the bottom of figure 5.10 reveal the variation within the whole frequency range (0.1-10 Hz).

The duration of the signal simulated for İzmir is of 6 seconds. The ratio of the peak ground acceleration in İzmir to the peak ground acceleration for entire earthquake scenario is 0.45 and correspondingly for peak ground velocity of 29%. Because of the rupture propagation towards İzmir these ratios are much larger for the Tuzla earthquake scenario compared to the scenario earthquake on the Gülbahçe fault, even though the epicenter distance to İzmir is approximately the same in both cases.

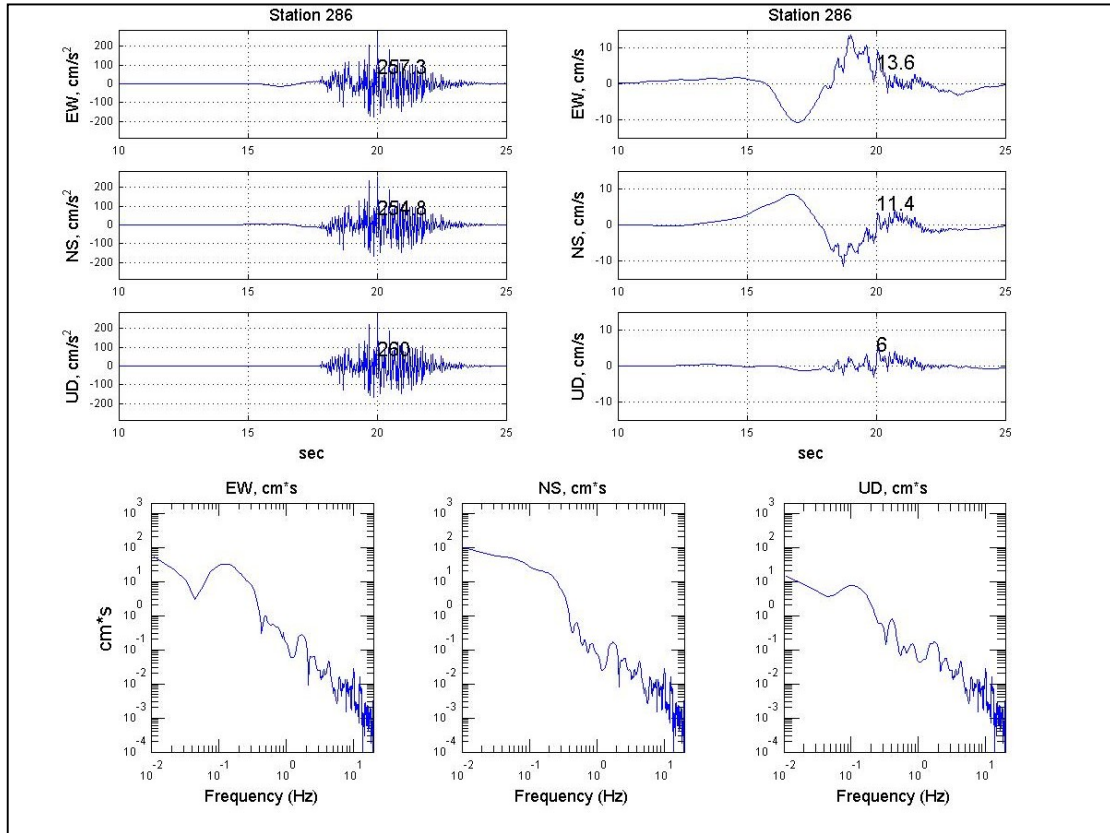


Figure 5.10: Simulated waveforms for the earthquake scenario on the Tuzla fault. The acceleration is shown on the left and the velocity on the right. In the bottom of the figure the spectras for the east-west, north-south and vertical components are shown.

5.4 Seferihisar Fault

On the Seferihisar fault ground motions were calculated for a single earthquake scenario on a 22.5 km long fault. The earthquake scenario on the fault is of strike-slip mechanisms along a north-northeast south-southwest striking fault with a dip of 80° to the southeast. The earthquake scenario is described in section 4.4.4.

The peak ground motions for the earthquake scenario on the Seferihisar fault are shown in figure 5.11. The distribution of significant ground motion is divided equally on both sides of the fault. The strongest ground shaking is located on top of the southern part of the asperity placed on the fault plane.

Table 5.6: The primary input parameters used and output parameters obtained in the ground motion simulations for the scenario 4 SF, Seferihisar Fault. The fault plane solution is given as strike/dip/rake.

Moment magnitude, M_w	6.872
Fault plane solution	$198.77^\circ/80^\circ/-149^\circ$
Hypocenter depth	12.34 km
PGA, scenario, max	574 cm/s^2
PGV, scenario, max	47 cm/s

PGA, İzmir	93.5 cm/s ²
PGV, İzmir	3.1 cm/s
Signal duration	12 s

The parameters obtained for the earthquake scenario are given in table 5.6 and the details of the input parameters are summed up in table 4.13.

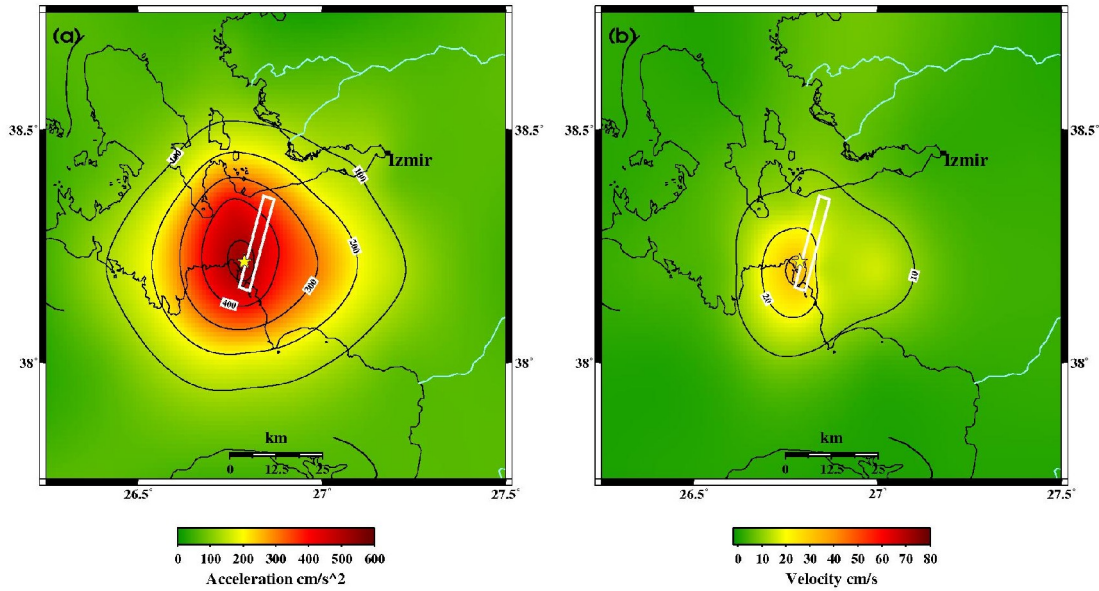


Figure 5. 11: Peak ground motion distribution in the area around İzmir due to the earthquake scenario on the Seferihisar fault. (a) Peak ground acceleration (cm/s²) and (b) peak ground velocity (cm/s). The white boxes illustrate the surface projection of the fault plane segments. The yellow star indicates the location of the epicenter. The city center of İzmir is shown as a black dot, indicating the station for which the waveforms given below are obtained.

The seismograms and corresponding frequency spectra calculated for the earthquake scenario on the western part of the İzmir fault are shown in figure 5.12. It is seen that the acceleration time series have much higher frequency content than the velocity time series, which is to be expected. The spectra in the bottom of figure 5.12 reveal the variation within the whole frequency range (0.1-10 Hz).

The duration of the seismic signal simulated for the center of İzmir is found to be 12 seconds. The peak acceleration in İzmir is found to be of only 18% of the peak ground acceleration for the entire scenario. This is explained by the location and orientation of the ruptured fault and the fact that the directivity of ground motions for this reason does not propagate towards the center of İzmir, but towards the northern side of the İzmir Bay.

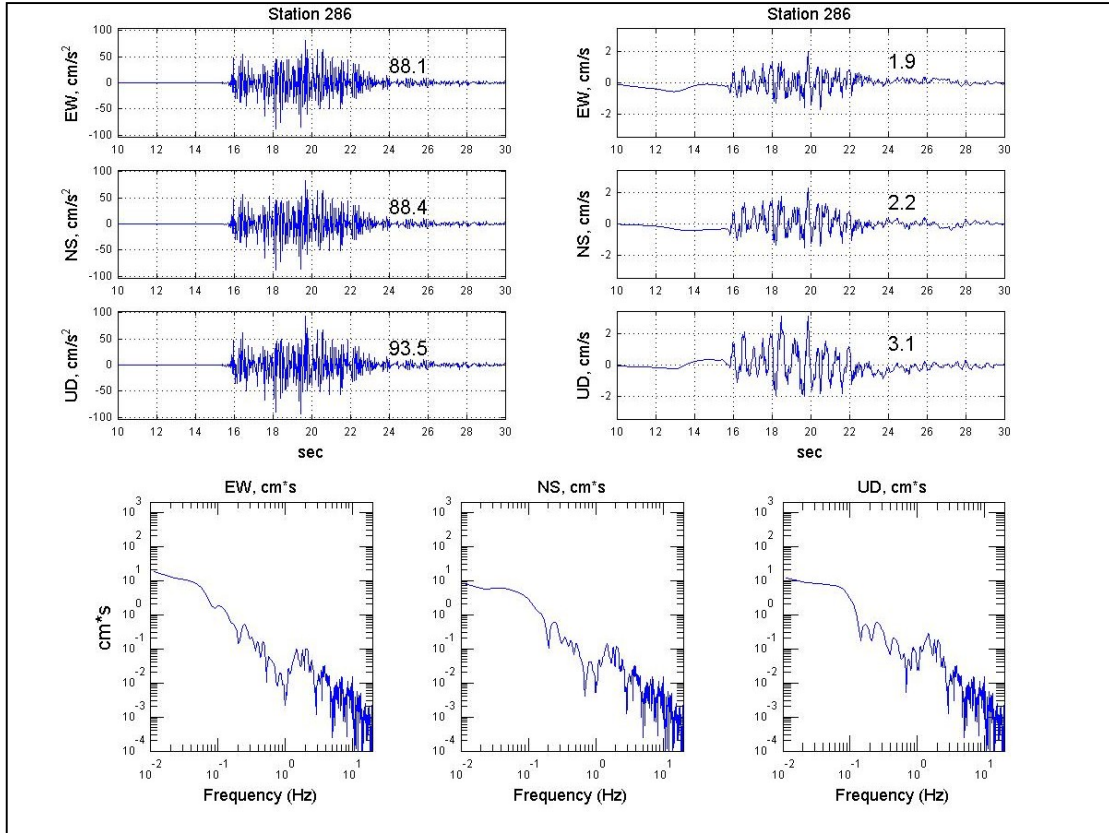


Figure 5.12: Simulated waveforms for the earthquake scenario on the Seferihisar fault. To the left the acceleration and to the right the velocity time series are shown. In the bottom of the figure the spectra for the east-west, north-south and vertical components are shown.

5.5 Manisa Fault

On the Manisa fault ground motions were calculated in three different rupture scenarios: a western, an intermediate and an eastern segment. Due to the large bend from the western to the eastern segment across the intermediate segment a combined rupture was not calculated, since the size of the bend is assumed to stop the rupture process. The earthquake scenarios on the Manisa fault are all of normal mechanisms on more or less east-west striking faults with dips of 83° to the north. The details of the earthquake scenarios are given in section 4.4.5.

5.5.1 5A WMF, Western Manisa Fault segment

The peak ground motions for the earthquake scenario on the western segment of the Manisa fault are given in figure 5.13. The largest ground motions are found above the surface projection of the asperity in the earthquake scenario. A slight directivity effect

towards west of the ground motions is observed. The distribution of significant peak ground acceleration and velocity covers the same area.

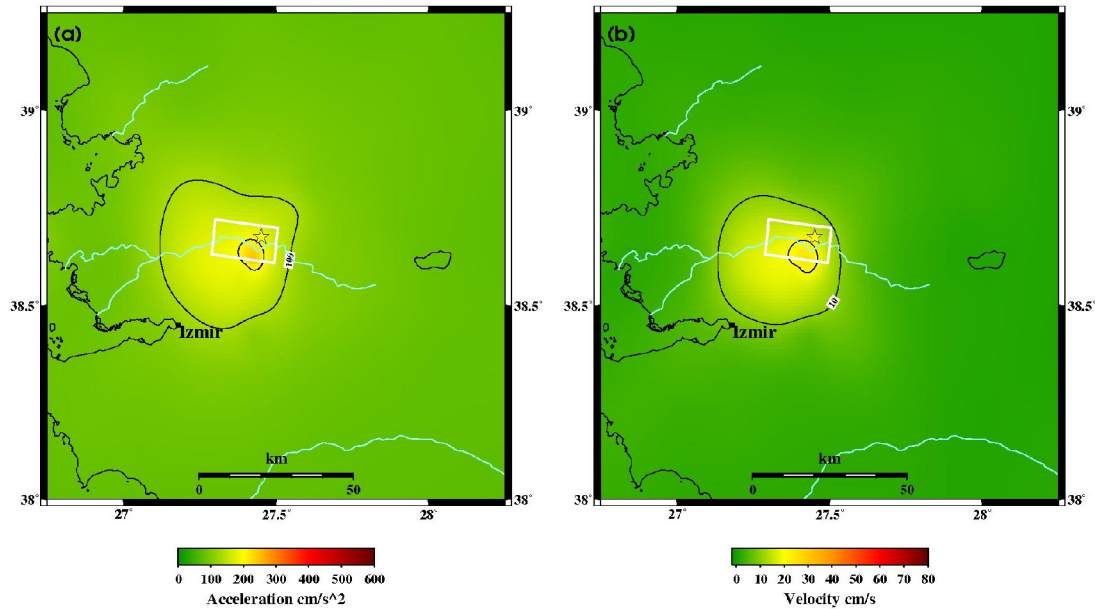


Figure 5.13: Peak ground motion distribution in the area around İzmir due to the earthquake scenario on the western segment of the Manisa fault. (a) Peak ground acceleration (cm/s^2) and (b) peak ground velocity (cm/s). The white boxes illustrate the surface projection of the fault plane segments. The yellow star shows the location of the epicenter. The city center of İzmir is given as a black dot, indicating the station for which the waveforms given below are obtained.

The parameters obtained for the earthquake scenario are given in table 5.7 and the details on the input parameters are summed up in table 4.14.

Table 5.7: The primary input parameters used and output parameters obtained in the ground motion simulations for the scenario 5A WMF, Western Manisa Fault. The fault plane solution is given as strike/dip/rake.

Moment magnitude, M_w	6.463
Fault plane solution	276.07°/48°/-83°
Hypocenter depth	9.80 km
PGA, scenario, max	255 cm/s^2
PGV, scenario, max	26 cm/s
PGA, İzmir	55.3 cm/s^2
PGV, İzmir	6.9 cm/s
Signal duration	8 s

The seismograms and corresponding frequency spectra calculated for the earthquake scenario on the western part of the İzmir fault are shown in figure 5.14. The acceleration time series have much higher frequency content than the velocity time series. The spectra in the bottom of figure 5.14 reveal the variations within the whole frequency range (0.1-10 Hz).

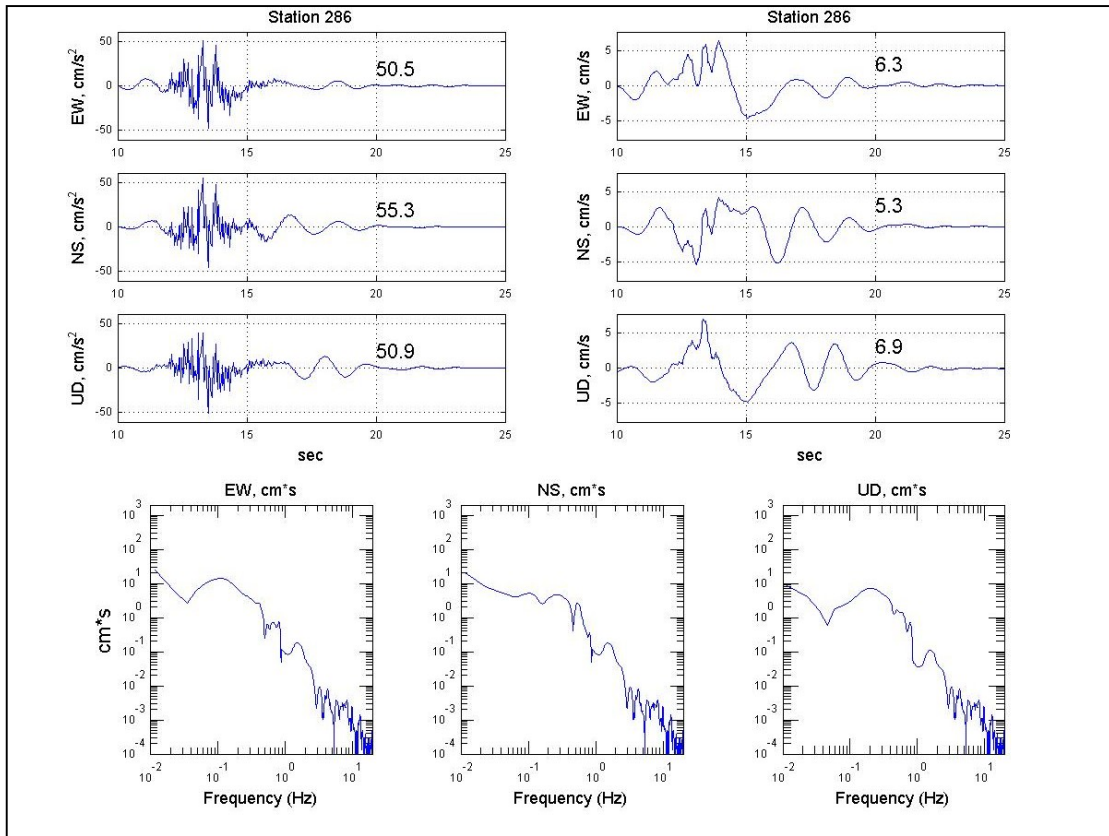


Figure 5. 14: Simulated waveforms for the earthquake scenario on the western segment of the Manisa fault. The acceleration is shown to the left and the velocity on the right. In the bottom of the figure the spectra for the east-west, north-south and vertical components are shown.

The duration of the waveforms modeled for the İzmir center is of 8 seconds. The resulting peak ground motions in the city of İzmir is of only approximately 25% of the peak ground motions for the entire earthquake scenario due to the distance between the fault and the city.

5.5.2 5B IMF, Intermediate Manisa Fault segment

The peak ground motions for the earthquake scenario on the intermediate segment of the Manisa fault are given in figure 5.15. The distribution of significant ground motions is placed equally on the hanging wall and footwall block for both the peak ground acceleration and the peak ground velocity. The largest ground motions are found above the surface projection of the fault of the earthquake scenario. A slight directivity effect of the ground motions is observed. The significant peak ground acceleration is distributed on a larger area than the significant peak ground velocity.

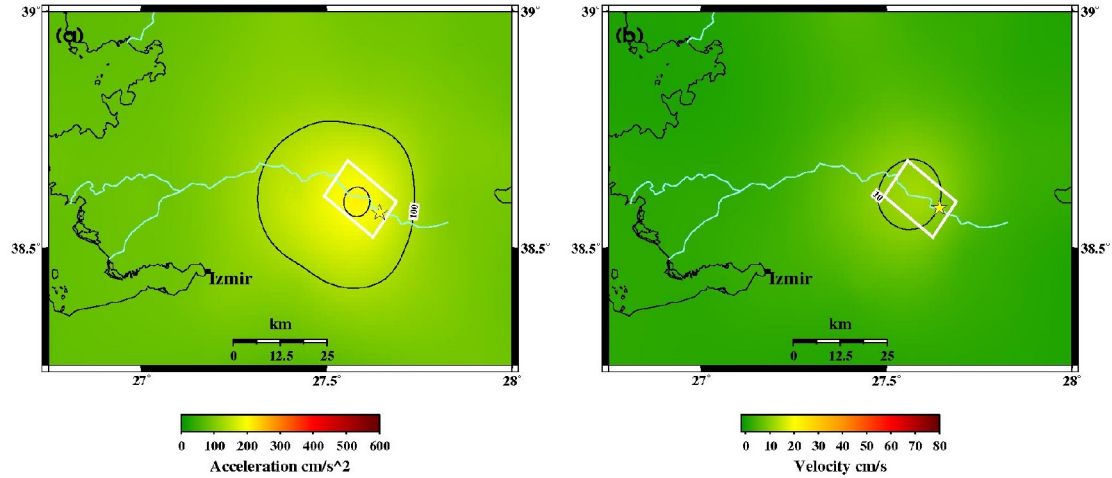


Figure 5.15: Peak ground motion distribution in the area around İzmir due to the earthquake scenario on the intermediate segment of the Manisa fault. (a) Peak ground acceleration (cm/s^2) and (b) peak ground velocity (cm/s). The white boxes illustrate the surface projection of the fault plane segments. The yellow star shows the location of the epicenter. The city center of İzmir is given as a black dot, indicating the station for which the waveforms given below are obtained

The parameters obtained for the earthquake scenario are given in table 5.8 and the details on the input parameters are summed up in table 4.15.

Table 5.8: The primary input parameters used and output parameters obtained in the ground motion simulations for the scenario 5B IMF, Intermediate Manisa Fault. The fault plane solution is given as strike/dip/rake.

Moment magnitude, M_w	6.371
Fault plane solution	303.58°/48°/-83°
Hypocenter depth	9.43 km
PGA, scenario, max	209 cm/s^2
PGV, scenario, max	12 cm/s
PGA, İzmir	35.0 cm/s^2
PGV, İzmir	2.9 cm/s
Signal duration	11 s

The seismograms and corresponding frequency spectra calculated for the earthquake scenario on the intermediate segment of the Manisa fault are shown in figure 5.16. It is seen that the acceleration time series have much higher frequency content than the velocity time series. The spectra in the bottom of figure 5.16 reveal the variation within the whole frequency range (0.1-10 Hz).

The duration of the ground shaking in İzmir due to the earthquake scenario on the intermediate segment of the Manisa fault is found to be of 11 seconds. The distance from the ruptured fault to the station in İzmir causes the seismic waves to loose energy, so the ratio of the peak ground motions in İzmir to the peak ground motions of

the earthquake scenario is of only 17% and 24% for peak ground acceleration and velocity respectively.

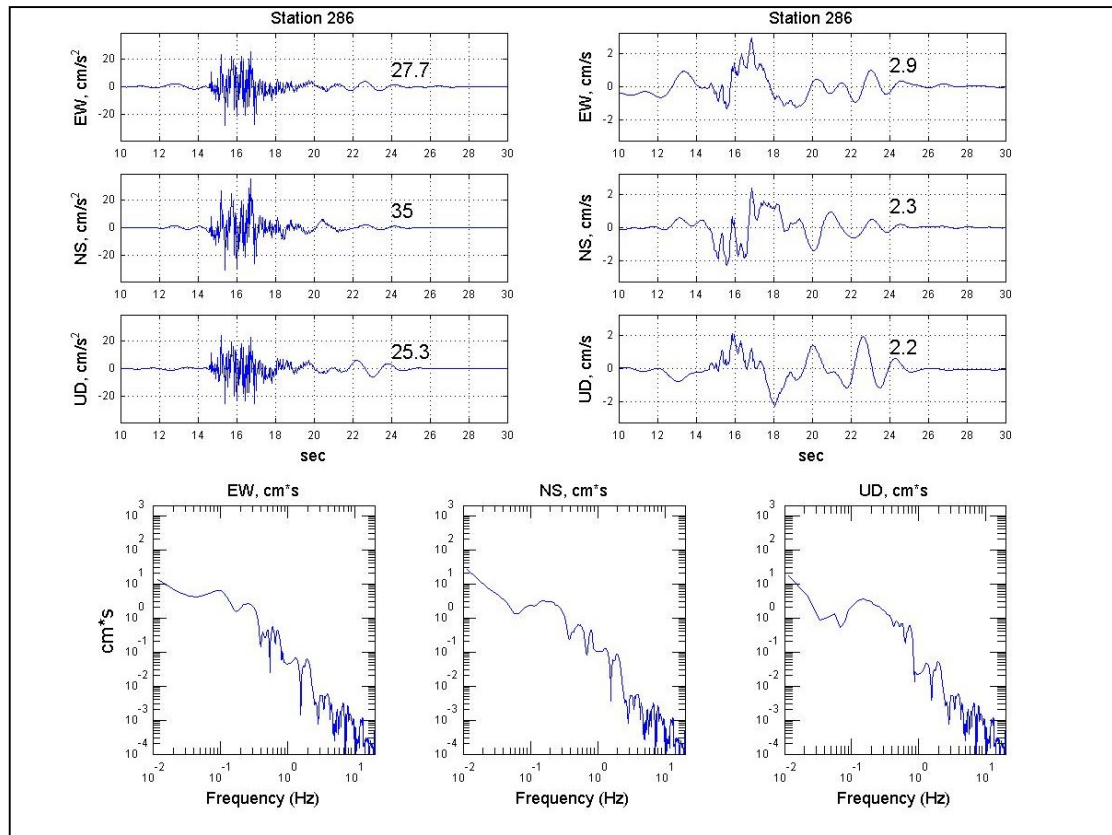


Figure 5.16: Simulated waveforms for the earthquake scenario on the intermediate segment of the Manisa fault. To the left is the acceleration and to the right the velocity time series. In the bottom of the figure the spectra for the east-west, north-south and vertical components are shown.

5.5.3 5C EMF, Eastern Manisa Fault segment

The peak ground motions for the earthquake scenario on the eastern segment of the Manisa fault are given in figure 5.17. The distribution of significant ground motions is placed equally on the hanging wall and footwall block for the peak ground acceleration, and the largest peak ground accelerations are observed above the ruptured fault plane. In the case of the peak ground velocity the ground motion distribution is more widespread. North of the fault plane an area of higher peak ground velocities than near the fault plane is observed, this might be due to a Moho reflection of the seismic waves. The magnitude of the simulated earthquake is of approximately the same size as the earthquake scenario on the eastern section of the İzmir fault (1B EIF). However, in that scenario a similar pattern was not observed. The two scenarios are of the same mechanism (normal faulting) but with different dip

(48° versus 60°), moreover the slip in the two scenarios is different (-83° versus -100°) and this might be part of the explanation of the different patterns, since the crustal model used is the same for all nine earthquake scenarios.

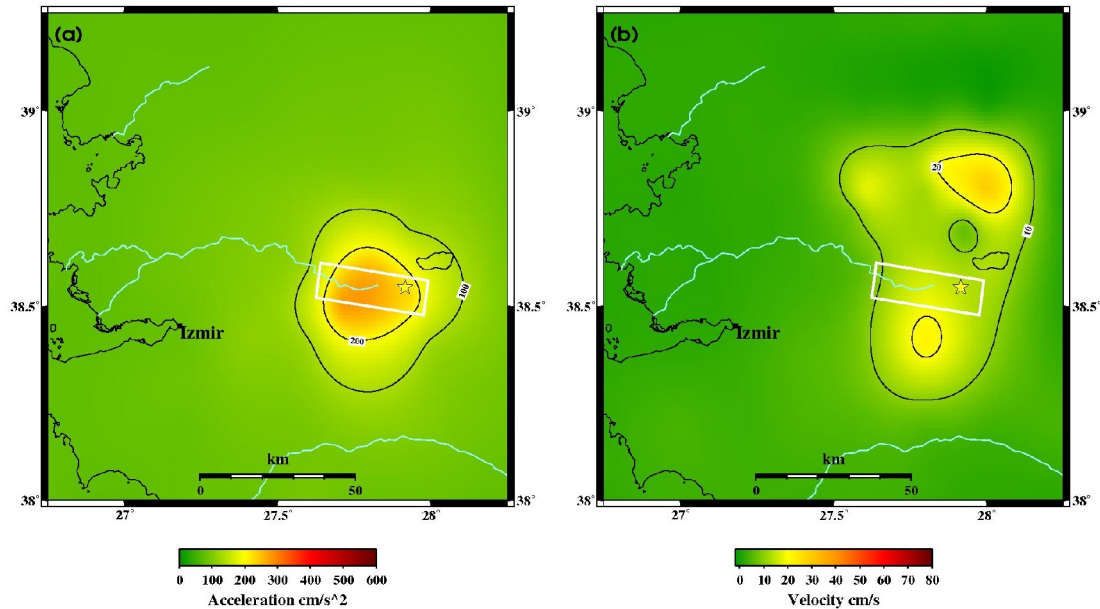


Figure 5.17: Peak ground motion distribution in the area around İzmir due to the earthquake scenario on the eastern segment of the Manisa fault. (a) Peak ground acceleration (cm/s^2) and (b) peak ground velocity (cm/s). The white boxes illustrate the surface projection of the fault plane segments. The yellow star shows the location of the epicenter. The city center of İzmir is given as a black dot, indicating the station for which the waveforms given below are obtained

The parameters obtained for the earthquake scenario is given in table 5.9, the details of the input parameters are summed up in table 4.16.

Table 5.9: The primary input parameters used and output parameters obtained in the ground motion simulations for the scenario 5C EMF, Eastern Manisa Fault. The fault plane solution is given as strike/dip/rake.

Moment magnitude, M_w	6.577
Fault plane solution	277.39°/48°/-83°
Hypocenter depth	9.99 km
PGA, scenario, max	274 cm/s^2
PGV, scenario, max	29 cm/s
PGA, İzmir	21.2 cm/s^2
PGV, İzmir	2.7 cm/s
Signal duration	11 s

The seismograms and corresponding frequency spectra calculated for the earthquake scenario on the western part of the İzmir fault are shown in figure 5.18. It is seen that the velocity time series are of much lower frequency content than the acceleration time series, which is to be expected. The spectra in the bottom of figure 5.18

reveals spectra in the bottom of figure 5.18 reveal the variation within the whole frequency range (0.1-10 Hz).

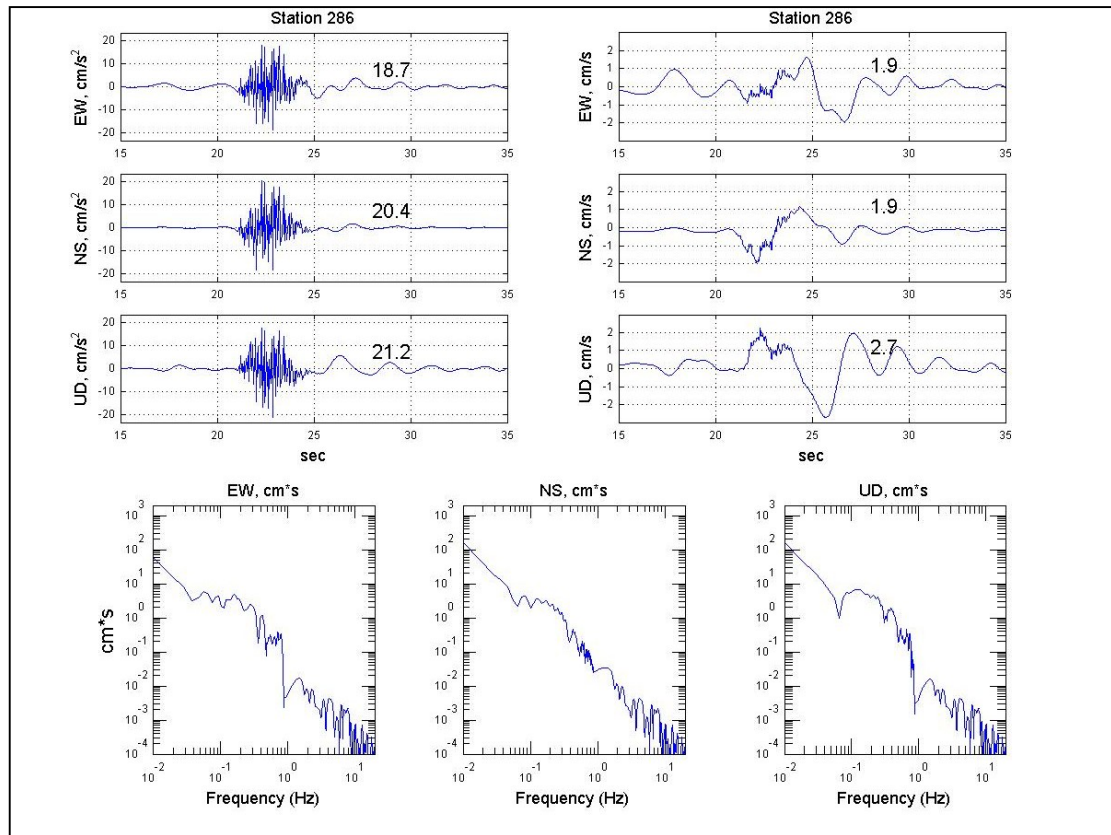


Figure 5.18: Simulated waveforms for the earthquake scenario on the eastern segment of the Manisa fault. The acceleration is shown on the left and the velocity on the right. In the bottom of the figure the spectra for the east-west, north-south and vertical components are shown.

The duration of the simulated ground motions in İzmir for this earthquake scenario is found to be 11 seconds. The ratios of peak ground motion in the center of İzmir to the peak ground motions of the earthquake scenario are of 8% and 9% for acceleration and velocity respectively.

The three earthquake scenarios simulated for the Manisa fault all cause very low ground motions in the city of İzmir, and a rupture on the Manisa fault is therefore expected to have the least impact on the city of İzmir compared to the other earthquake scenarios presented in this thesis.

6 Discussion

In this study ground motion simulations were conducted for nine different earthquake scenarios on faults located in the vicinity of İzmir (Emre et al., 2005b). The results obtained from the ground motion simulations were presented for each single fault in the previous chapter. In the first section of this chapter they are compared followed by discussions on site effect problems in the city of İzmir. In the last section of this chapter a short discussion is given about the weaknesses in ground motion simulation methodology.

In appendix G and H all the comparisons of empirical attenuation relations with the ones obtained during this study are made for the peak ground motions and velocity response spectra for various locations placed close to faults are shown.

6.1 Discussion of the obtained results

The attenuation of peak ground motions for all the scenario earthquakes are compared with existing empirical attenuation relations, local as well as world-wide. In addition, frequency response spectra are presented for the earthquake scenarios, which are discussed in section 6.1.3. These spectra are compared to the H/V spectra obtained in a previous study (Atakan, 2005) in section 6.2.1.

6.1.1 Comparison of the results

In order to determine the worst-case scenario for the city of İzmir the peak ground motion values for all scenarios have been plotted as a function of the signal duration for a site located in the center of İzmir (figure 6.1). These results are also shown in table 6.1.

Table 6.1: Signal duration and peak ground acceleration and velocity obtained at the station located in the İzmir center for the nine different earthquake scenarios conducted in this study. Scenario 1C IF results in the largest ground motions in İzmir and is highlighted in bold types.

Scenario		Duration (s)	PGA, İzmir (cm/s ²)	PGV, İzmir (cm/s)
1A WIF	Western İzmir segment	5	150,9	10,3
1B EIF	Eastern İzmir segment	7	226,6	23,5
1C IF	İzmir Fault	9	291,4	47,6
2 GF	Gülbahçe Fault	11	103,1	5,8
3 TF	Tuzla Fault	6	260,0	13,6
4 SF	Seferihisar Fault	12	93,5	3,1
5A WMF	Western Manisa segment	8	55,3	6,9
5B IMF	Intermediate Manisa segment	11	35,0	2,9
5C EMF	Eastern Manisa segment	11	21,2	2,7

Figure 6.1 clearly shows the worst-case scenario for the city of İzmir, i.e. the scenario 1C IF, where the entire İzmir Fault ruptures. Also the scenario on the easternmost segment of the İzmir fault (1B EIF) is considered critical for İzmir.

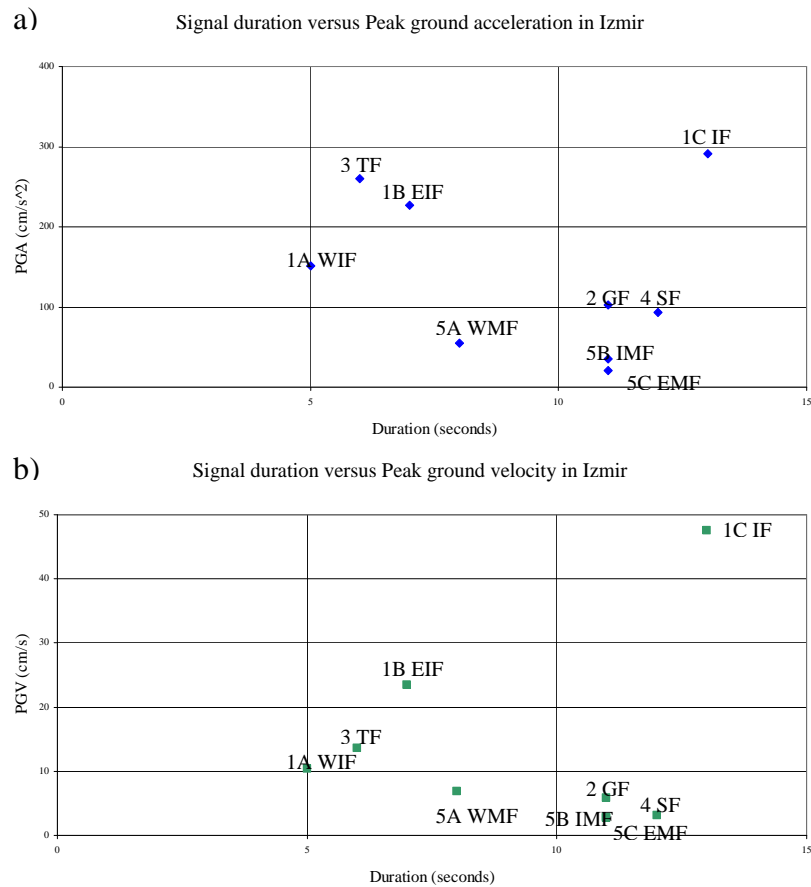


Figure 6.1: Peak ground motions obtained for the nine earthquake scenarios plotted as a function of the signal duration for a site in the center of İzmir. The earthquake scenarios are identified with their respective abbreviated codes (see table 6.1).

The scenario earthquake 1C IF is found to be the worst-case scenario, since the peak ground motions for this event are much higher compared with the signal duration of the other scenarios. The signal duration for this scenario is 13 seconds, which is the longest signal duration obtained in this study. The highest peak ground acceleration and velocity of 291.4 cm/s² and 46.7 cm/s respectively for the same scenario is much higher than predicted by the general tendency of longer signal duration which is consistent with lower peak ground motions, see also figure 3.2 (section 3.1.1). This tendency is observed for both the peak ground accelerations and velocities.

Obviously the high values of peak ground motions observed in İzmir for scenario 1B EIF and 1C IF are partly explained of the proximity of the site to the scenario faults. In such cases the effect of attenuation is at minimum. This is also evident since the ratio between the peak ground acceleration obtained in İzmir and the one obtained from the entire scenario, for both cases is of more than 70%, see section 5.1.

Comparing the moment magnitudes for the simulated earthquake scenarios with the maximum obtained peak ground motions in the scenarios reveals that ground motions resulting from strike-slip faults are higher than those from normal faults, which has also been discussed in previous studies (Brune and Anooshehpour, 1999; McGarr, 1984; Oglesby et al., 1998; Shi et al., 2003). The predicted peak ground acceleration regarding the three earthquake scenarios on strike-slip faults are all higher than those predicted for the normal faulting events, even though the normal faulting scenarios on the combined İzmir fault (1C IF) is the second largest scenario when considering the energy and moment magnitudes. These are shown in table 6.2.

Table 6.2: Moment magnitudes for the nine earthquake scenarios and corresponding peak ground motions for the scenarios. The largest moment magnitude used and the largest peak ground motions obtained are written in bold types.

Scenario		M _w	PGA cm/s ²	PGV (cm/s)
1A WIF	Western İzmir segment	6.463	256	35
1B EIF	Eastern İzmir segment	6.542	262	28
1C IF	<i>İzmir Fault</i>	6.886	438	68
2 GF	Gülbahçe Fault	6.939	559	40
3 TF	Tuzla Fault	6.872	574	47
4 SF	Seferihisar Fault	6.617	526	32
5A WMF	Western Manisa segment	6.463	255	26
5B IMF	Intermediate Manisa segment	6.371	209	12
5C EMF	Eastern Manisa segment	6.577	274	29

Larger ground motions are observed in the scenario for the Tuzla fault compared to the Gülbahçe fault, even though the moment magnitude is set to be larger in the later scenario because of the assumed longer fault length. Furthermore, the normal component of both scenarios is approximately the same (-10° and -167° respectively). However, the larger ground motions observed from the earthquake scenario on the Tuzla fault can be a result of variations in the location of asperities on the two faults. In the case of the Gülbahçe fault two asperities are used in the two end segments of the fault. In the scenario earthquake for the Tuzla fault three asperities are used – one on each fault segment.

6.1.2 Attenuation of the seismic waves

In chapter 4.1 the velocity model was chosen and the attenuation relation used in the ground motion simulations was mentioned. In order to check if these values are reasonable, the simulated peak ground acceleration (PGA) and peak ground motion (PGV) values are compared to the ground motion with empirically obtained attenuation relations for distances up to 400 km from the fault.

The simulation results are compared with five different empirical attenuation relations for PGAs: Ambraseys et al. (1996), Campbell (1997), Gülkan and Kalkan (2002), Spudich et al. (1997) and Pankow and Pechmann (2004). The simulated PGVs are compared to four different empirical attenuation relations, being Campbell (1997), Akkar and Bommer (2007) and two results from Pankow and Pechmann (2004). All empirical relations are set up with hard rock conditions, since ground motions were simulated for the bedrock.

The attenuation relation of Ambraseys et al. (1996) concerns hard rock condition in Europe. The relation used is for PGAs with a structural period of 1 Hz.

The attenuation relation from Campbell (1997) is for horizontal peak ground motion values, and the relation is especially developed in order to predict near-source ground motion in the region of moderate to large earthquakes. In this study the peak ground motion values used is a geometric mean of the two horizontal components, and the

distance from fault to station is the shortest distance between the recording site and the presumed zone of seismogenic rupture on the fault. In the study by Campbell (1997) attenuation relations are developed for strike-slip and reverse faults, since the database used contains only two normal fault events. The database used is world-wide (Campbell, 1997). Therefore, when comparing the empirical relation with the simulated peak ground motions the relation for strike-slip faults is used. It is for the discussion kept in mind that strike-slip faults are assumed to produce higher ground motions than normal faults (McGarr, 1984).

Gülkan and Kalkan (2002) used 47 strong ground motion records from earthquakes in Turkey in order to predict free field horizontal components for PGA. They have produced attenuation relations valid for distances up to 150 km from the fault, and they define the distance as the shortest horizontal distance from the recording site to the horizontal projection of the rupture zone to the surface. The relation is developed for a single fault category, since the peak ground motions for the normal and reverse faulting earthquakes in the database did not show significant difference from ground motion characteristics of strike-slip earthquakes (Gülkan and Kalkan, 2002).

The empirical attenuation relation by Spudich et al. (1997) was conducted for world-wide PGAs in extensional regimes, being identified as areas where there is a mixture of normal and strike-slip faulting, recent volcanism, lithospheric thinning and a high heat flow. The study area of this thesis fits with these characteristics. The relations obtained from this study are for horizontal peak acceleration from earthquakes in the magnitude range of 5.0 to 7.7 and in the distance range of 0-70 km from the fault. The distance from the recording site to the fault is defined similar to the study by Gülkan and Kalkan (2002) as the shortest horizontal distance from the station to the horizontal projection of the rupture zone to the surface (Spudich et al., 1997).

Pankow and Pechmann (2004) made a modification to the study conducted by Spudich et al. (1996). The distance from fault to recording site is therefore defined similar. The study by Pankow and Pechmann (2004) further extended the previous study by developing empirical relations for obtaining the attenuation relations for PGVs. Furthermore, an alternative to the PGV relation was developed by using an empirical relation between PGV and 5% damped pseudovelocity at 1 Hz from

Newmark and Hall (1982). The two empirical relations obtained for peak ground motions results in different PGV values for short distances to the fault, but yield the same values for distances of more than 300 kilometers (Pankow and Pechmann, 2004).

In the study by Akkar and Bommer (2007) an empirical attenuation relation for PGV is developed based on 532 strong ground motion records from Europe and the Middle East at distances up to 100 km from 131 earthquakes in the moment magnitude range of 5-7.6. The study presents empirical relations for the attenuation of PGV both as the geometrical mean of the two horizontal components, but also for the maximum value of the horizontal component. It is the latter relation, which is used in the comparison with the simulated results from this study. The distance is defined as the minimum horizontal distance from the surface projection of the fault rupture to the recording station (Akkar and Bommer, 2007).

The comparison of simulated peak ground motions as a function of distance with the empirical relations has been done for the nine earthquake scenarios. However, only the graphs for scenario 1C IF and 3 TF are shown in this section and the reader is referred to appendix G for comparison with all other scenarios. Scenario 1C IF and 3 TF are chosen since they represent a normal fault and a strike-slip fault respectively and at the same time they are also representing the worst-case scenarios for the city of İzmir, as found in section 6.1.1. The distance used for the simulation points are the shortest distance from recording site to the fault rupture in three dimensions. This is not the same as used in the empirical relations, since they use the shortest horizontal distance from the recording site to the fault rupture, however, in all the empirical relations an artificial depth is used, and it was found more correct to use the actual shortest distance to the fault rupture. It is not expected that this will change the results significantly. Moreover the output from the ground motion simulations gives the maximum horizontal peak ground motion, and there is therefore not used a geometric mean of the two horizontal components in the comparisons, like it is done for most of the empirical relations.

Figure 6.2 shows the comparison of simulated ground motions, PGA and PGV at distances less than 400 kilometers to the fault for the rupture on the İzmir fault,

scenario 1C IF. As seen from the figure there is reasonably good agreement between the simulated ground motions and empirical predictions. There is a tendency for the PGA that the simulated values are below the attenuation curves. However, the pattern of the simulated PGA values fit best to the one of the empirical relations given by Campbell (1997). Also since the relation given by Campbell (1997) is for strike-slip faults, the ground motion is assumed to be lower in the case of scenario 1C IF, since this a normal faulting earthquake. However, the empirical relation by Spudich et al. (1997) yields higher ground motions than the study by Campbell (1997), even though this is derived for extensional regimes. In the case of the peak ground velocities, the simulated values have a larger spread but they lie between the values predicted by the upper and lower limits of the empirical attenuation relations.

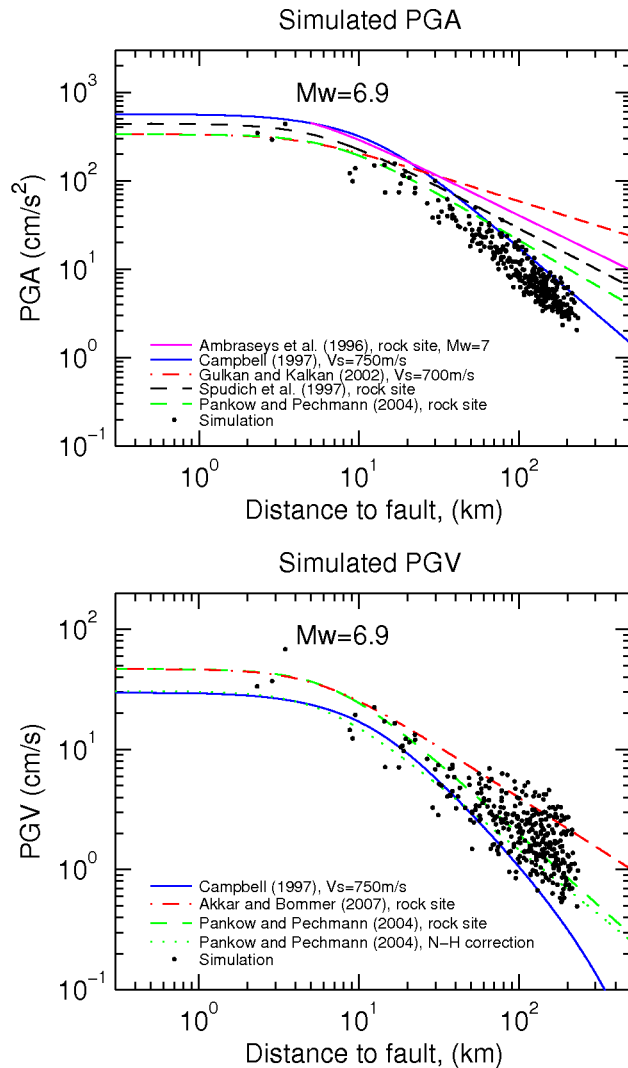


Figure 6.2: Comparison of simulated (black dots) peak ground acceleration (top) and velocity (bottom) to ground motions predicted by empirical attenuation relations of Ambraseys et al. (1996), Campbell (1997), Gülkan and Kalkan (2002), Spudich et al. (1997), Akkar and Bommer and Pankow and Pechmann (2004). For the last relation there is in the case of PGV also shown a corrected version by applying the results of Newmark and Hall (1982) for PGV. The comparison is done with the results obtained for the earthquake scenario 1C IF, İzmir fault.

In figure 6.3 the comparison of simulated ground motions, PGA and PGV are shown at distances less than 400 kilometers to the fault for the rupture on the Tuzla fault, scenario 3 TF. It is seen that the simulated values for the PGA fits better to the

predicted empirical attenuation relations. Though for distances of less than 30 kilometers to the fault the PGA are higher than the attenuation relations predicts. For the PGV, as for the case of the earthquake scenario 1C IF, the simulated values are between those predicted by the empirical relations, though there is a tendency of the simulated PGV values to be in the higher range of the of the empirical relations, especially at larger distances. This can partly be explained by the directivity of the ground velocity observed for scenario 3 TF on Tuzla fault (figure 5.9).

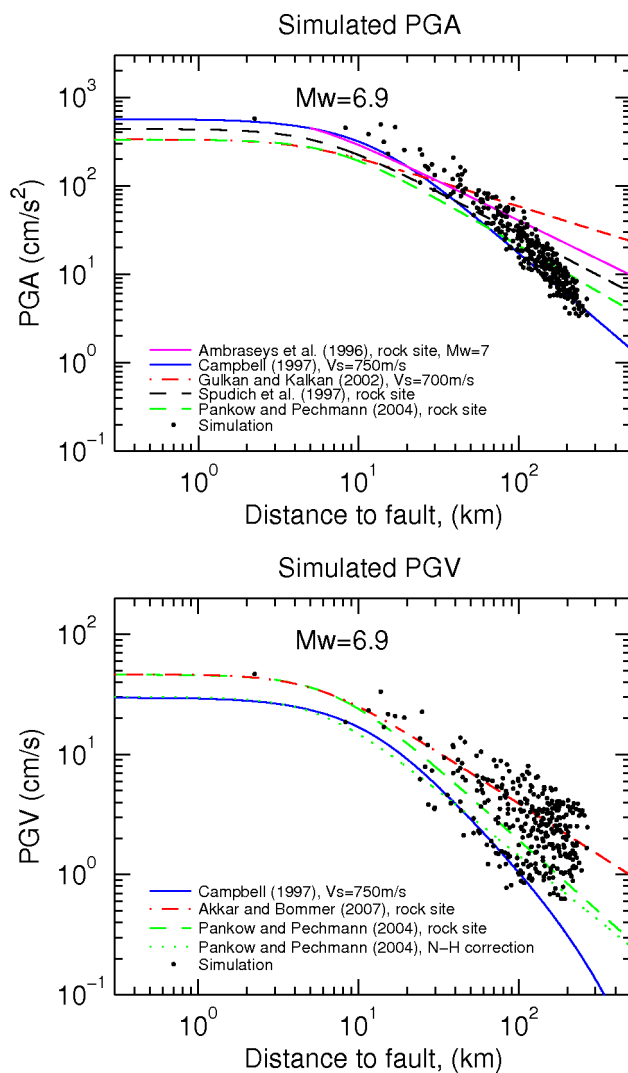


Figure 6.3: Comparison of simulated (black dots) peak ground acceleration (top) and velocity (bottom) to ground motions predicted by empirical attenuation relations of Ambraseys et al. (1996), Campbell (1997), Gülkan and Kalkan (2002), Spudich et al. (1997), Akkar and Bommer and Pankow and Pechmann (2004). For the last relation there is in the case of PGV also shown a corrected version by applying the results of Newmark and Hall (1982) for PGV. The comparison is done with the results obtained for the earthquake scenario 3 TF, Tuzla fault.

There seems to be a reasonably good agreement between the simulated ground motions and empirical predictions.

For the obtained simulated values from earthquake scenarios on normal faults, scenario 1A-C IF and 5A-C MF (figure G.1-3 and G.7-9 in appendix G) yields lower simulated PGA values than the empirical relations, but the distribution of the simulated points follows the shape of the relation given by Campbell (1997).

For the PGV, the simulated values are found to be in between the range of the predictive relations; however, there are observed lower ground motions than predicted for shorter distances. That the

simulated ground motions tends to be lower than the predictive relations, is in agreement with the fact that normal faults produce lower ground motions than strike-slip faults, since the relations used primarily are found from strike-slip faulting earthquakes.

In the case of the simulated peak ground motions from the earthquake scenarios on strike-slip faults, scenario 2-4 (figure G.4-6 in appendix G) the simulated PGA values fits very well to the predicted empirical relations, but there is observed larger values for shorter distance than the relations predict. For the peak ground velocities the majority of the simulated values are in the range between the different empirical predicted relations, however, for both the scenario on the Gülbahçe and the Tuzla fault, scenarios 2 GF and 3 TF respectively, there is also observed a cloud of larger PGV values for the whole distance range. This can be explained by the effect of rupture directivity, which is especially pronounced in these two scenarios, as was seen in the figures showing the peak ground velocities for these scenarios (figure 5.7 and 5.9).

The figure showing the comparison of the simulated values from the earthquake scenario on the Seferihisar fault (4 SF) with the empirical relations (figure G.6) reveals a cloud of points for the PGA values with lower values than the predicted in the distance range of 20 to 200 kilometers, though the majority of the points are in agreement with the predictive relations. As the PGV values are concerned lower ground motion values are observed in the whole distance range, though the majority of the points are also within the range of the predictive relations.

The empirical relation for PGA derived for Turkey (Gülkan and Kalkan, 2002) yields the largest ground motions of the predictive attenuation relations, and therefore the ones least fitting to the obtained values for the PGA, especially for the normal faulting scenarios and on larger distances for the scenarios on strike-slip faults. The study predicting peak ground velocities for Europe and the Middle East (Akkar and Bommer, 2007) serve as an upper bound for obtained values as far as the normal faulting events are concerned.

The empirical relation derived by Campbell (1997) for a worldwide dataset of mainly strike-slip faulting earthquakes agrees best with the simulated data in the case of predicting PGA. The simulated PGV agrees best with the empirical relations derived by Pankow and Pechmann (2004) for the normal faulting events. For the Gülbahçe and Tuzla faults the simulated PGV values fit either with the relations by Pankow and Pechmann (2004) or the empirical relation obtained by Akkar and Bommer (2007) for Europe and the Middle East.

6.1.3 Response spectra

The velocity response spectra for the nine scenario earthquakes at the station in İzmir center are shown in figure 6.4. For all scenarios, except those on the different fault segments of the İzmir fault, very low spectral velocity values are seen, with no major peaks. There are however, minor peaks on the spectra from the earthquake scenario 3 TF on Tuzla Fault (green) for frequencies between 0.1 to 0.4 Hz on both horizontal components. The absolute spectral velocity values, on the other hand,

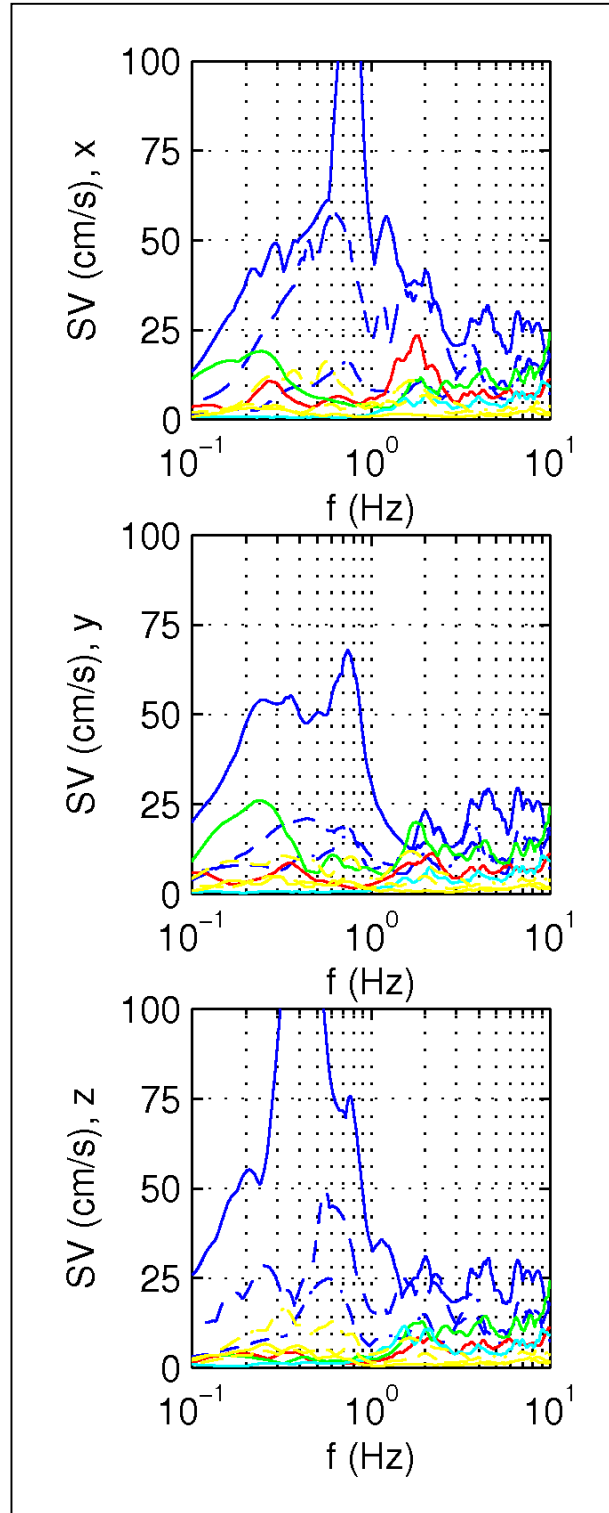


Figure 6.4: Comparison of the velocity response spectra for all nine scenarios. Scenario 1A-C (blue), where 1A (-.-), 1B (-) and 1C (a connected line). 2 GF (red), 3 TF (green), 4 SF (light blue), 5A-C (yellow), where 5A (-.-), 5B(-) and 5C (a connected line). The horizontal components are gives as x for east-west and y for north-south, z is the vertical component.

are only in the range of 25 cm/s in these peaks. Also the scenario earthquake 2 GF on the Gülbahçe Fault (red) produces a small peak in the east-west direction (x) for frequencies of 1-2 Hz.

The dominating earthquake scenarios in figure 6.4 are those simulated on the different İzmir fault segments (blue). Especially for the scenarios 1B EIF (--) and 1C IF (-) strong peaks are observed in the frequency range of 0.2 to 1 Hz. The peaks are strongest for scenario 1C IF, on the combined rupture of the western and eastern segments, while they are weakest for the westernmost segment.

The peaks on the vertical component for scenario 1A-C IF indicate a vertical displacement during the rupture in agreement with the normal faulting mechanisms of these scenarios. It is also seen that the velocity response for the Manisa fault scenarios (5A-C MF) have the strongest peaks in the vertical component, whereas the velocity response for the scenario earthquakes conducted for strike-slip faults (scenario 2-4) is flat for the lower frequency range on the vertical component of the velocity response.

In a previous study (Durukal et al., 2006) the different codes of ground motion simulation are compared to each other. This comparison shows a large variation in the ground motion estimates in all the codes close to the fault, whereas further away the results converge to homogeneous distribution. In this respect, the very high peaks observed in the velocity response spectra, for especially the earthquake scenario 1C IF, could be attributed to this near fault variation. In order to check this, velocity response spectra are made for simulation points in approximately equal short distance (as is the case for the İzmir fault) to four of the other earthquake scenarios (2 GF, 3 TF, 4 SF and 5A WMF). These are shown in appendix H. No significant peaks are observed in these trials. The strong peaks in figure 6.4 can then be attributed to near-fault variations due to specific input parameters used in this scenario for the İzmir fault.

According to the descriptions of the historic earthquakes the city has been destroyed several times by earthquakes with $M_w > 6.0$ (section 2.2). In order to constrain these events better, new ground motion simulations need to be performed on fault segments on both the İzmir and the Tuzla faults with corresponding magnitudes of historical

events. Correlation with the damage due to these historical events is then possible. In this thesis the main focus has been to identify the most critical faults that control the earthquake hazard in İzmir. Therefore simulating historical events is beyond the scope of this thesis.

6.2 Local site conditions and secondary effects of earthquakes

In this thesis all ground motion simulations are conducted for bedrock conditions and hence the possible local site effects are not taken into account. In this section local site effects in İzmir are discussed based on previous work.

Due to the north-south extension in western Anatolia large graben structures are developed. The origin of the İzmir bay is associated with similar extensional tectonics and results in basin development in time. The current morphology in the area clearly indicates two distinct features. The areas located topographically high are associated with the bedrock outcrops whereas the low-lying areas represent the accumulated sedimentary deposits. The large part of the metropolitan area of İzmir is situated on such sedimentary deposits. Furthermore, the significant fluvial deposition occurs in the delta of the Gediz River in the northern part of the İzmir Bay (Karşıyaka) and from smaller secondary rivers in the eastern and southern part of the city. In addition to that fast development of the metropolitan area has engendered several artificially filled coastal areas such as the coastal strip along the southern part (Kordon) and the northern part (Karşıyaka) of the bay.

6.2.1 Amplification of seismic waves

General geotechnical characteristics of the İzmir metropolitan area was mapped within the framework of the İzmir Earthquake Master Plan (Erdik et al., 2000). Soil classifications were made based on the Turkish earthquake resistant design code (Aydinoglu, 1998) and is shown in figure 6.5.

Table 6.3: Soil classification from the study of Aydinoglu (1998).

Soil condition	Characteristic period A	Characteristic period B
Z1	0.10	0.30
Z2	0.15	0.40
Z3	0.15	0.60
Z4	0.20	0.90

The four classifications shown in figure 6.5 (Z1-Z4), are based on the geotechnical data from boreholes and CPT measurements on 98 sites using the recommendations in the study by Aydinoglu (1998), see table 6.3. As it is seen in figure 6.5 the red and blue areas, corresponding to softer soil conditions (Z3 and Z4), cover most of the northern part as well as the coastal area around the bay.

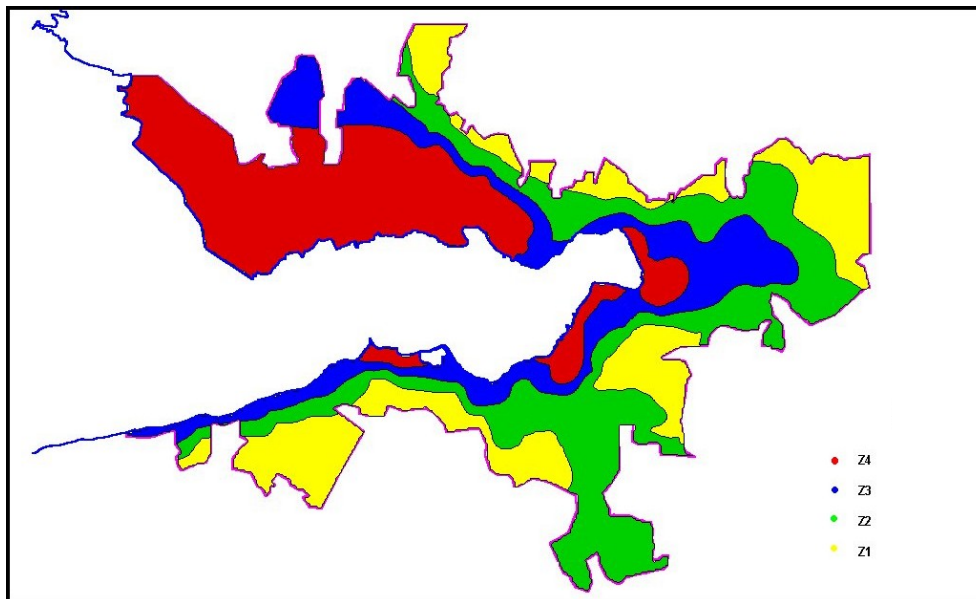


Figure 6.5: Soil classification in the area surrounding the İzmir bay. Colour-codes correspond to the soil conditions given in table 6.3. The original figure has no geographical reference points; however, the coloured area corresponds to the limits of the metropolitan area of İzmir.

The amplification of seismic waves due to the unconsolidated sediments in İzmir was estimated in the İzmir Earthquake Master plan, as shown in figure 6.6. In general significant amplification is expected at the northern side of the bay area. Furthermore, the city center is expected to experience an amplification factor of three.

This is further confirmed by an independent preliminary study conducted on two sites in the northern (Karşıyaka) and the southern part of the bay (Kordon) (Atakan, 2005). This study is based on H/V spectral ratios computed on ambient noise records (Nakamura, 1989), following the guidelines suggested by the SESAME project

(Atakan et al., 2004a; Atakan et al., 2004b; Koller et al., 2004). The H/V spectral ratios obtained are usual able to estimate the fundamental frequency for a given site.

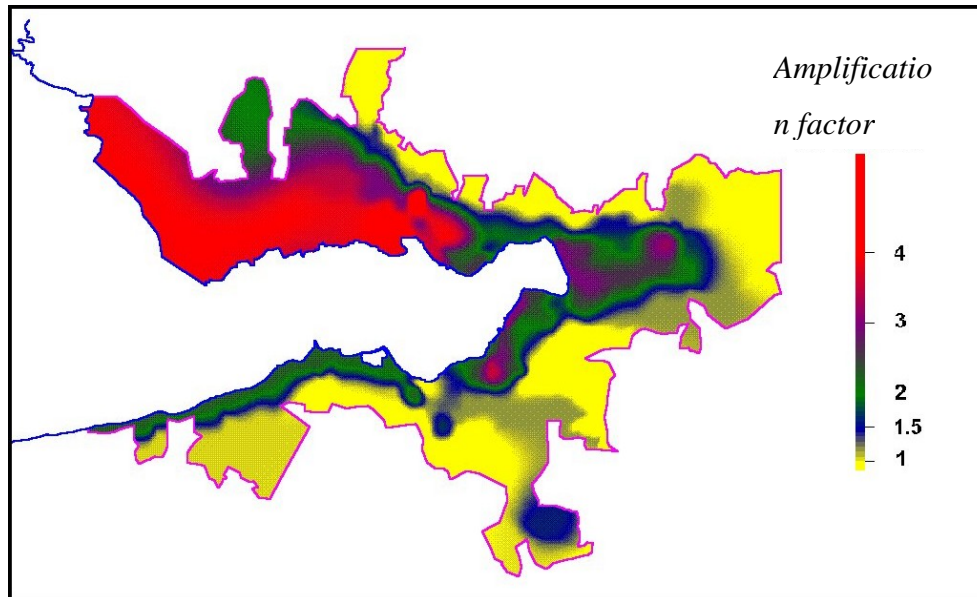


Figure 6.6: Amplification factors for ground motion modeling conducted on a bedrock site. The map is conducted as a part of the İzmir Earthquake Master Plan (Erdik et al., 2000). The original figure have no geographical reference points; however, the coloured area corresponds to the limits of the metropolitan area of İzmir.

The fundamental frequency is the frequency at which the strongest amplification of ground motions occurs due to local site effects and is therefore the most important frequency seen from a hazard perspective. Although the method is effective in assessing the fundamental frequency, the amplification factors are not reliable.

Comparing the fundamental frequency range found in the study of Atakan (2005) (figure 6.7) with the frequencies where peaks are observed in the response spectra (figure 6.4) from the earthquake scenarios on the İzmir fault from this study, leads to the evident conclusion that there is an overlap in the frequency range. The modeled ground motions are thus expected to amplify significantly in this frequency range.

Within the framework of the İzmir Earthquake Master Plan (Erdik et al., 2000), described in section 2.3.2, a map showing the liquefaction potential was prepared. It is from figure 6.8 evident that especially the center of İzmir and the northern side of the bay, Karşıyaka, are considered to be especially prone to liquefaction processes, whereas to the south and the east these processes are considered to be of less importance. The red area in the north coincides with the delta of the Gediz River.

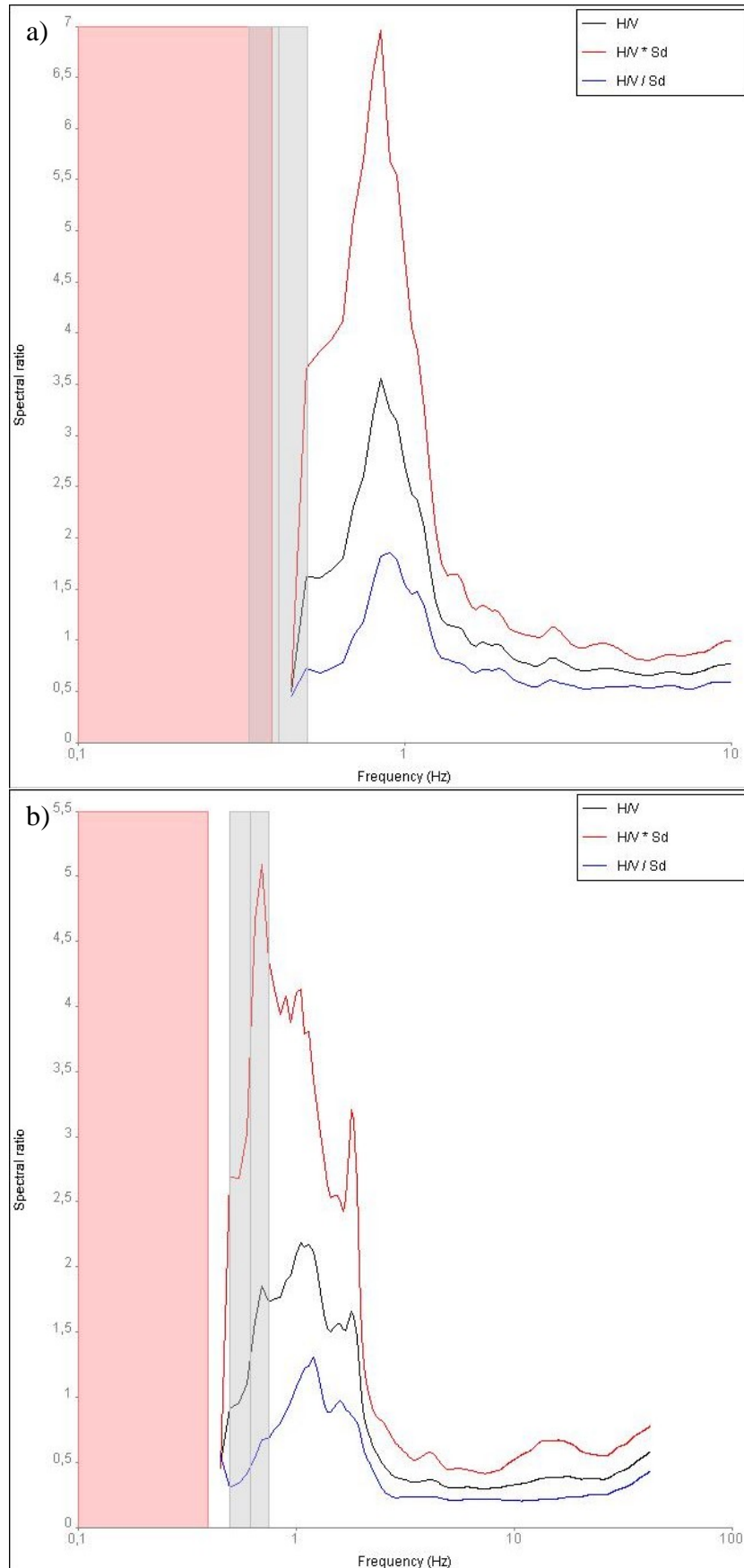


Figure 6.7: Site response spectra for **a)** Kordon and **b)** Karşıyaka. There are in both spectra observed broad peaks around the frequency of 1 Hz (approximately in the range of 0.4 to 1.4 Hz), suggesting the frequency to be the fundamental frequency for these two sites. (Note different x- and y-scales).

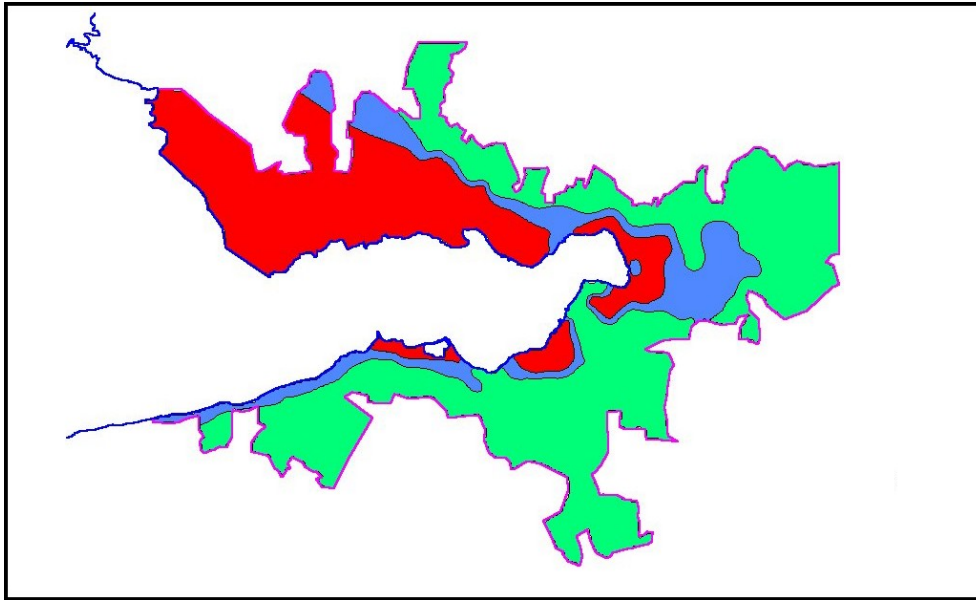


Figure 6.8: Contour map showing the liquefaction potential in the area surrounding the İzmir bay. Color-codes yield red for high, blue for intermediate and green for low potential of liquefaction (Erdik et al., 2000). The original figure does not have geographical reference points; however, the coloured area corresponds to the limits of the metropolitan area of İzmir.

Both Kordon and Karşıyaka are located on artificial filling. As far as Kordon is concerned the filling consists of large blocks with gravel in between. On the northern side of the bay in Karşıyaka it is not clear how the filling has been conducted. However, the field trip in the area in autumn 2006 showed that the houses build in this area are subsiding into a soft fundament, resulting in tilted houses. This is illustrated in figure 6.9. Such tilting is an indication of the existing settlement problems and the weakness of the soil conditions. There areas are likely to experience liquefaction in case of a large earthquake.



Figure 6.9: Examples of tilted houses in Karşıyaka due to soft fundament of the houses. The pictures were taken during the field trip in autumn 2006.

6.2.2 Other secondary effects

Fault rupture hazard in the case of the city of İzmir is only associated with the İzmir fault, since it lies underneath the metropolitan area. It was reported from the earthquake in 1688 that the city center of İzmir was lowered by 60 cm due to an earthquake on the İzmir fault. During the fieldtrip to İzmir in autumn 2006 the sea level in the innermost part of the İzmir bay was estimated to be approximately one meter below the street level of the city center. Therefore a lowering of the city will in certain areas result in flooding of the land.

Furthermore, slope instabilities occur in densely populated areas in the central part of İzmir, where construction practices are poor. Similarly the mountains surrounding the city are also prone to slope instabilities. In addition occurrence of sub-marine landslides are not studied in detail. However, such sub-marine slides triggered by large earthquakes are quite well determined elsewhere in the world.

Finally effects of tsunamis have already been reported for i.e. the 1688 earthquake (Altinok and Ersoy, 2000; Ambraseys and Finkel, 1995; Papazachos and Papazachou, 1997; Papazachos et al., 1997). It is however not only tsunamis associated with local earthquakes which pose additional hazard in the coastal area of the İzmir Bay, also other regional large earthquakes occurring in the Aegean Sea can be considered a threat.

6.3 Weaknesses in the methodology

The methodology adopted in this study contains various weaknesses. As it was mentioned in section 2.3.2 there are methods to conduct ground motion modeling based on a 3D velocity structure. In this study a 1D velocity model has been used because of limitations in availability of data as well as in computer power. In the following limitations of the methodology is described. This discussion is divided into two sections; one concerning the uncertainties in the input used to conduct the ground motion simulations and the other describing limitations in the program package, which have become evident during this study.

6.3.1 Uncertainties in the input

When conducting ground motion simulations two types of uncertainties need to be taken into account, epistemic and aleatory uncertainties (Frankel et al., 2002). The epistemic uncertainties concern the uncertainty connected to the model, in this case the understanding of the fault model. The input parameters in this category are fault geometry, segmentation, asperity location and total seismic moment. These parameters can by means of additive data and extensive field work be better defined and thereby yield more correct values, which then can be used in new earthquake scenarios.

The aleatory uncertainties involve randomness and is therefore, in ground motion simulations, related to parameters of fault rupture dynamics, i.e. parameters which are random in character and therefore difficult to obtain precisely. Parameters influenced by randomness are thus the rupture initiation point, rise time, rupture velocity and stress drop. Furthermore input to the ground motion simulations as the velocity and attenuation model can be classified as both having both epistemic and aleatory characters. It is possible to determine these parameters to some extent in a region, yielding epistemic character, however, inhomogeneities in the crust will cause randomness in the model and thereby introduce aleatory uncertainties.

In order to estimate the effect of the parameters influenced by randomness a sensitivity study can be conducted, where the parameters are changed one at a time and the ground motion distribution obtained are then compared to the ground motion distribution obtained from a reference scenario.

The scope of this study was to produce several earthquake scenarios on faults located near İzmir in order to determine which faults are the most critical concerning the seismic hazard in the study area. For this reason the parameter sensitivity is not studied in detail and will be discussed based on a previous study by Sørensen et al. (in press). Sørensen et al. (in press) show that the simulated ground motion is dependent on critical parameters such as rise time, rupture velocity, rupture initiation point and stress drop, which can change the output for an earthquake scenario significantly. There are usually large uncertainties when choosing the values for the input

parameters used in the ground motion simulations, and this should be done very carefully.

The scenario earthquake 1C IF was conducted with the hypocenter placed at two different locations; one in the most eastern end of the eastern segment, which is the scenario earthquake presented in the results, section 5.1.3, and one where the hypocenter was placed in the westernmost end of the western segment, corresponding to the location of the hypocenter of scenario 1A WIF. The ground motion distributions for the scenario with the hypocenter placed in the western segment are given in figure 6.10.

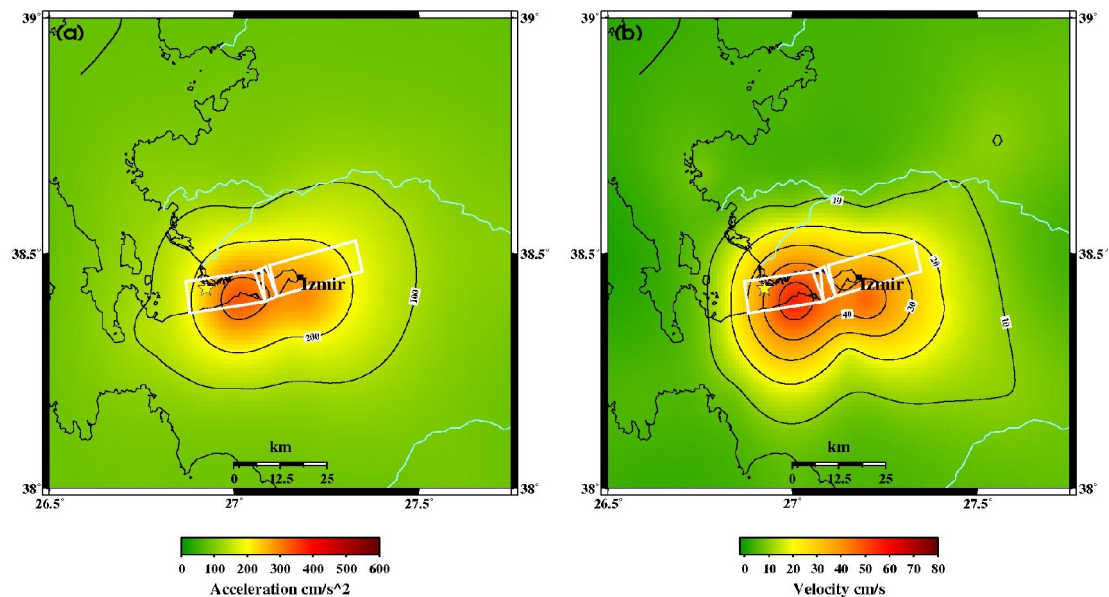


Figure 6.10: Peak ground motion distributions for the scenario earthquake on the İzmir Fault similar to scenario 1C IF, though with the hypocenter placed in the western segment. **a)** Peak ground acceleration cm/s^2 , **b)** peak ground velocity cm/s .

Same input parameters are adopted in each of the two simulations for comparison; only the rupture initiation point is changed. In both cases, the largest ground motions are observed above the segment where the hypocenter is located. For this reason the scenario where the hypocenter is placed in the eastern segment will produce the largest ground motions in İzmir, since this segment is located under the city center. This earthquake scenario is therefore found to be of the largest concern when considering the seismic hazard. Based on this study ground motion simulations should be conducted for scenario 1C IF with the hypocenter located in the same place as for scenario 1B EIF (the most western part of the eastern segment) in order to investigate

the ground motion distribution in İzmir, when the rupture propagates bilaterally along the fault segments.

6.3.2 Computational deficiencies/limitations of the code

The presented study has revealed computational deficiencies and limitations in the adopted code. These concern difficulties in differentiating hanging wall and footwall block ground motions as well as modeling step-overs and will be described in this section.

Ground motion simulations are conducted for both strike-slip faulting and normal faulting earthquakes in this study. The contour maps showing the peak ground motions for the different scenarios all show symmetry in the distribution of the peak ground motions around the fault. However, previous studies have shown that for normal faulting earthquakes there is a broken symmetry of the ground motions, yielding higher ground motions in the hanging wall block than on the footwall block (Brune and Anooshehpour, 1999; Oglesby et al., 1998; Shi et al., 2003).

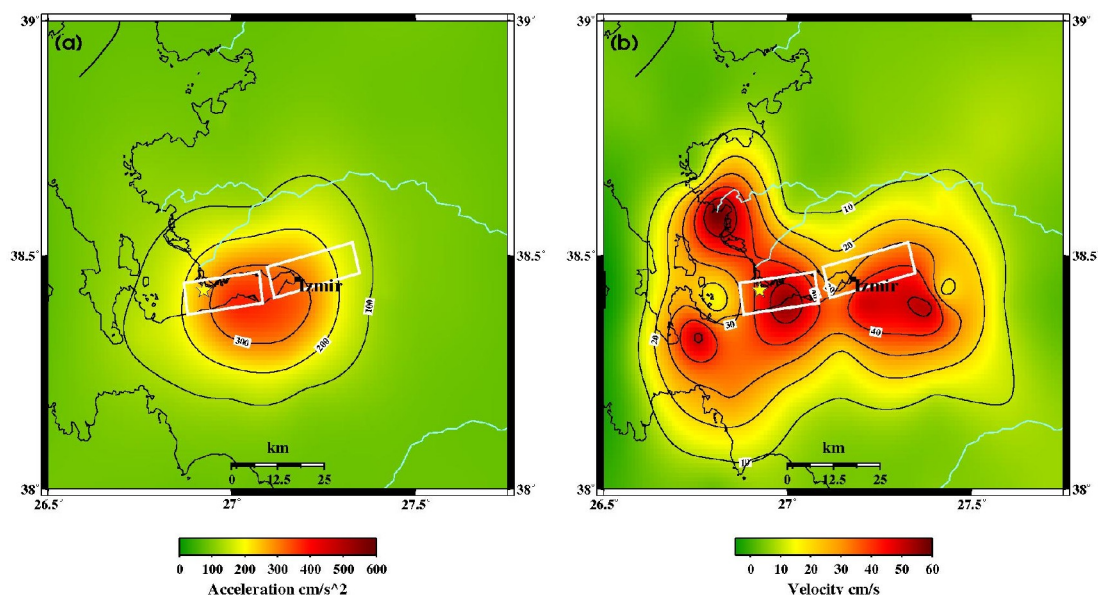


Figure 6.11: Peak ground motions from an earthquake scenario on the two segments of the İzmir fault with a 3 kilometer step-over in the middle.

The higher ground motion in the hanging block is not taken into account in the ground motion simulation. Thus higher peak ground motions are expected to occur in these regions, than the simulation results shows. In the case of the earthquake scenarios on

the İzmir fault this will cause larger ground motion in the city center, since this is placed on the hanging wall block.

During the work with the ground motion simulations it has come clear that the applied method has a limitation in the algorithm used for step-overs. This problem was first realized when calculating an earthquake scenario consisting of two separate segments of the İzmir fault with a 3 km step-over in the middle. The resulting maps showing the peak ground motion distribution are shown in figure 6.11. Compared to figure 5.5 in section 5.1 these results produce an artificial and unusual pattern for the peak ground velocity.

7 Conclusion

In this thesis the ground motion caused by nine earthquake scenarios on faults in the vicinity of İzmir are presented. The conclusions can be grouped into two categories on both the simulation results as well as the methodology used.

The following conclusions can be made from the simulation results:

- The worst-case scenario for seismic hazard in the center of İzmir is scenario 1C IF. Peak ground accelerations of 291 cm/s^2 and peak ground velocities of 48 cm/s are estimated.
- The frequency content of the simulated response spectra is in the same frequency range found for the fundamental frequency for sites in İzmir in a previous H/V study, suggesting significant potential site effects due to amplification.
- The simulation results indicate significantly higher ground motion values for two scenarios; İzmir and Tuzla faults. The historic events, which have caused destruction of İzmir, are therefore most likely to have occurred on these fault segments.
- The attenuation relation used in the ground motions simulations agrees well with empirical relations in case of the peak ground accelerations for the scenarios conducted for strike-slip faulting earthquakes, whereas the simulated values obtained for the normal faulting earthquakes are found to be lower than predicted.
- The peak ground velocities obtained from the simulations have a large spread in the attenuation properties, compared to the acceleration.
- The largest directivity effects are observed from the earthquake scenarios conducted on the Gülbahçe and Tuzla faults.
- The earthquake scenarios conducted on the three segments of the Manisa fault (scenario 5A-C MF) are considered to be of marginal concern with regard to the hazard in İzmir.

In addition the following more general conclusions can be drawn on the methodology used:

- The technique predicts higher peak ground accelerations for strike-slip faulting than normal faulting earthquakes, which is consistent with previous studies.
- There is not found higher ground motion values in the hanging block than in the footwall block in the normal faulting scenarios, although this is predicted by previous studies.
- The distribution of significant ground motion is highly dependent on the location of the rupture initiation point of the earthquake rupture scenario.
- The simulation technique has limitations in calculating the ground motion simulations based on earthquake scenarios on disconnected fault segments (i.e. step-overs cannot be modelled).

8 Future perspectives

Results obtained in this thesis have revealed several concerns where focused efforts are needed in future studies. These are divided into two main groups: one concerning the future earthquake hazard estimates in the area around İzmir, and the other concerning the improvement of the methodology used in this thesis in order to obtain realistic ground motion simulations.

8.1 Future work in the area around İzmir

A realistic seismic hazard assessment is highly dependent upon the understanding of the fault behaviour and consequently a future earthquake hazard assessment will require a detailed fieldwork in the area. The fieldwork should aim at a better understanding of the fault characteristics and possibly also of the fault interactions in order to investigate stress transfer during an earthquake taking the dense location of faults into account.

A better understanding of the link between short and long term deformation and how these affect the seismic hazard is necessary. On a regional lithospheric scale a study of the deformational processes that leads to the development of intra-continental micro-plate boundaries and relate these to plate driving and resisting forces is needed. This will provide a sound basis for setting up kinematic models for the region.

A realistic input for a kinematic model should include the analyses of;

- historic and instrumental seismicity,
- focal mechanism inversion for regional stress,
- stress transfer analysis for fault interactions,
- interpretation of already existing GPS velocity data and paleomagnetism to understand possible block rotations and
- paleoseismicity to assess the fault segmentation model and their behaviour

Also analysis of fault segmentation and behaviour is an integrated part of this model build-up. A better developed kinematic model is a prerequisite in order to produce new and more exact ground motion simulations in the area.

In continuation of the study conducted in this thesis a sensitivity study is needed to evaluate the effects of variations in the input parameters. Such a study should include the scenario 1C IF and 3 TF in order to further investigate the sensitivity of input parameters in comparison between normal faulting and strike-slip faulting earthquake scenarios. Additionally, an evaluation of the different possible hypocenter locations of especially the İzmir fault is also needed, as described in section 6.3.1.

Finally, new earthquake scenarios on the various fault segments of the İzmir and Tuzla faults should be conducted. Rupture scenarios of historical events need to be carried out in order to better constraint the correlation to historical earthquake occurrences. Such a study will help estimating the reactivation potential and recurrence time in order to conduct a probabilistic estimate of the seismic hazard in the area, based on deterministic ground motion simulations (see section 8.2.).

8.2 Improvement of the methodology

The methodology used in this thesis has several limitation which became evident during the study. The simulated ground motions on normal faults (scenario 1A-C IF and 5A-C MF) all show homogeneous distribution for both the hanging wall and the footwall blocks. However, previous studies have proven that much larger ground motions are obtained in the hanging block than on the footwall block, as it was also discussed in chapter 6.3.2. This should be taken into account in future studies.

As mentioned in section 6.3.2 it is, with the available program package, not possible to conduct ground motion simulations based on earthquake scenarios which consist of several disconnected segments. This should be corrected for future studies.

The ground motions are furthermore calculated for bedrock conditions and thereby the unconsolidated sedimentary layers, which are present in the study area due to large

river deltas and artificially filled coastal areas, are not included in the calculations. Simulating the effects of sedimentary deposits is feasible (e.g. Sørensen et al. (2006)). However, calculating the ground motions for the whole study area used in this thesis would be too demanding with regard to computer power as well as constraining the geotechnical properties of the sediments as it is today. Future studies focusing on geotechnical characteristics of the sediments should therefore be conducted.

The method presented in this work provides a better assessment of the hazard when compared to previous probabilistic seismic hazard assessments. Ground motions are calculated for different earthquake scenarios, and hence the method is purely deterministic. In areas like the İzmir case, where several active faults control the earthquake hazard, this should be treated probabilistically. The standard probabilistic methodology (PSHA) ignores fault interaction, stress transfer and fault rupture complexity due to fault rupture dynamics and wave propagation. It is therefore necessary to develop a new technique where hybrid ground motion simulations from individual rupture scenarios are treated probabilistically.

There are ongoing efforts in the region to address the issues mentioned above.

9 Acknowledgements

First I want to express my gratitude to my supervisors Kuvvet Atakan and Jens Havskov for supervision, fruitful discussions and for providing an excellent environment for all their students. I also wish to thank Mathilde Bøttger Sørensen for helpful support with understanding the universe of ground motion simulations and for answering definitely many and confusing questions in and out of season. I am grateful to Mohammad Raaesi for all the hours we have spent in front of the computers working with the Global Mapping Tools (GMT) in order to produce the maps shown in this thesis. I thank Harald Walderhaug and Coskun Sari for providing paleomagnetic and H/V results respectively. I also thank Anette Hald-Bjerrum for the tremendous work she has put in proof-reading of the thesis at hand.

I wish to thank my friends in Denmark, who have supported me in my decision to stay in Norway, for having kept contact and always taken their time to see me in my sometimes rather hectic plans during my stays in Denmark. Especially I would like to mention Anne Katrine Alsing, Ditte Maria Grønhøj, Morten Ib Nielsen and Kathrine Dam Andersen. During the two and a half years in Norway I have met many great people, who have made the stay much more delightful. First of all I want to mention the people I met in Fantoft, especially Maria Foged, Mo Yan Yuen, and Mariann Richterhausen Pedersen. I want to thank the people in the geodynamics group; among them the members of the Cake-Club who have helped and supported me in the writing of my thesis, in particular Zoya Zarifi, Mohammad Raaesi, Hlompho Malephane, Anna Ksienzyk and Aleksandre Kandilarov. Last but not least I want to thank the group of Norwegian geology students for many laughs, lunches and coffee breaks, especially Nina Petersen, Turid Knudsen and Kjersti Solveit.

Finally I want to thank my family. My parents - mom, step-mom, dad and step-dad: Alice Wedderkopp, Anette Hald-Bjerrum, Jakob Hald-Bjerrum and Ole Frandsen - who have been a tremendous support in my considerations and decision of extending my stay in Bergen; always making sure I had a place to come home to, as well as morally during the last hectic months while finishing my studies.

10 References

Aki, K., and Richards, P.G., 2002, Quantitative Seismology: *Sausalito, California*, University Science Books, 700 p.

Akinci, A., Ibanez, J.M., del Pezzo, E., and Morales, J., 1995, Geometrical spreading and attenuation of Lg waves: a comparison between western Anatolia (Turkey) and southern Spain: *Tectonophysics*, v. **250**, p. 47-60.

Akinci, A., Mejia, J., and Jemberie, A.L., 2004, Attenuative Dispersion of P Waves and Crustal Q in Turkey and Germany: *Pure and Applied Geophysics*, v. **161**, p. 73-91.

Akinci, A., Taktak, A.G., and Ergintav, S., 1994, Attenuation of coda waves in Western Anatolia: *Physics of the Earth and Planetary Interiors*, v. **87**, p. 155-165.

Akkar, S., and Bommer, J.J., 2007, Empirical Prediction Equations for Peak Ground Velocity Derived from Strong-Motion Records from Europe and the Middle East: *Bulletin of the Seismological Society of America*, v. **97**, p. 511-530.

Aktug, B., and Kilicoglu, A., 2006, Recent crustal deformation of Izmir, Western Anatolia and surrounding regions as deduced from repeated GPS measurements and strain field: *Journal of Geodynamics*, v. **41**, p. 471-484.

Altinok, Y., Alpar, B., Özer, N., and Gazioglu, C., 2005, 1881 and 1949 earthquakes at the Chios-Cesme Strait (Aegean Sea) and their relation to tsunamis: *Natural Hazards and Earth System Sciences*, v. **5**, p. 717-725.

Altinok, Y., and Ersoy, S., 2000, Tsunamis Observed on and Near the Turkish Coast: *Natural Hazards*, v. **21**, p. 185-205.

Altunel, E., 1998, Evidence for Damaging Historical Earthquakes at Priene, Western Turkey: *Tr. J. of Earth Sciences*, v. **7**, p. 25-35.

Ambraseys, N.N., and Finkel, C.F., 1995, The Seismicity of Turkey and Adjacent Areas, A Historical Review, 1500-1800: Istanbul, Muhittin Salih EREN.

Ambraseys, N.N., and Jackson, J.A., 1998, Faulting associated with historical and recent earthquakes in the Eastern Mediterranean region.: *Geophysical Journal International*, v. **133**, p. 390-406.

Anderson, J.G., Wesnousky, S.G., and Stirling, M.W., 1996, Earthquake size as a function of fault slip rate: *Bulletin of the Seismological Society of America*, v. **86**, p. 683-690.

Armijo, R., Meyer, B., King, G., A., R., and Papanastassiou, D., 1996, Quaternary evolution of the Corinth rift and its implications for Late Cenozoic evolution of the Aegean: *Geophysical Journal International*, v. **126**, p. 11-53.

Atakan, A., 2005, Mikrotremor ölçümleri ve mühendislik uygulamaları *Chamber of Geophysical Engineers: Izmir, Turkey.*

Atakan, K., Bard, P.-Y., Kind, F., Morene, B., Roquette, P., Tendo, A., and SESAME-Team, 2004a, J-SESAME: A standardized software solution for the H/V spectral ratio technique, *13th World Conference on Earthquake Engineering: Vancouver, B.C., Canada.*

Atakan, K., Duval, A.-M., Theodulidis, N., Guillier, B., J.-L., C., Bard, P.-Y., and SESAME-Team, 2004b, The H/V spectral ratio technique: experimental conditions, data processing and empirical reliability assessment, *13th World Conference on Earthquake Engineering: Vancouver, B.C., Canada.*

Aydinoglu, M.N., 1998, Specification for structures to be built in disaster areas, *Ministry of Public Works and Settlement Government of Republic of Turkey.*

Ayhan, M.E., Demir, C., Lenk, O., Kilicoglu, A., Altiner, Y., Barka, A.A., Ergintav, S., and Ozener, H., 2002, Interseismic Strain Accumulation in the Marmara Sea Region: *Bulletin of the Seismological Society of America*, v. **92**, p. 216-229.

Bayrak, Y., and Yilmazturk, A., 1999, Stress Drop and Classification of Global Earthquakes, *Second Balkan Geophysical Congress and Exhibition.*

Becker, A.M., and Abrahamson, N.A., 1998, Stress drops in extensional regimes: *Seismological Research Letters*, v. **69**, p. 172.

Benetatos, C., Kiratzi, A., Ganas, A., Ziazia, M., Plessa, A., and Drakatos, G., 2006, Strike-slip motions in the Gulf of Sigacik (western Turkey): Properties of the 17 October 2005 earthquake seismic sequence: *Tectonophysics*, v. **426**, p. 263-279.

Bindi, D., Parolai, S., Grosser, H., Milkereit, C., and Karakisa, S., 2006a, Crustal Attenuation Characteristics in Northwestern Turkey in the Range from 1 to 10 Hz: *Bulletin of the Seismological Society of America*, v. **96**, p. 200-214.

Bindi, D., Parolai, S., Grosser, H., Milkereit, C., and Zunbul, S., 2006b, Cumulative Attenuation along Source-to-Receiver Paths in Northwestern Turkey: *Bulletin of the Seismological Society of America*, v. **96**, p. 188-199.

Boore, D.M., 1983, Stochastic simulation of high-frequency ground motions based on seismological models of the radiated spectra: *Bulletin of the Seismological Society of America*, v. **73**, p. 1865-1894.

Boore, D.M., and Joyner, W.B., 1997, Site amplifications for generic rock sites: *Bulletin of the Seismological Society of America*, v. **87**, p. 327-341.

Bouchon, M., 1981, A simple method to calculate Green's functions for elastic layered media: *Bulletin of the Seismological Society of America*, v. **71**, p. 959-971.

Bozkurt, E., and Sözbilir, H., submitted, Evolution of the Large-scale Active Manisa Fault, Southwest Turkey: Implications on Fault Development and Regional Tectonics: *article in review, Submitted.*

Brune, J.N., 1970, Tectonic stress and the spectra of seismic shear waves from earthquakes: *Journal of Geophysical Research*, v. **75**, p. 4997-5009.

Brune, J.N., and Anooshehpour, A., 1999, Dynamic geometrical effects on strong ground motion in a normal fault model: *Journal of Geophysical Research*, v. **104**, p. 809-815.

Campbell, K.W., 1997, Empirical Near-Source Attenuation Relationships for Horizontal and Vertical Components of Peak Ground Acceleration, Peak Ground Velocity, and Pseudo-Absolute Acceleration Response Spectra: *Seismological Research Letters*, v. **68**, p. 154-179.

Clarke, P.J., Davies, R.R., England, P.C., Parsons, B., Billiris, H., Paradissis, D., Veis, G., Cross, P.A., Denys, P.H., Ashkenazi, V., Bingley, R., Kahle, H.-G., Muller, M.-V., and Briole, P., 1998, Crustal strain in central Greece from repeated GPS measurements in the interval 1989–1997: *Geophysical Journal International*, v. **135**, p. 195-214.

Cocard, M., Kahle, H.-G., Peter, Y., Geiger, A., Veis, G., Felekis, S., Paradissis, D., and Billiris, H., 1999, New constraints on the rapid crustal motion of the Aegean region: recent results inferred from GPS measurements (1993-1998) across the West Hellenic Arc, Greece: *Earth and Planetary Science Letters*, v. **172**, p. 39-47.

Cong, L., and Mitchell, B.J., 1998, Lg Coda Q and its Relation to the Geology and Tectonics of the Middle East *Pure and Applied Geophysics*, v. **153**, p. 563-585.

Dalguer, L.A., Miyake, H., and Irikura, K., 2004, Characterization of Dynamic Asperity Source Models for Simulating Strong Ground Motion, *13th World Conference on Earthquake Engineering: Vancouver, B.C., Canada.*

Das, S., and Kostrov, B.V., 1986, Fracture of a single asperity on a finite fault: a model for weak earthquakes?, in Das, S., Boatwright, J., and Scholz, C., eds., *Earthquake Source Mechanism: Washington*, American Geophysical Union, p. 91-96.

Durukal, E., Gunduz, A.S., Sanli, B., Sørensen, M.B., Richwalski, S., Sesetyan, K., Atakan, A., Madariaga, R., and Wang, R., 2006, A 'benchmarking' exercise on the performance of kinematic ground motion simulation codes, *EGU: Vienna.*

Emre, Ö., Dogan, A., Özalp, S., and Yildirim, C., 2005a, 17 Ekim 2005 Sigacik (Izmir) Depremleri Ön Degerlendirme Raporu: **Ankara**, Maden Tetkik ve Arama Genel Müdürlüğü, p. 6.

Emre, Ö., Özalp, S., Dogan, A., Özaksoy, V., Yildirim, C., and Göktas, F., 2005b, Izmir Yakin Cevresinin Diri Faylari Ve Deprem Potansiyelleri, *Maden Tetkik ve Arama, MTA*, p. 80.

EMSC, 2007, European-Mediterranean Seismological Centre, <http://www.emsc-csem.org>.

Erdik, M., Ansal, A., Aydinoglu, N., Barka, A., Isikara, A.M., Yüzügüllü, Ö., Avcı, J., Özel, O., Biro, Y.A., and Birgören, G., 2000, Izmir Deprem Senaryosu ve Deprem Master Planı.

Erdik, M., Biro, Y.A., Onur, T., Sesetyan, K., and Birgören, G., 1999, Assessment of earthquake hazard in Turkey and neighboring regions: *Annali de Geofisica*, v. **42**, p. 1125-1138.

Fairhead, J.D., and Wilson, M., 2005, Plate tectonic processes in the South Atlantic Ocean: Do we need deep mantle plumes: *Special Paper 388: Plates, plumes and paradigms*, v. **388**, p. 537-553.

Field, E.H., 2007, Overview of the Working Group for the Development of Regional Earthquake Likelihood Models (RELM): *Seismological Research Letters*, v. **78**, p. 7-16.

Frankel, A.D., Petersen, M.D., Mueller, C.S., Haller, K.M., Wheeler, R.L., Leyendecker, E.V., Wesson, R.L., Harmsen, S.C., Cramer, C.H., Perkins, D.M., and Rukstales, K.S., 2002, Documentation for the 2002 Update of the National Seismic Hazard Maps.

Giardini, D., Gupta, H., Giesecke, A., Dimaté, C., Shedlock, K., Grunthal, G., Garcia, M., Iben Brahim, B., Slejko, D., Musson, R., Balassanian, S., Ulomov, V., Ashtiany, M.G., Atakan, A., Nyambok, I., Zhang, P., McCue, K., Engdahl, E., McGuire, R., and Mayer-Rose, D., 1999, Global Seismic Hazard Assessment Program, <http://www.seismo.ethz.ch/GSHAP/>, *Schweizerischer Erdbebendienst (SED)*.

Giardini, D., Jiménez, M.-J., and Grunthal, G., 2003, The ESC-SESAME Unified Seismic Hazard Model for the European-Mediterranean Region, <http://wija.ija.csic.es/gt/earthquakes/>, in Giardini, D., Jiménez, M.-J., and Grunthal, G., eds.

Goldsworthy, M., Jackson, J., and Haines, J., 2002, The continuity of active faults in Greece: *Geophysical Journal International*, v. **148**.

Gülkan, P., and Kalkan, E., 2002, Attenuation modeling of recent earthquakes in Turkey: *Journal of Seismology*, v. **6**, p. 397-409.

Hanks, T.C., and Kanamori, H., 1979, A moment magnitude scale: *Journal of Geophysical Research*, v. **84**, p. 2348-2350.

Hartzell, S.H., 1978, Earthquake aftershocks as Green's functions: *Geophysical Research Letters*, v. **5**, p. 1-4.

Havskov, J., and Ottemöller, L., 2003, SEISAN: The Earthquake Analysis Software: **Bergen**, 244 p.

Heaton, T., Tajima, F., and Mori, A.W., 1986, Estimating ground motions using recorded accelerograms: *Surveys in Geophysics*, v. **8**, p. 25-83.

Hernandez, B., N.M.; S., S.K.; S., Pacheco, J.F., Cotton, F., Campillo, M., Iglesias, A., Crus, V., Gómez, J.M., and Alacántara, L., 2001, Rupture History of September 30, 1999 Intraplate Earthquake of Oaxaca, Mexico (Mw=7.5) from Inversion of Strong-Motion Data: *Geophysical Research Letters*, v. **28**, p. 363-366.

Horasan, G., Gulen, L., Pinar, A., Kalafat, D., Ozel, N., Kuleli, H.S., and Isikara, A.M., 2002, Lithospheric Structure of the Marmara and Aegean Regions, Western Turkey: *Bulletin of the Seismological Society of America*, v. **92**, p. 322-329.

Hutchings, L., Stavrakakis, G.N., Ioannidou, E., Wu, F.T., Jarpe, S., and Kasameyer, P., 1998, Strong Ground Motion Synthesis for a M=7.2 Earthquake in the Gulf of Coringth, Greece Using Emperical Green's Functions, *29th IASPEI General Assembly: Thessaloniki, Greece*, Lawrence Livermore National Laboratory.

Irikura, K., 1986, Prediction of strong acceleration motion using empirical Green's functions, *Proc. 7th Japan Earthquake Symp.: Japan*, p. 151-156.

Isseven, T., 2001, Batı Anadolu'nun neotektonik rejiminin paleomanyetik çalışmalarla incelenmesi [Doctoral thesis].

Jackson, J.A., King, G., and Vita-Finzi, C., 1982, The neotectonics of the Aegean: an alternative view: *Earth and Planetary Science Letters*, v. **61**, p. 303-318.

Jimenez, M.-J., Giardini, D., and Grunthal, G., 2003, The ESC-SESAME Unified Hazard Model for the European-Mediterranean region: *EMSC/CSEM Newsletter*, v. **19**, p. 2-4.

Kamae, K., Irikura, K., and Pitarka, A., 1998, A technique for simulating strong ground motion using hybrid Green's function: *Bulletin of the Seismological Society of America*, v. **88**, p. 357-367.

Kanamori, H., 1977, The energy release in great earthquakes: *Journal of Geophysical Research*, v. **82**, p. 2981-2988.

Kanamori, H., and Anderson, D.L., 1975, Theoretical basis of some empirical relations in seismology: *Bulletin of the Seismological Society of America*, v. **65**, p. 1073-1095.

Kim, W.-Y., Kulhanek, O.T.A., and Meyer, K., 1984, Source processes of the 1981 Gulf of Corinth earthquake sequence from body-wave analysis: *Bulletin of the Seismological Society of America*, v. **74**, p. 459-477.

Kiratzi, A., and Louvari, E., 2003, Focal mechanisms of shallow earthquakes in the Aegean Sea and the surrounding lands determined by waveform modelling: a new database: *Journal of Geodynamics*, v. **36**, p. 251-274.

Kissel, C., 1986, Apport du paleomagnetisme a la comprehension de l'évolution geodynamique Tertiaire du domaine Egeen de L'épire a L'anatolie occidentale [Ph.D. thesis]: Paris, A L'Universite de Paris-Sud Centre D'Orsay.

Kissel, C., Laj, C., Sengör, A.M.C., and Poisson, A, 1987, Paleomagnetic evidence for rotation in opposite senses of adjacent blocks in Northeastern Aegea and Western Anatolia: *Geophysical Research Letters*, v. **14**, p. 907-910.

Koller, M.G., Chatelain, J.-L., Guillier, B., Duval, A.-M., Atakan, K., Lacave, C., Bard, P.-Y., and participants, S., 2004, Practical used guidelines and software for the implementation of the H/V ratio technique: measuring conditions, processing method and results interpretation, *13th World Conference on Earthquake Engineering: Vancouver, B.C, Canada*.

Kotzev, V., Nakov, R., Burchfiel, B.C., King, R., and Reilinger, R., 2001, GPS study of the active tectonics in Bulgaria: Results from 1996 to 1998: *Journal of Geodynamics*, v. **31**, p. 189-200.

Larson, E., 2006, Global CMT Catalog search, *G. Ekström and N. Nettles*.

Lay, T., and Wallace, T., 1995, Modern Global Seismology, **Academic Press, Inc**, 521 p.

Le Pichon, X., Chamot-Rooke, N., Lallemand, S., Noomen, R., and Veis, G., 1995, Geodetic determination of the kinematics of central Greece with respect to Europe: *Journal of Geophysical Research*, v. **100**, p. 12,675-12,690.

Mai, M., 2007, SRCMOD: a database of finite-source rupture models, <http://www.seismo.ethz.ch/srcmod/> *Schweizerischer Erdbebendienst (SED) Swiss Seismological Service*.

Mai, M., Spudich, P., and Boatwright, J., 2005, Hypocenter Locations in Finite-Source Rupture Models: *Bulletin of the Seismological Society of America*, v. **95**, p. 965-980.

McClusky, S., Balassanian, S., Barka, A., Demir, C., Ergintav, S., Georgiev, I., Gurkan, O., Hamburger, M., Hurst, K., Kahle, H., Kastens, K., Kekelidze, G., King, R., Kotzev, V., Lenk, O., Mahmoud, S., Mishin, A., Nadariya, M., Ouzounis, A., Paradissis, D., Peter, Y., Prilepin, M., Reilinger, R., Sanli, I., Seeger, H., Tealeb, A., Toksöz, M.N., and Veis, G., 2000, Global Positioning System constraints on plate kinematics and dynamics in the eastern Mediterranean and Caucasus: *Journal of Geophysical Research*, v. **105**, p. 5695-5719.

McGarr, A., 1984, Scaling ground motion parameters, state of stress, and focal depth: *Journal of Geophysical Research*, v. **89**, p. 6,969-6979.

McKenzie, D., 1972, Active tectonics of the Mediterranean region: *Geophysical Journal R. astronomical Society*, v. **30**, p. 109-185.

- McKenzie, D., 1978, Active tectonics of the Alpine Himalayan Belt, the Aegean Sea and surrounding regions: *Geophysical Journal R. astronomical Society*, v. **55**, p. 217-252.
- McKenzie, D., and Jackson, J.A., 1983, The relationship between strain rates, crustal thickening, paleomagnetism, finite strain and fault movements within a deforming zone: *Earth and Planetary Science Letters*, v. **65**, p. 182-202.
- Meade, B.J., Hager, B.H., McClusky, S.C., Reilinger, R.E., Ergintav, S., Lenk, O., Barka, A., and Ozener, H., 2002, Estimates of Seismic Potential in the Marmara Sea Region from Block Models of Secular Deformation Constrained by Global Positioning System Measurements: *Bulletin of the Seismological Society of America*, v. **92**, p. 208-215.
- Mendoza, C., and Hartzell, S.H., 1988, Inversion for slip distribution using teleseismic P waveforms: North Palm Springs, Borah Peak, and Michoacan earthquakes: *Bulletin of the Seismological Society of America*, v. **78**, p. 1092-1111.
- Nakamura, Y., 1989, A method for dynamic characteristics estimation of subsurface using microtremor on the ground surface: *Quarterly Report of RTRI*, v. **30**, p. 25-33.
- Nyst, M., and Thatcher, W., 2004, New constraints on the active tectonic deformation of the Aegean: *Journal of Geophysical Research*, v. **109**, p. 406-430.
- Oglesby, D.D., Archuleta, R.J., and Nielsen, S.B., 1998, Earthquakes on Dipping Faults: The Effects of Broken Symmetry: *Science*, v. **280**, p. 1055-1059.
- Orbay, N., Sanver, M., Hisarli, M., İseven, T., and Özcep, F., 2000, Karaburun Yarımadasının paleomagnetizması ve tektonik evrimi: *Bati Anadolu' nun Depremselliği Sempozyumu kitabı*, p. 59-67.
- Pankow, K.L., and Pechmann, J.C., 2004, The SEA99 Ground-Motion Predictive Relations for Extensional Tectonic Regimes: Revisions and a New Peak Ground Velocity Relation: *Bulletin of the Seismological Society of America*, v. **94**, p. 341-348.
- Papazachos, B., and Papazachou, C., 1997, The Earthquakes of Greece: **Thessaloniki**, *Technical books Edition*.
- Papazachos, B.C., Kiratzi, A., and Papadimitriou, E.E., 1991, Regional Focal Mechanisms for Earthquakes in the Aegean Area: *Pageoph*, v. **136**, p. 405-418.
- Papazachos, B.C., Papaioannou, C.A., papazachos, C.B., and Savvaidis, A.S., 1997, Atlas of Iseismal Maps for Strong Shallow Earthquakes in Greece and Surrounding Area (426BC-1995): **Thessaloniki**, *Technical books Editions*.
- Pitarka, A., Somerville, P., Fukushima, Y., Uetake, T., and Irikura, K., 2000, Simulation of Near-Fault Strong-Ground Motion Using Hybrid Green's Functions: *Bulletin of the Seismological Society of America*, v. **90**, p. 566-586.

Pondrelli, S., Morelli, A., and Ekström, G., 2004, European-Mediterranean Regional Centroid Moment Tensor catalog: solutions for years 2001 and 2002: *Phys. Earth Planet. Int.*, v. **145**, p. 127-147.

Pondrelli, S., Morelli, A., Ekström, G., Mazza, S., Boschi, E., and Dziewonski, A.M., 2002, European-Mediterranean regional centroid-moment tensors: 1997-2000: *Phys. Earth Planet. Int.*, v. **130**, p. 71-101.

Pondrelli, S., Salimbeni, S., Ekström, G., Morelli, A., Gasperini, P., and G., V., 2006, The Italian CMT dataset from 1977 to the present: *Phys. Earth Planet. Int.*, v. **159**, p. 286-303.

Pulido, N., and Kubo, T., 2004, Near-fault strong motion complexity of the 2000 Tottori earthquake (Japan) from a broadband source asperity model: *Tectonophysics*, v. **390**, p. 177-192.

Pulido, N., Ojeda, A., Atakan, A., and Kubo, T., 2004, Strong ground motion estimation in the Sea of Marmara region (Turkey) based on a scenario earthquake: *Tectonophysics*, v. **391**, p. 357-374.

Reiter, L., 1990, Earthquake Hazard Analysis: Issues and Insights, **Columbia University Press**, 254 p.

Sargeant, S.L., Burton, P.W., Douglas, A., and Evans, J.R., 2002, The Source Mechanism of the Athens Earthquake, September 7, 1999, Estimated from P Seismograms Recorded at Long Range: *Natural Hazards and Earth System Sciences*, v. **27**, p. 35-45.

Saunders, P., Priestley, K., and Taymaz, T., 1998, Variations in the crustal structure beneath western Turkey: *Geophysical Journal International*, v. **134**, p. 373-389.

Shi, B., Brune, J.N., Zeng, Y., and Anooshehpour, A., 2003, Dynamics of Earthquake Normal Faulting: Two-Dimensional Lattice Particle Model: *Bulletin of the Seismological Society of America*, v. **93**, p. 1179-1197.

Somerville, P., Irikura, K., Graves, R., Sawada, S., Wald, D., Abrahamson, N., Iwasaki, Y., Kagawa, T., Smith, N., and Kowada, A., 1999, Characterizing Crustal Earthquake Slip Models for the Prediction of Strong Ground Motion: *Seismological Research Letters*, v. **70**, p. 59 - 80.

Somerville, P., Sen, M., and Cohee, B., 1991, Simulation of strong ground motions recorded during the 1985 Michoacan, Mexico and Valparaiso, Chile earthquakes: *Bulletin of the Seismological Society of America*, v. **81**, p. 1-27.

Spudich, P., Fletcher, J.B., Hellweg, M., Boatwright, J., Sullivan, C., Joyner, W.B., Hanks, T.C., Boore, D.M., McGarr, A., Baker, L.M., and Lindh, A.G., 1997, SEA96 - A New Predictive Relation for Earthquake Ground Motions in Extensional Tectonic Regimes: *Seismological Research Letters*, v. **68**, p. 190-198.

Stein, S., and Wysession, M., 2003, An Introduction to Seismology, Earthquakes, and Earth Structure, **Blackwell Publishing**.

Sørensen, M.B., Atakan, K., and Pulido, N., 2007, Simulated Strong Ground Motions for the Great M 9.3 Sumatra-Andaman Earthquake of 26 December 2004: *Bulletin of the Seismological Society of America*, v. **97**, p. S139-151.

Sørensen, M.B., Oprsal, I., Bonnefoy-Claudet, S., Atakan, K., Mai, P.M., Pulido, N., and Yalciner, C., 2006, Local site effects in Ataköy, Istanbul, Turkey, due to a future large earthquake in the Marmara Sea: *Geophysical Journal International*, v. **167**, p. 1413-1424.

Sørensen, M.B., Pulido, N., and Atakan, K., in press, Sensitivity of ground motion simulations to earthquake source parameters: a case study for Istanbul, Turkey: *Bulletin of the Seismological Society of America*.

Tapirdamaz, M.C., 2005, Türkiye'nin paleomanyetik veri katalogu, *ATAG9: Aktif Tektonik Arastirma Grubu 9*.

Taymaz, T., Jackson, J., and McKenzie, D., 1991, Active tectonics of the north and central Aegean Sea: *Geophysical Journal International*, v. **106**, p. 433-490.

Tselentis, G.A., and Zahradnik, J., 2000, The Athens Earthquake of 7 September 1999: *Bulletin of the Seismological Society of America*, v. 90, p. 1143-1160.

USGS, E.H.P., 2007, USGS, Earthquake Hazards Program, <http://earthquake.usgs.gov/>.

Wells, D.L., and Coppersmith, K.J., 1994, New empirical relationships among magnitude, rupture length, rupture width, rupture area, and surface displacement: *Bulletin of the Seismological Society of America*, v. **84**, p. 974-1002.

Westaway, R., 1990a, Block rotation in western Turkey 1. Observational evidence: *Journal of Geophysical Research*, v. **95**, p. 19857-19884.

Westaway, R., 1990b, Block rotation in western Turkey and elsewhere 2. Theoretical models: *Journal of Geophysical Research*, v. 95, p. 19885-19901.

Yagi, Y., 2004, Preliminary Results of Rupture Process for 2004 off coast of Northern Sumatra Giant Earthquake (ver. 1), <http://iisee.kenken.go.jp/staff/yagi/eq/Sumatra2004/Sumatra2004.html>.

Zhu, L., Akyol, N., Mitchell, B.J., and Sozbulir, H., 2006, Seismotectonics of western Turkey from high resolution earthquakes relocations and moment tensor determinations: *Geophysical Research Letters*, v. **33**.

Zor, E., Sandvol, E., Xie, J., Türkelli, N., Mitchell, B.J., Gasanov, A.H., and Yetirmishli, G., 2007, Crustal Attenuation within the Turkish Plateau and Surrounding Regions: *Bulletin of the Seismological Society of America*, v. **97**, p. 151-161.

This document was created with Win2PDF available at <http://www.win2pdf.com>.
The unregistered version of Win2PDF is for evaluation or non-commercial use only.